IMPLEMENTATION AND EVALUATION OF A TWO-DIMENSIONAL LASER DOPPLER VIBROMETER SYSTEM FOR NON-CONTACT MONITORING OF EXTERNAL STRESS LOADING OF ALUMINUM SAMPLES

A Thesis
Presented to
The Academic Faculty

by

Paul Wesley Langston

In Partial Fulfillment
of the Requirements for the Degree
Master of Science in Mechanical Engineering in the
Woodruff School of Mechanical Engineering

Georgia Institute of Technology
May 2009

IMPLEMENTATION AND EVALUATION OF A TWO-DIMENSIONAL LASER DOPPLER VIBROMETER SYSTEM FOR NON-CONTACT MONITORING OF EXTERNAL STRESS LOADING OF ALUMINUM SAMPLES

Approved by:

Dr. Karim G. Sabra, Advisor
Woodruff School of Mechanical Engineering
Georgia Institute of Technology

Dr. Laurence J. Jacobs
School of Civil and Environmental Engineering
(Joint Appointment in the Woodruff School)
Georgia Institute of Technology

Dr. François Guillot
Woodruff School of Mechanical Engineering
Georgia Institute of Technology

Date Approved:

ACKNOWLEDGEMENTS

TABLE OF CONTENTS

LIST OF TABLES

LIST OF FIGURES

ix

LIST OF ABBREVIATIONS

SHM Structural Health Monitoring

DFI Diffuse Field Interferometry

FT ; FFT Fourier Transform; Fast Fourier Transform

LDV Laser Doppler Vibrometer

SLDV Scanning Laser Doppler Vibrometer

SUMMARY

Multidimensional vibration measurements are used to enhance the reconstruction of wavefields providing great benefits to various areas including structural health monitoring (SHM) and non-destructive evaluation (NDE). This thesis describes the development of a 2D non-contact measurement system based on point LDV technology. It details the various hardware components and Labview software developed and integrated to gather both normal and in-plane vibration measurements as well as the testing used to determine the functionality and robustness of the capabilities of each component. The developed system was designed not only for optimal performance but also for flexibility, efficiency, and ease of use.

Upon completion of the hardware-software integration, the accuracy of the 2D LDV measurement configuration was studied through comparison to a PCB Triaxial (3D) Accelerometer. Measurements were simultaneously collected with both the LDV and accelerometer and compared to determine the accuracy of the 2D configuration with respect to the state of the art in industry. This comparison with the accelerometer validated the 2D LDV configuration and showed the high level of accuracy of the system.

Finally, the developed system was used to analyze the acoustoelastic effect in a small Aluminum plate under uniaxial compressive loading. Each component of motion was analyzed individually in an effort to determine how the relative frequency shift, ν, depends on the relative uniaxial compressive load. Linear relationships were seen between these two variables, and fits to the data were used to determine the compansion parameter in several resonance peaks of the complex waveform. The signals for the

normal and in-plane components of the waveform were then analyzed through multi-component joint analysis. This approach sought to determine metrics as well as qualitative measures which utilized both components simultaneously in order to determine how the relationship between the components of motion was affected by changing the applied load. Both polarization angle and time signal ellipse analyses were performed on the data with promising results for future low-frequency multi-dimensional vibration analysis applications.

CHAPTER 1

INTRODUCTION

1.1 Multidimensional Vibration Sensing

Structural Health Monitoring (SHM) and Non-Destructive Evaluation (NDE) systems often rely on propagating elastic waves through a part under inspection in order to assess its structural integrity and detect eventual degradations. With a 2D setup, both components of the vibration field can be measured [Giurgitu 2007; Rose 1999] These two components are defined as the directions normal and parallel to the plane of the surface of motion and shall be referred to as the normal and in-plane components of motion respectively.

Full wavefield methods use the detection of multiple components of surface motion (i.e. both normal and in-plane) to create of a more complete description of the elastic disturbances in an object. For instance, the ability to recreate a complete wavefield is especially useful to identify crack locations in SHM and NDE applications by detecting mode conversions in Lamb waves from symmetric (S_0) to anti-symmetric (A_0) and vice versa. Tomographic imaging can also be improved by measuring both components of a surface's motion. Another area that has shown some recent promising developments is the application of 2D measurement techniques to learn about the effects of stress on the vibration's polarization. Theoretical models have been developed that imply that polarization (a combination of normal and in-plane displacement) is more sensitive to changes in stress than more common approaches such as measuring the change in wave speed. [Junge et al. 2006] Multidimensional vibration measurement is an important

enabling technology in many areas, and its applications will only broaden as it improves and becomes more popular.

1.2 Existing 3D Technologies

Presently, multidimensional vibration measurement can be done in several different ways with sensors falling into two general categories based on the physical relationship required between the transducer and the object. The two groups of sensors are contact sensors and noncontact sensors, and they both have advantages and disadvantages.

1.2.1 Contact Sensors

As the name implies, contact sensors take measurements while in mechanical contact with the vibrating surface or object of interest. Strain gauges and many types of accelerometers fall into this category. In many industries, accelerometers are the state of the art, and they are very common almost anywhere motion measurements are taken due to their low cost and ease of use among engineers. Both 1D and 3D accelerometers exist, and their low cost and ease of use make them very popular.

Some drawbacks of contact sensors are limitations to certain frequency ranges and mass loading. Furthermore, depending on the magnitude and frequency of the disturbance in the object, accelerometers and other contact sensors are limited in their effectiveness to map vibrations across large areas due to the expense needed to attach enough sensors to analyze anything in the high frequency range. Fields comprised of short wavelengths require too many measurement points to be accurately reconstructed with traditional accelerometers. In this case, mounting accelerometers can be time consuming. Furthermore, they are too large in many instances to obtain the necessary

spatial resolution. Contact transducers with multidimensional capabilities also tend to be much larger than their 1D counterpart, and this added size and weight can distort a waveform significantly through an effect called mass loading. Overall, contact sensors are effective for simple, low frequency applications where only a few receivers are needed.

1.2.2 Noncontact Sensors

1.2.2.1 Advantages and Disadvantages

The second category of vibration transducers encompasses noncontact sensors, and laser Doppler vibrometers (LDV) are the standard in this area. Polytec PDV-100 point (1D) LDVs were the transducers chosen for integration into the multidimensional vibration measurement system developed for this thesis. LDV technology was first utilized to measure vibrating structures in the 1980's, but it did not become a common technique until the 1990's when advancements in software and hardware improved the performance of these devices. Since that time, LDV technology has continued to evolve resulting in vibrometers available in today's marketplace that are designed for specific applications and that boast frequency ranges of up to 40MHz with even the most basic point (1D) LDV capable of accuracies of ±0.5% under 10kHz. [Castellini et al. 2006] LDVs are optical sensors that take vibration measurements at a distance from the object of interest. Because of this, there is no mass loading effect to perturb the motion under study. The one exception to this is in MEMS applications where the heat produced by the laser beam is enough to cause heat loading effects on the object. LDV is a very popular alternative to accelerometers due to its noninvasive characteristics as well as its ability to efficiently and accurately scan the surface of an object in order to recreate high frequency

wavefields over large areas. LDV has become a mainstream measurement technique that has many benefits over traditional transducers such as accelerometers, and recent developments have continued to broaden the scope of projects to which LDV can be applied.

Disadvantages of this optically based technology include the line of sight and surface reflectivity requirements. While it is noncontact, the LDV must be able to actually "see" the point of interest in order to function correctly, and that point must be reflective enough to allow enough light to travel back to the LDV for detection. Point (1D) LDV is fairly common, but a drawback of 3D LDV is that it still developing and is very expensive. There is also no commercially available 3D LDV system that is sold as separate components in order to allow flexibility in its application. They tend to be big bulky devices with limited flexibility and adaptability in the field.

1.2.2.2 Physical Principles of LDV

In general, the term LDV is most often used to describe the original "point" or 1D LDV. This device simply measures the velocity of the vibration of an object in the direction of the laser beam path at a single point on the surface of an object. LDVs use an interferometer to split the direct beam from the laser head into a reference beam and a measurement beam. The basic idea is that the measurement beam is directed off the vibrating object and back to the interferometer where it is recombined with the reference beam and measured by a photodetector(s). The Michelson and Mach-Zehnder interferometers are the two basic interferometer configurations that are commonly used with the primary difference being the number of photodetectors that each employs (Michelson uses one and Mach-Zehnder uses two.) Polytec is one of the leaders in the

4

production of LDVs and LDV related devices, and they use the modified Mach-Zehnder interferometer configuration pictured in Figure 1. [Martarelli 2001]
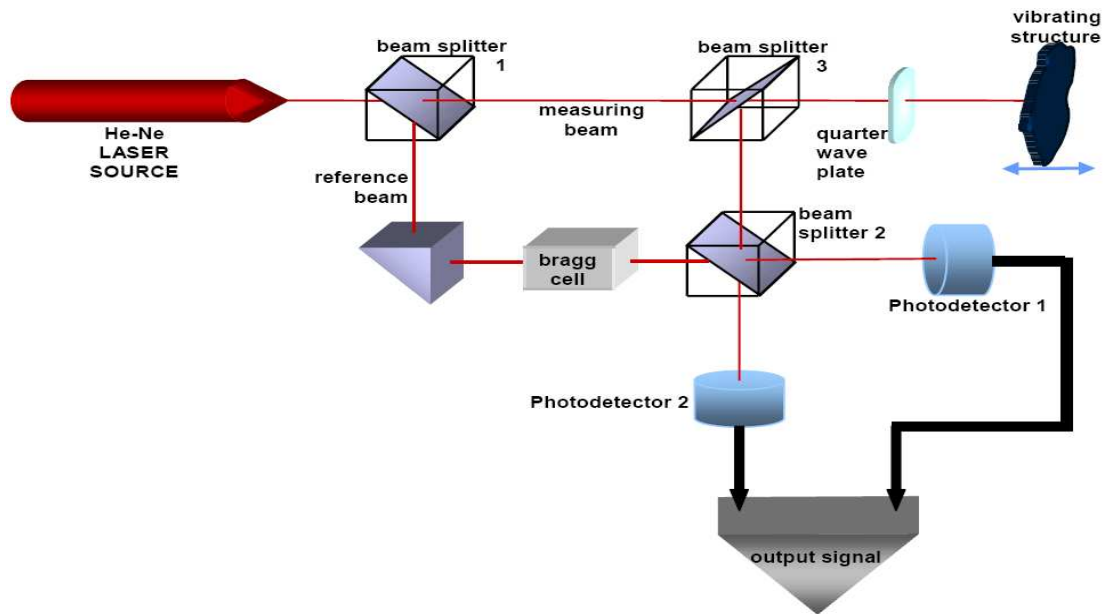
Figure 1: Modified Mach-Zehnder Interferometer [Martarelli 2001]

The important addition to the traditional Mach-Zehnder configuration is the Bragg cell located in the path of the reference beam. This device diffracts the incident beam into several orders, and one of the frequency shifted beams is used to determine the sign or direction associated with the velocity information received by the photodetectors. [Martarelli 2001] Use of the Bragg cell also gets rid of low-frequency thermal fluctuations.

This velocity information is received by the photodetectors in the form of the intensity (the number of photons) of the light wave incident on them. When the two light waves are measured, a frequency shift due to the vibration of the object will be detected. This frequency shift is known as the Doppler Effect. With a light wave in this setup, the beam actually experiences what is commonly known as a "double Doppler shift." When the light wave is traveling from the interferometer to the vibrating target, the system is

5

parallel to a stationary source and a moving observer, and the frequency shift on the beam is

$$\Delta f = \frac{u\cos(v)}{\lambda}$$

(1)

where λ is the wavelength of light, u is the velocity of the moving surface, and v is the angle between the propagation direction of the light wave and the vibration direction of the moving surface. The moving object then reflects the shifted beam back to what is now the stationary receiver in a moving source-stationary observer system resulting in another frequency shift that appears slightly more complex

$$\frac{\Delta f}{f} = \frac{\frac{u}{c}\cos(v)}{1-\frac{u}{c}\cos(v)}.$$

(2)

For the case of vibration measurements however, the assumption can be made that the displacement of the surface at the measurement point, u, is very small compared to the speed of light in the medium, c, and when the expression is expanded using Taylor series expansion in $\frac{u}{c}$ the higher order terms can be ignored, and the two cases yield the same frequency shift. The combination of the two shifts results in an overall frequency shift of the measurement beam of

$$\Delta f = \frac{2u\cos(v)}{\lambda}.$$

(3)

This frequency shift that is derived from the oscillations in the intensity detected by the photodetectors is then converted to the vibration velocity through the LDV's digital signal processing unit [Martarelli 2001].

6

The final physical property that must be addressed in relation to LDV is the concept of laser speckle. Lasers generate a coherent beam of light comprised of many lower intensity light waves with various phase shifts. The major coherent beam is referred to as the primary beam, and the lower intensity, phase-shifted waves that make up the primary beam are known as elementary beams. When a laser is incident on an optically rough surface, its reflection exhibits a speckle effect caused by the constructive and destructive interference of the elementary beams within the primary coherent laser beam. Figure 2 illustrates this phenomenon.
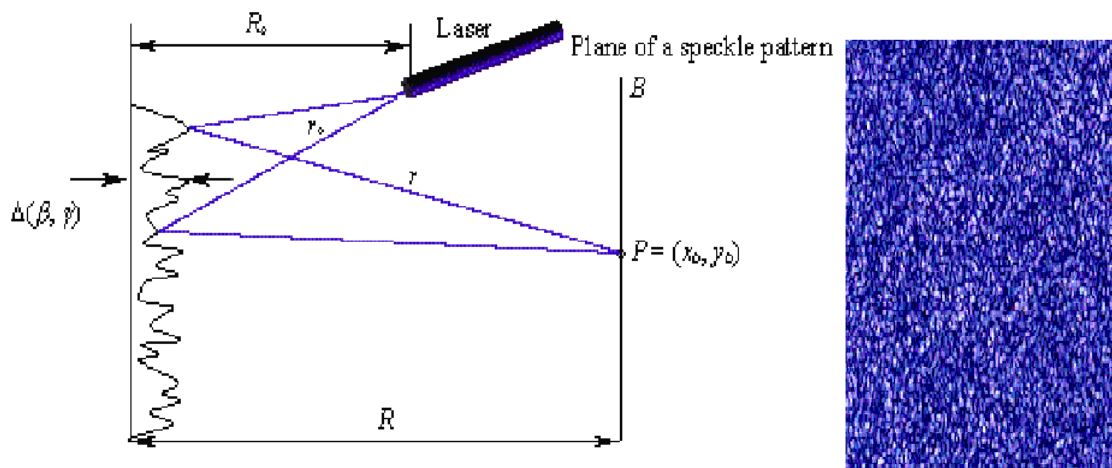
Figure 2: Illustration of the laser speckle effect [Langston 2005]

It is this speckle effect and the noise that it creates that is the most common limitation to many LDV applications. The speckle effect is magnified by certain characteristics on the surface of an object and this has a strong influence on the intensity of light reflected back to the photodetectors in the LDV. Because it is a characteristic of all lasers used in LDV, this noise must be dealt with in some form in every LDV related application. When considering how to appropriately accommodate for speckle noise, it is very important to

note that the speckle pattern created by this effect responds to the displacement of the object (or the beam in scanning applications) in a systematic way. In other words, if a laser is scanned along the same path, it will see the same series of speckle patterns corresponding to each point on each pass, and this characteristic causes the speckle noise to exhibit periodic features that mirror the scan frequency in scanning applications. The level of the speckle noise also increases proportionally to the scan frequency. This noise can and has been modeled for certain applications, but usually, the characteristics can be seen by simple data collection before beginning an experiment. A simple FFT of the base level noise time signal will reveal that the majority of the speckle noise is focused around the peaks of the scan frequency and its harmonics. This knowledge makes the selection of scan speed very important with respect to speckle noise. The scan frequency must be chosen so that neither it nor its harmonics are near the vibration frequencies of interest of the object being analyzed. If this requirement can be met, the speckle noise will not pollute the signal being measured. [Ewins et al. 2006]

Speckle noise is much easier to deal with in multidimensional point measurement applications than many scanning applications because one only has to deal with a single moving object (the surface of interest) rather than two (the surface and the scanning laser). In order to limit the speckle noise while developing and validating the various aspects of this system, metallic targets were primarily used as surfaces of interest and their reflectivity was often enhanced with Polytec reflective tape. While the limitations of the PDV-100 point LDVs are important, the work involved in this thesis focused on the development of the entire system and its capabilities. A list of the technical specifications and other information pertaining to the PDV-100's is listed in Appendix A.

      This thesis details the development and validation of a laser Doppler vibrometer-based measurement system that is capable of quantifying not only the normal vibration of a solid body but also the component of vibration that is parallel to the plane containing the surface of interest. This motion parallel to the plane containing the surface of interest will be referred to as the in-plane motion or vibration. LDV manufacturers produce various devices that capture 3D measurements in a couple different ways, but the most popular method involves using three laser heads in a configuration that can be used to decompose the measured signals into not only the normal vibration of the surface of an object but also the two orthogonal in-plane components of that vibration. Polytec's 3D vibrometer, utilizes three small laser heads contained in a single box. The two heads located on the sides are oriented in the same plane at equal but opposite azimuth angles with respect to the center head. These two heads are used to gather information that can be decomposed into the normal velocity component as well as the in-plane velocity component parallel to the plane of the two heads. The center head is raised out of the plane of the other two heads in order to gather information that can be decomposed along with the information gathered by the other heads into the in-plane motion perpendicular to the plane defined by the two outer heads. This additional measure of having the center LDV on a different plane than the other two LDVs is a complication that is unnecessary for the applications of this system, and therefore, a slightly simplified two-dimensional version of this method was chosen for the implementation in The Wave Physics lab. The chosen configuration measures the normal component of motion and the single in-plane component of motion parallel to the plane of the LDVs. The simplicity of implementation

was the motivation for this choice in addition to the fact that most of the research that will be conducted in the future will only require the knowledge of a single in-plane component of vibration. It is difficult to measure a single in-plane component accurately, so an attempt to measure both orthogonal in-plane components was out of the scope and need of this project at this point in time.

1.3 Motivation and Goals

Polytec and other LDV manufacturers produce various devices that capture 3D measurements in a couple different ways, but the most popular method involves using three laser heads in a configuration that can be used to decompose the measured signals into not only the normal component of vibration but also the two orthogonal in-plane components of vibration. The work involved in this thesis focused on the development and validation of a slightly simplified, more flexible, and much cheaper two dimensional version of this concept. Significant steps were made toward the ultimate goal of a multi-beam system that will be able to take several simultaneous multidimensional measurements for the purpose of diffuse field monitoring.

Individual components were used to develop a system with an LDV configuration that could be easily altered for various applications involving samples of different materials, sizes, and geometries. The combined use of multiple Polytec PDV-100 point LDVs will provide not only multidimensional measurements but also scanning measurements and in-situ measurements outside the lab environment.

The goal of this system is to facilitate the exploration and discovery of areas and applications where 2D measurement may provide a more complete and precise view than

traditional 1D measurement regarding the physics of different phenomena. 2D measurements have the capability of providing useful additional information for the recreation of wave fields, the study of polarization, and tomographic imaging. The hope is that this information will lead to valuable findings such as more effective ways to measure the acoustoelastic effect or to identify mode conversion at cracks or imperfections within materials. Efforts will be made to continually pursue and explore new areas such as these where 2D measurement may have an advantage over its conventional 1D counterpart.

1.4 Thesis Organization

This thesis will detail several important aspects of the development and validation of this system that is contained in Dr. Sabra's Wave Physics Lab in the Georgia Institute of Technology. Chapter 2 will discuss the physical principles and specifications of the various components employed in this work as well as their integration and functionality. This will include a detailed description of both the hardware and software utilized to construct and streamline the final system. Then, Chapter 3 will detail the actual process of obtaining the in-plane and normal vibration components based on the gathered data. A short description of how the LDV take measurements will lead to the derivation of the formulas needed to extract the necessary information from the data. Various issues directly related to this system's capabilities and limitations will be discussed, and an experiment that was conducted in order to validate the theory and derived expressions will be detailed. Chapter 4 will then discuss a more complex experiment that was conducted to demonstrate the systems capabilities through a real engineering application

of present interest. The goal of this experiment was to identify how stress effects the polarization at the surface of an aluminum plate under a range of compressive loads. The normal and in-plane components of the vibration were analyzed both independently and together using several different methodologies in an effort to determine what information could be extracted from the propagation of Lamb waves in an Aluminum plate under stress. It was determined that there is information in both components of motion as well as in the relationship between the two components. Finally, some conclusions will be drawn about the progress made in the development of this system and the future work that can be done to improve and broaden the application of the system.

CHAPTER 2

SYSTEM COMPONENTS AND INTEGRATION

2.1 Hardware Components

Individual components were integrated into the 2D measurement system, and an overall view of the system and its hardware components are shown in Figure 3. The following sections detail the various hardware components as well as pertinent information regarding their functionality and integration into the system. This is an optically based system that utilizes Polytec PDV-100 point LDV as discussed in detail in Chapter 1. Specifications of the PDV-100 can be found in Appendix A.
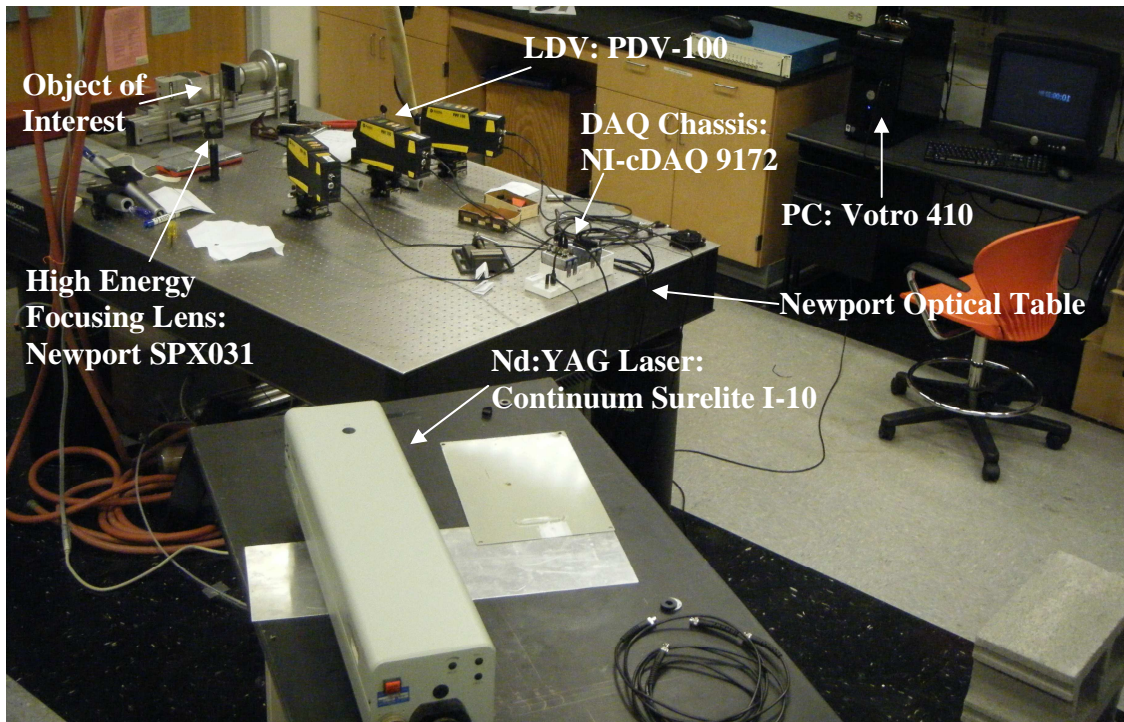
Figure 3: Comprehensive view of the 2D measurement system

2.1.1 Point Source: Continuum Surelite I-10

The excitation source chosen for this system was a Continuum Surelite I-10 (SL I-

10) Nd:YAG laser (Fig. 4 and 5). This Nd:YAG (neodymium-doped yttrium aluminum garnet; Nd:Y3Al5O12) laser is a high energy, solid state laser that is used to strike the object of interest, therefore, generating elastic waves in the object and creating vibration on the surface of the object. It is the vibration source in the system. Nd:YAG is a crystal that is utilized by the laser as a gain medium. [Siegman 1986] The SL I-10 optically pumps or excites the crystal with flashlamp. Then, through an optical switch called a Q-switch, light is released to travel through the laser cavity and toward the target. The use of this Q-switching technique is called pulse mode as opposed to other lasers which may operate in continuous mode.

Figure 4: Surelite SL I-10 Nd:YAG high energy laser bench used as a point source excitation

Figure 5: Power cooling unit and front control panel

An important capability of the SL I-10 is that it can be triggered by an external signal(s). There are two ways to trigger the SL I-10. Mode 1 triggering allows the internal clock to trigger the flashlamp while a single external signal is input into the laser to activate the Q-switch. According to the Continuum Surelight Manual, this is a very simple process as only a single 5V→0V square wave is needed, but the problem is that there will be a delay or jitter of ±10ns in the system, and the consistency of the resulting pulse will be in question. The laser cavity and the Nd:YAG are tuned to operate at a certain frequency (10Hz for the SL I-10) in order that the Q-switch may be activated at the precise time that the crystal is at the optimal energy level to produce a maximum energy pulse. Unless the flashlamp and Q-switch are operating together, there is no way to perfectly sync the two for the best possible performance.

Mode 2 is a more complicated way of externally triggering the laser, but it virtually eliminates the jitter and allows for the best performance of the laser. This mode uses two synced analog signals to both prime the crystal with the flashlamp, and release the Q-switch at precisely the right moment. Basically, one square wave pulses the laser at 10Hz, and a second shorter pulse-like square wave activates the Q-switch 180ms after one of the flashlamp cycles as shown in figure 6. [Continuum 1996]
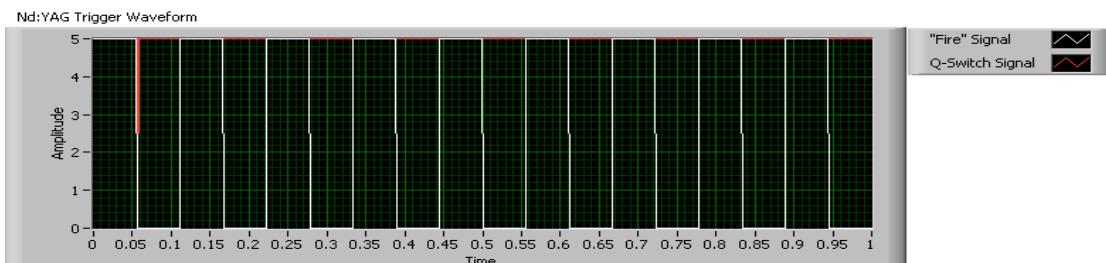
Figure 6: SL I-10 input waveforms for external triggering. The white square wave pumps the Nd:YAG crystal, and the red impulse Q-switches the laser by throwing the optical switch at precisely the right moment to allow the energy to be released from the laser head.

Finally, in order to achieve the most repeatable and smallest source possible, the light from the Nd:YAG laser was focused using a Newport model SPX031 plano-convex lens. This is a high energy lens made of uncoated, extremely pure fused silica. The effective focal length (EFL) of the lens is 500mm, and its diameter is 25.4mm. This lens was used in all of the studies and applications involved with the development and validation of this system. There is also a second lens in the lab of identical makeup and diameter to the SPX031 but with EFL 350mm. Proper focusing enables the Nd:YAG laser source to act similar to an ideal point source capable of generating a broadband range of frequencies within the target. A point source is an energy source of negligible size compared to the wavelength of the generated waves.

2.1.2 National Instruments Control Hardware

Some LDVs are bought in conjunction with hardware and software all prepackaged and ready to install, but the PDV-100's used in this study were bought independently of any data acquisition (DAQ) software or hardware. Again, this was done for purposes of flexibility so that the same DAQ system could be used to interface with various other research projects as well as future research on this project. The DAQ platform chosen for use in The Wave Physics lab was the National Instruments CompactDAQ Chassis (NI-cDAQ 9172) shown in figure 7. This is basically a device that facilitates the interaction between the computer and up to eight input/output (I/O) modules that have various capabilities. Complete specs of the NI-cDAQ-9172 can be found in Appendix B.

Figure 7: NI cDAQ-9172 CompactDAQ Chassis used to interface hardware with Labview software through analog input modules, an analog output module, and an analog trigger module.

For this multidimensional vibration measurement system, three different types of modules were utilized to perform the necessary tasks of analog input, analog output, and analog triggering. In order to acquire the analog signal from the LDVs, two NI-9215 modules were utilized. Each module has four channels that sample at rates up to 50k samples per second per channel. This sample rate is sufficient because the LDVs only collect data up to 22kHz. These modules were very easy to implement and were utilized for all of the initial testing of the LDVs. As the system progressed, external triggering of the laser became important in order to synchronize the point source with the DAQ. The details of the various ways to do this can be found in section 2.1.2. In order to generate the necessary analog output signals for mode 2 triggering, an NI-9263 analog output module was implemented. This module is very similar to the NI-9215, but it is capable of analog output instead of analog input. Finally, after independently integrating the DAQ and the Nd:YAG laser trigger to the computer through the National Instrument interface, it was determined that these two aspects of the system had to be synchronized to facilitate the averaging of signals upon collection as opposed to having to average the signals post collection. Although the NI-9215 is capable of collecting analog input, analog triggering is not compatible with this model, and an NI-9205 module had to be purchased and

17

integrated into the chassis in order to perform this crucial function. A hardware trigger was needed to coordinate analog I/O due to the inaccuracies of Windows built in clock and the debilitating effect that would have had on a software trigger. Windows internal clock simply is not precise enough to allow the use a software trigger in a system where signal averaging is important. Instead, the "Q-switch" signal generated by the NI-9263 (shown in red in Fig. 6) was used to trigger the actual collection of the data by the NI-9215's. Our application does not necessarily require knowledge of when this took place or triggering of the Nd:YAG laser at a specific time, but simply a coordination of the two aspects.

2.1.3 Point Laser Doppler Vibrometer: Initial Operational Tests and Functionality of the Polytec PDV-100

The measurement performance of the PDV-100s (Fig. 8) were first assessed in order to shape the direction and capabilities of the final system.

Figure 8: Polytec PDV-100 LDV non-contact optical transducer

The following initial tests were performed in order to gain a working understanding of the capabilities of these LDVs:

- Functionality and Synchronization:
  - Two LDVs were placed approximately 1.5m from and with incidence angle approximately normal to an aluminum plate. Both LDVs were directed to measure the same point on the surface of the plate. Signals were collected simultaneous with the two LDVs using the same filter and sensitivity settings. The PDV-100 has several built in high and low pass filters and three sensitivity levels that were all tested for basic functionality. Different signals were generated in the plate using the Nd:YAG laser source for high frequency (up to the 22kHz limit of the PDV-100's) and a hammer source for low frequency (0-500Hz), and these signals were collected with the two LDVs on each of the different settings to verify that the filters and sensitivity settings functioned properly. After all the signals were collected using each of the filters and settings, they were processed in the time and frequency domain using MATLAB (See Appendix C), and the pair of signals collected for each setting combination were compared for correlation in both domains. Then, one of the LDVs remained in the configuration to be used as a reference signal, and the second LDV was replaced by one of the other LDVs in inventory, and the procedure was repeated. This procedure was carried out for each LDV-reference LDV combination, and it was concluded that each of the LDVs showed very good agreement with the others and was in proper working order.

- Surface Test
  - Signals were collected with a single LDV directed at objects with various surface reflectivities to order to better understand how well the PDV-100's function on surfaces that have low reflectivity. It was observed that strong signal intensity could be obtained even off of surfaces such as brown cardboard and gray porous shipping foam.
- Mirror Test
  - Another of the initial tests was done by implementing mirrors into the experimental setup in order to determine whether they would result in any signal distortion or attenuation. One LDV was aimed directly at an aluminum plate, and a second LDV was directed off of three mirrors before being directed at the same point on the plate as the other LDV and at an approximately equal angle of incidence. It was found that several plane mirrors could be used without any discernable degradation of the signal. During this process of initial testing, it was noticed that the frequency spectrums of the time signal data gathered by each of the LDVs frequently showed a peak at 5400Hz. It is still unclear exactly what causes this peak, but the knowledge of this phenomenon was very useful through the development and validation of the system.
- Robustness to misalignment
  - With the three LDV configuration for 2D measurement, one of the LDVs was setup to measure only the normal component of the motion of the surface, so it was very important to identify how precise the alignment of

the middle LDV had to be. An LDV was setup at an angle of incidence that appeared to the naked eye be "normal" to the surface. The object was excited, and the velocity data was collected. Then, the LDV was rotated to either side of the initial measurement point by approximately 1.25cm collecting a signal at each point. The object was approximately 90cm from the LDV, so it was apparent even to the naked eye (with the aid of the perpendicular lines on the optical table), that the LDV was not directly normal to the surface for the side measurements. The LDV was fixed to the table and the side measurements were taken by changing the angle of the LDV and, therefore, the angle of incidence on the surface. At low frequency, the wavelength of the object is sufficiently long enough (~1m) that the motion of the surface was uniform over the 2.5cm line along which signals were collected. Figures 9 and 10 show the time signals and frequency spectrums plotted on top of each other for comparison.
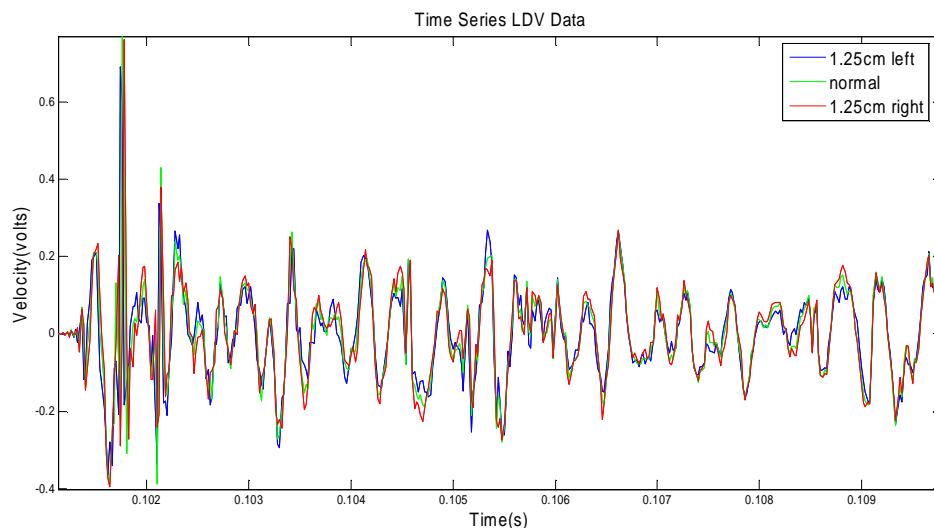
Figure 9: Comparison of time signals collected with obvious misalignments in the orientation of the LDV. Despite the misalignments, all three signals show good correlation throughout the duration of the signal.

21
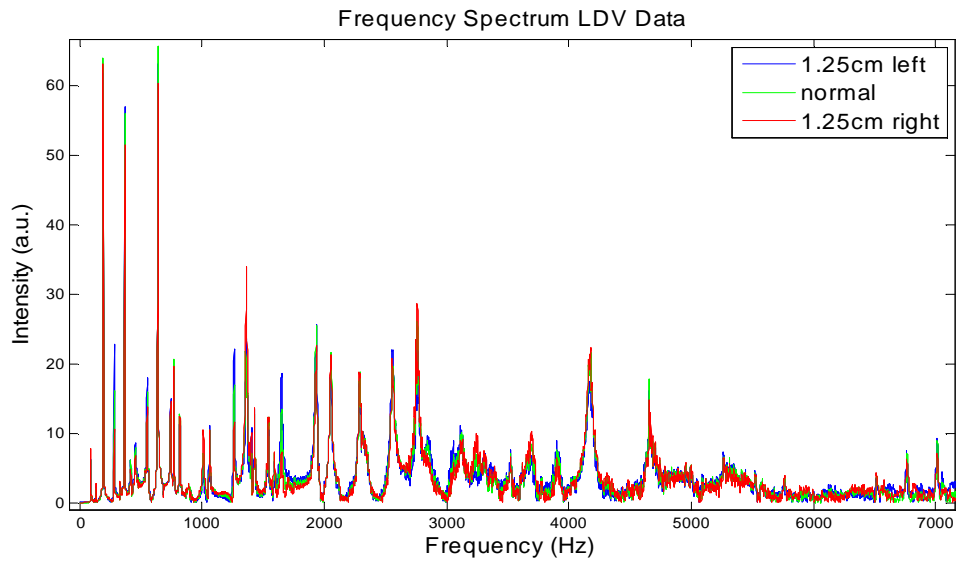
Figure 10: Comparison of frequency content of signals collected with obvious misalignments in the orientation of the LDV. Despite the misalignments, all three spectra show good correlation over the broadband frequency range.

It is apparent from these images that there is little variation in phase or amplitude of the time signal and similar variation in the frequency spectrums for the three cases considering the extreme magnitude of the misalignment. While the angle variations involved in this quick study were relatively small at this distance from LDV to target, the visual aids that are present in the setup cause the changes to be very noticeable. This shows that the proposed setup that will be discussed in more detail in Chapter 3 is fairly robust and even noticeable misalignments will not cause huge errors in the measurement.

2.2 Software: NI Labview 8.5.1

The choice of the cDAQ chassis for DAQ led to Labview becoming the software platform by which this measurement system was operated. Labview is a visual code that is intuitive on a basic level. The visual commands that appear to the user as simple icons of various shapes and sizes often contain embedded functions, commands, assumptions, and requirements unapparent to the user until errors are encountered. As the hardware

was integrated and tested for functionality and performance, simple Labview codes or Virtual Instruments (VI's) were written for DAQ and Nd:YAG laser triggering in order to facilitate the initial tests of functionality discussed in section 2.1.

One goal of the development of this system was to create something that could be used for future work in the lab for years to come, so ease of use and efficiency were of paramount importance when writing the VIs. This vision led to the development of a VI that utilizes a producer/consumer format to facilitate and synchronize all components of the entire measurement system. This format uses a queue to manage information operating in two separate loops at two different rates. After the physical channels and basic parameters are defined by the VI, a queue is created that serves like a controllable buffer. In the producer loop, the signals for triggering the Nd:YAG laser are generated and output which also triggers the "acquire data" command. At this point, data is collected for the defined number of channels for the duration of a single signal and is sent into the queue. Once in the queue, the data for the single signal moves into the consumer loop where it is divided by the number of total signals being averaged (in order to perform linear signal averaging) and stored. These loops operate independently, so while this first signal is being processed and stored, the Nd:YAG laser is being triggered and data is being acquired for a second signal that will undergo the same simple division and be added to the data stored in the consumer loop. Upon completion of the desired number of laser triggers and individual signal collections, the data in the consumer loop (the averaged signal) is written to a binary file and stored in the location identified by the user during the initial setup of the parameters of the VI.

Labview utilizes a "block diagram" where the actual code is written and

manipulated, and a "front panel" that serves as a graphical user interface. In addition to
file name and location, the user can seamlessly adjust the number of channels (up to 9)
collected, the sampling rate, the number of signals averaged, and the length of the signal
(in one second increments) directly on the front panel. With only a small amount of
manipulation of the block diagram, the total number of channels available can be
increased (with the addition of one NI-9215 module into the chassis for every four
channels added) to a total of 17 channels and the length of the signal can be adjusted
arbitrarily keeping in mind the requirements of the Nd:YAG triggering and the role that
plays in triggering the DAQ. Figure 11 shows a schematic of how the VI operates, and
the block diagram and front panel are in Appendix D.
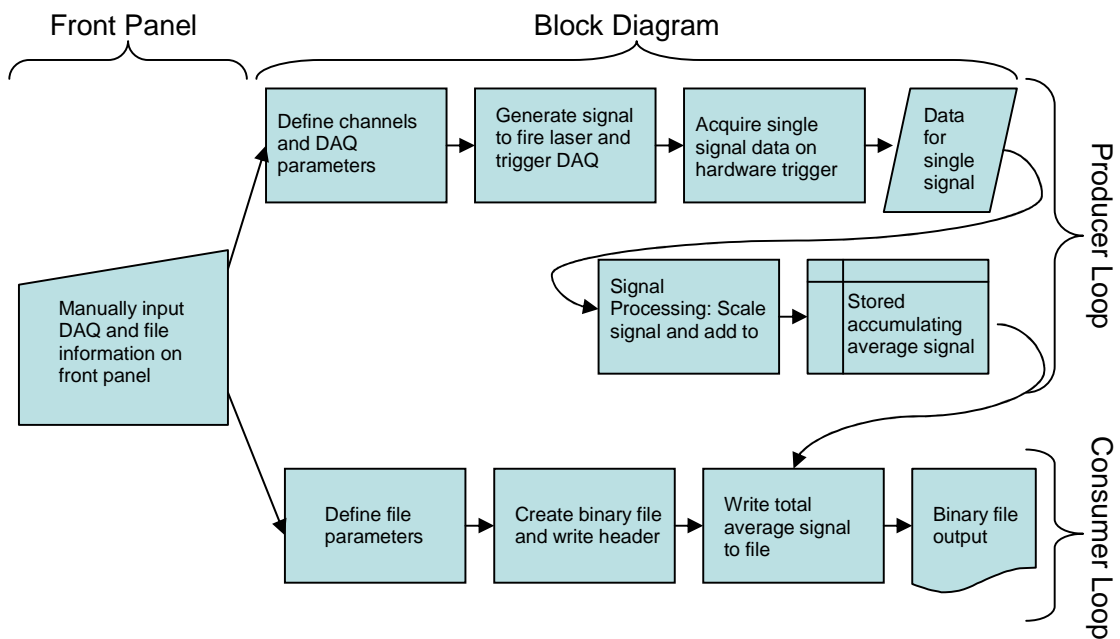
Figure 11: Flowchart illustrating the operation of the VI used to control the 2D measurement system.
Manual inputs are made by the user on the Front Panel, and the producer and consumer loops operate
independently and are contained in the Block Diagram.

A test was done to verify that the VI was actually computing a linear average of
all of the signals collected. One preliminary version of the VI that saved each of the

24

signals into individual files instead of averaging them was employed for this collection of individual signals. Then, the final VI with internal signal averaging capabilities was used to collect a single averaged signal immediately after the collection of the individual signals. MATLAB was used to compute a linear average of the individual files to plot on top of the signal generated using the internal averaging of the Labview VI, and the results can be seen in Figure 12. The experimental setup at this point in the development of the system was not optimal, so its repeatability was not the best, but it is obvious from this figure that the VI was in fact computing an accurate linear average of the collected signals.
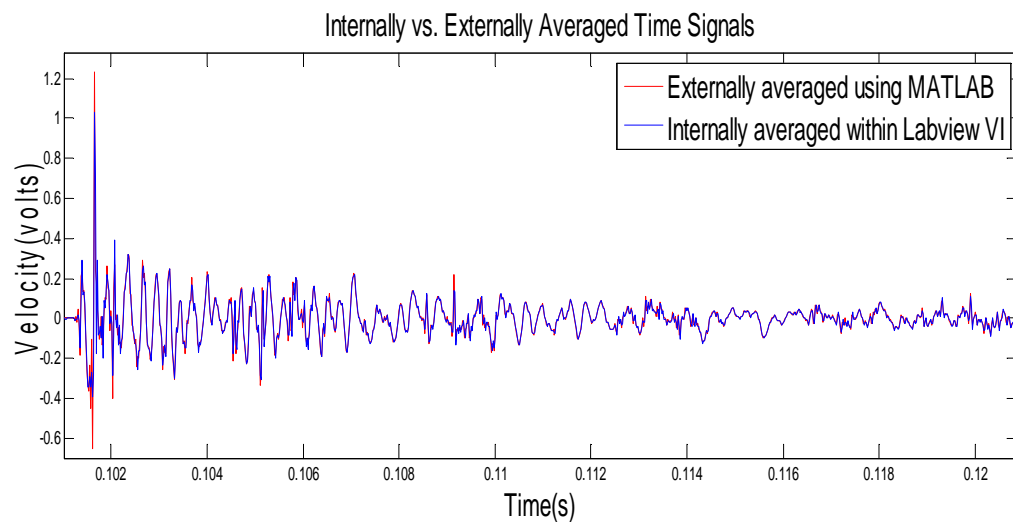
Figure 12: Comparison of a signal that was averaged within the developed Labview VI and a signal calculated from many individually collected files and then averaged externally in MATLAB.

CHAPTER 3

MEASUREMENT OF NORMAL AND IN-PLANE COMPONENTS OF MOTION

3.1 Overview and Objectives

A 2D optical system was implemented to measure the normal and in-plane components of motion. This system leverages the geometry of the optical table to allow precise angle calculations to be made through very simple distance measurements. In order to validate this configuration and system capabilities, a study was performed in which signals were collected with the LDVs and a PCB 356A32 triaxial accelerometer.

The goals of the study were two fold. First, the signals for the in-plane and normal components of the vibration of an aluminum plate would be gathered with both the accelerometer and the LDV configuration. The accelerometer was used as the control, and the primary objective was to demonstrate that the same signal was collected with each transducer. The second objective of this study was to determine if the oblique angle of the side LDVs affected the accuracy of the extracted in-plane vibration signal. This was important because there was speculation that there would be a tradeoff between the accuracy of the in-plane measurements and the incidence angle with thoughts that a smaller oblique angle measured from the axis parallel to the plane of the plate would result in a stronger more accurate in-plane vibration signal than larger angles. This would limit the system because LDVs are dependent upon the ability to gather reflected light, so these smaller incidence angles would have also resulted in a lower intensity and subsequent lower signal-to-noise ratio (SNR) for LDV measurement. According to the theory discussed in the next section, the signals from the side LDVs should be able to be

26

decomposed into accurate normal and in-plane components of motion regardless of their incidence angle assuming there is sufficient reflection from the measurement surface to allow the LDV to collect with good SNR. Despite this, there was strong sentiment to pursue such a study to verify this experimentally.

3.2 Signal Decomposition:

3.2.1 Geometry of extracting the in-plane and normal components

One of the biggest obstacles overcome through the process of this system development was verifying the model that had been derived with regard to how the point LDVs collect data and what it is that they actually measure. There was some initial uncertainty about exactly what was measured along the optical axis of the laser and how to apply that knowledge. As it turned out, the Polytec LDV measures a linear combination of the velocity components of the surface of interest. Figure 13 shows how the three lasers are setup in the 2D configuration as well as a visual representation of what each LDV actually measures.
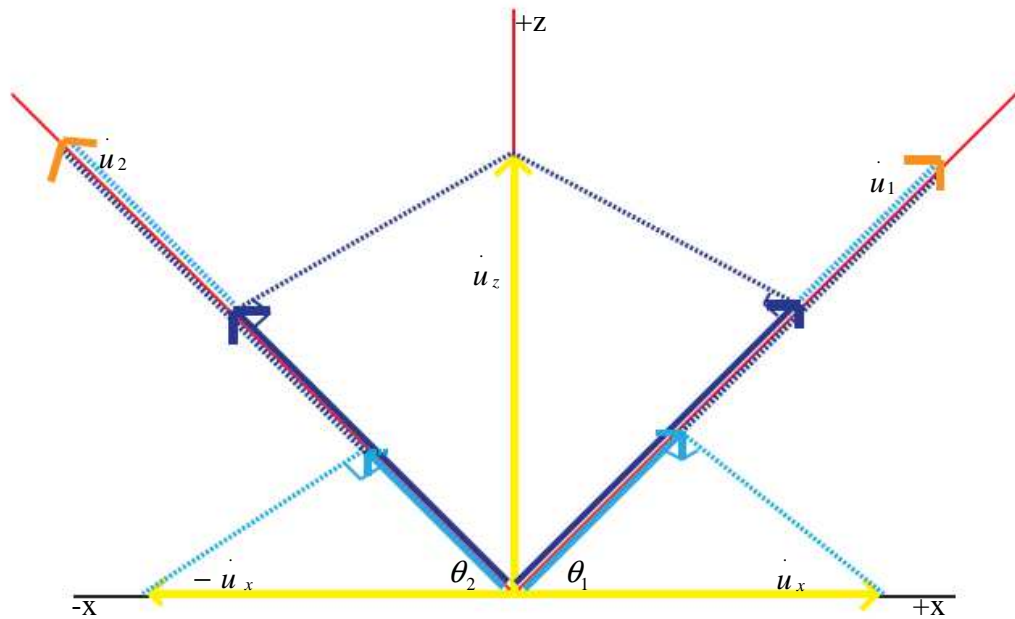
Figure 13: Overhead illustration of what the LDV actually measures; black line = plate, red lines = optical axis of LDV's

According to the Polytec 3D LDV user's manual, each of the lasers essentially measures a portion of the different components of the velocity at a point. For the coordinate system defined in Fig. 15, this means that

$$\dot{u}_1 = \dot{u}_x \cos\theta_1 + \dot{u}_z \sin\theta_1 \tag{4}$$

$$\dot{u}_2 = -\dot{u}_x \cos\theta_2 + \dot{u}_z \sin\theta_2. \tag{5}$$

Based on this knowledge, the in-plane (x-axis) and normal (z-axis) velocities can be defined from the measured components using the equations

$$\dot{u}_x = \frac{\dot{u}_1 \sin\theta_2 - \dot{u}_2 \sin\theta_1}{\cos\theta_2 \sin\theta_1 + \sin\theta_2 \cos\theta_1} \tag{6}$$

$$\dot{u}_z = \frac{\dot{u}_1 \cos\theta_2 + \dot{u}_2 \cos\theta_1}{\cos\theta_2 \sin\theta_1 + \sin\theta_2 \cos\theta_1} \tag{7}$$

The geometrical setup developed for this system guarantees good agreement between the angles such that the assumption that $\theta_1 = \theta_2 = \theta$ is valid. Based on this equal angle assumption, the equations become

$$\dot{u}_x = \frac{\dot{u}_1 - \dot{u}_2}{2\cos\theta} \tag{8}$$

$$\dot{u}_z = \frac{\dot{u}_1 + \dot{u}_2}{2\sin\theta}. \tag{9}$$

All four of these equations (6-9) show that neither the normal velocity component, $\dot{u}_z$, nor the in-plane component, $\dot{u}_x$, are dependent on the normal component measured by the middle LDV. However, this extra measurement was taken for two reasons. First, the middle LDV which measures $\dot{u}_z$ directly was used throughout this study to verify that the experimental setup was precise by facilitating a comparison of the 'measured' $\dot{u}_z$ and the 'calculated' $\dot{u}_z$. It was this measured $\dot{u}_z$ that was most often used as the normal velocity component throughout this thesis.

The second reason for using the middle LDV is so that, if the system is moved to an area where the geometry of the table can no longer be utilized to take direct angle measurements but the angles of the side LDVs can be assumed to be equal, equation 9

stated above can be used to calculate θ. In theory, it appears that equation 9 can be

solved directly for θ, but in practice, $\dot{u}_z$ is a time series which contains many null values,

and the resulting fraction defining θ goes to ∞ at each of these points. Therefore, an

alternate method must be used to evaluate θ based on the known relationship to the three

measured values. The angle, θ, can be calculated in each of the following ways. First, the

measured value for $\dot{u}_z$ can be plotted on the y-axis and $\dfrac{\dot{u}_1+\dot{u}_2}{2}$ on the x-axis of a simple

xy-plot. Then, a linear fit can be done of the resulting plot. From the linear relation (Equ.

9), it is known that the slope is equal to $\dfrac{1}{\sin\theta}$ so θ can be easily determined. The second

way is similar but slightly more robust. Each side of equation 9 can be cross-correlated

with $\dot{u}_z$ as shown in equation 10.

$$\dot{u}_z \otimes \dot{u}_z = \frac{1}{\sin\theta} < \frac{\dot{u}_1+\dot{u}_2}{2} \otimes \dot{u}_z > \qquad (10)$$

where $\otimes$ represents the cross-correlation and the coefficient, $\dfrac{1}{\sin\theta}$, can be determined

allowing θ to be known. With the plate as a target and using only a few reflections, the

signals are fairly simple, and each of these methods results in fairly accurate angle

measures.

3.2.2 Error Analysis of System Configuration

After determining the relationships between the measured signals and the normal

and in-plane velocity components, an error analysis was performed in order to determine

how sensitive the system was to uncertainties in several areas. Four major sources of

error were identified, and they will be referred to as alignment error, parameter error,

noise, and measurement error.

Alignment error is the error resulting from imperfections in the assumption that $\theta_1 = \theta_2 = \theta$. Equation 8 was the working equation for all signal decomposition (remember $\dot{u}_z$ was defined as the measured signal from the middle LDV), and this equation is a simplified version of equation 6. It is impossible to guarantee that two angles in this system are identical, so the reality is that

$$\theta_2 = \theta_1 + \Delta\theta \tag{10}$$

where $\Delta\theta$ is some error defined by the difference between the two actual values of θ. For simplification, θ_1 is taken to be known, and all alignment error is attributed to misalignment in θ_2. Based on this knowledge, the actual value of the in-plane velocity component in the +x-direction can be defined as

$$\overset{\wedge}{\dot{u}}_x(\theta_1,\theta_2) = \dot{u}_x(\theta_1,\theta_1 + \Delta\theta) = \dot{u}_x(\theta_1,\theta_1) + \Gamma\Delta\theta \tag{11}$$

where Γ is an error term related to $\Delta\theta$, and $\dot{u}_x(\theta_1,\theta_1)$ denotes the value defined in equation 8 for equal angles. Direct substitution of equation 11 into equation 6, along with first order expansions of the individual sine and cosine terms and then again of the resulting denominator lead to the relation

$$\overset{\wedge}{\dot{u}}_x(\theta_1,\theta_1 + \Delta\theta) = \dot{u}_x(\theta_1,\theta_1) + \Delta\theta \left[\frac{\dot{u}_1}{2\sin\theta_1} - \dot{u}_x(\theta_1,\theta_1)\left(\frac{\cos^2\theta_1 - \sin^2\theta_1}{2\sin\theta_1\cos\theta_1} \right) - \frac{1}{2\cos\theta_1}\frac{\partial u_2}{\partial\theta_2}\bigg|_{\theta_2=\theta_1} \right] \tag{12}$$

Leveraging the geometry of the optical table in designing the symmetric LDV configuration was the most effective way to minimize this alignment error.

Parameter error is also very important when evaluating the accuracy of this system. This error involves inaccuracies in determining the value of θ used for the calculation of the in-plane velocity component using equation 6. By taking the simple derivative of this equation with respect to θ, it can be seen that

$$\frac{d\dot{u}_x}{d\theta} = \frac{\dot{u}_1(\theta) - \dot{u}_2(\theta)}{2\cos\theta}\tan\theta + \frac{1}{2\cos\theta}\frac{\partial(\dot{u}_1(\theta) - \dot{u}_2(\theta))}{\partial\theta}.$$ (13)

This demonstrates that $\dot{u}_x$ changes proportionally to $\tan\theta$ with variations in θ, and both terms go to ∞ as $\theta \to \pi/2$. When designing the setups for the various experiments conducted using this system, special attention was made to use the geometry of the optical table to facilitate the most simple and accurate distance measurements possible. Many times, the fixture that supported the object of interest was not fixed to the optical table, and posts that could be fixed to the table were used to take short, accurate distance measurements using digital calipers.

The third source of error is simple noise in the signals caused by various sources. Sometimes these sources can be identified and eliminated or worked around, but often, the noise level is just something that must be dealt with in the analysis. Signal averaging was the major function of the DAQ VI that negated much of this noise, and this averaging along with the optical table was able to achieve very high SNR where the noise was several orders of magnitude lower than the signal. Because of this, noise was not a factor in any approaches to signal analysis used in this thesis.

Finally, there is the inherent measurement error of the LDVs. According to the specifications provided by Polytec, the calibration accuracy for the analog output of the PDV-100 is ±1% in the frequency range from 20kHz-22kHz. This places LDV error at

least two orders of magnitude below the maximum signal level in most cases, but it

should be considered when making comparisons to other transducers. Table 1

summarizes each source of error and the accommodations integrated into the system to

handle each.

Table 1: Summary of error sources and steps made to mitigate their impact

Type of Error	Accommodations
Alignment error: $\theta_1 \neq \theta_2$	Symmetric LDV configuration based on table geometry
Parameter error: inaccuracies in measuring θ	Using objects fixed to the table to leverage the table's geometry in order to make distance measurements small enough for digital calipers
Noise	Signal averaging; vibration isolation system of optical table
Measurement error	Purchase high quality Polytec LDVs

3.3 Experimental Setup

As implied previously, only two LDVs are needed to decompose their collected

signals into the normal component and the in-plane component of motion parallel to the

plane of the LDVs, but the configuration utilized here employs three LDVs. All three

LDVs in this setup were located in the same plane and focused on the same point on the

surface of the Al plate which was the target for this experiment. The middle LDV was

aligned normal to the plate, and the two outer LDVs were located equidistant from the

middle LDV on each side and in a line parallel to the plate. This configuration used the

geometry of the optical table to allow for very precise angle measurements. When

focused on the point defined by the normal LDV, the outer LDVs had angles of incidence

that were very precisely equal and opposite. In order to determine the best angle of

incidence for data acquisition, the side LDVs were placed at five different locations in

order to collect data with five different angles of incidence (45º, 60º, 73º, 80º, 83º). These

angles were somewhat dictated by the geometry of the table, but they allowed for a broad range that covered most of the possible configurations for this system.

The Al plate that was used as the target for this experiment was 46cm x 30.5cm x .5cm. It was scrap metal so the exact alloy specifications are unknown. In order to damp some of the reflections and simplify the signal, the edges were covered with VanAken International modeling clay. The clay covered approximately .75cm along all the edges on both sides of the plate, and it was approximately .25cm thick. All edges were covered with clay with the exception of portions of the 30.5cm edges that were clamped Newport heavy duty rods using C-clamps. The rods were screwed into the optical table parallel to the line of LDVs which guaranteed that the plate remained in the plane normal to the middle LDV throughout the experiment. Figure 14 shows a schematic of the configuration defining angles and LDV designations according to the theory visualized in Figure 13.
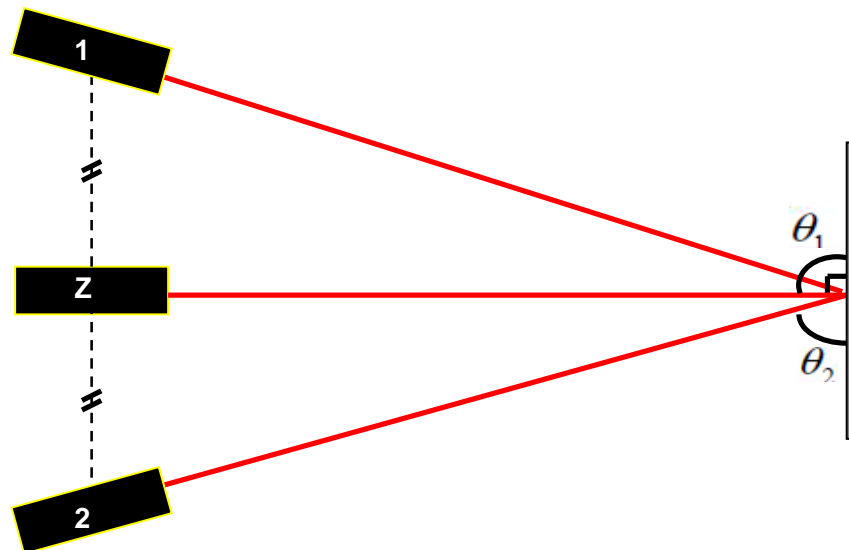
Figure 14: Experimental setup used to validate 2D LDV measurement system through direct comparison to a PCB Triaxial Accelerometer

34

The final portion of the setup for this experiment was the attachment and placement of the PCB 356A32 Triaxial Accelerometer. Several different approaches were taken when attempting to validate the effectiveness of the LDV configuration. First, data was collected separately. The Nd:YAG laser was used as a point source and signals were acquired using the LDVs, and then, the accelerometer was attached with a thin, round sticker called an electrode washer and the process of signal generation and collection was performed again. Due to the weight (5.4g) of the accelerometer, however, this data was immediately shown to be invalid. The mass loading caused by the accelerometer distorted the signal significantly, and no comparison could be made. Next, a symmetric setup was attempted where the LDV point of interest and the point of interest of the accelerometer (attached with the electrode washer) were placed at opposite orientations with respect to the source point of the Nd:YAG laser. While this produced better results, it was difficult to implement, and the error introduced by the additional measurements that had to be taken proved to contaminate the data to the point that there was still great uncertainty in the effectiveness of the technique.

Because the experiment was conducted at low frequency (100Hz-4kHz), the wavelength was sufficiently long (~1m) compared to the size (.45in cube) of the accelerometer to allow the top surface of the accelerometer parallel to the plate to demonstrate the same motion as the surface of the plate. Because of this, the LDV measurement point had to be placed directly on top of the accelerometer in order to collect both accelerometer and LDV signals simultaneously. With this setup, measurements by both transducers were affected by the mass loaded condition. A small piece of reflective tape was used on top of the titanium housing of the accelerometer in

order to guarantee maximum intensity for the LDVs, and the accelerometer was attached

with wax in order to create a seal with greater direct contact with the surface of the plate

than that provided by the electrode washer. Figure 15 shows a closer view of how this

was done as well as how the x-axis and z-axis were defined.
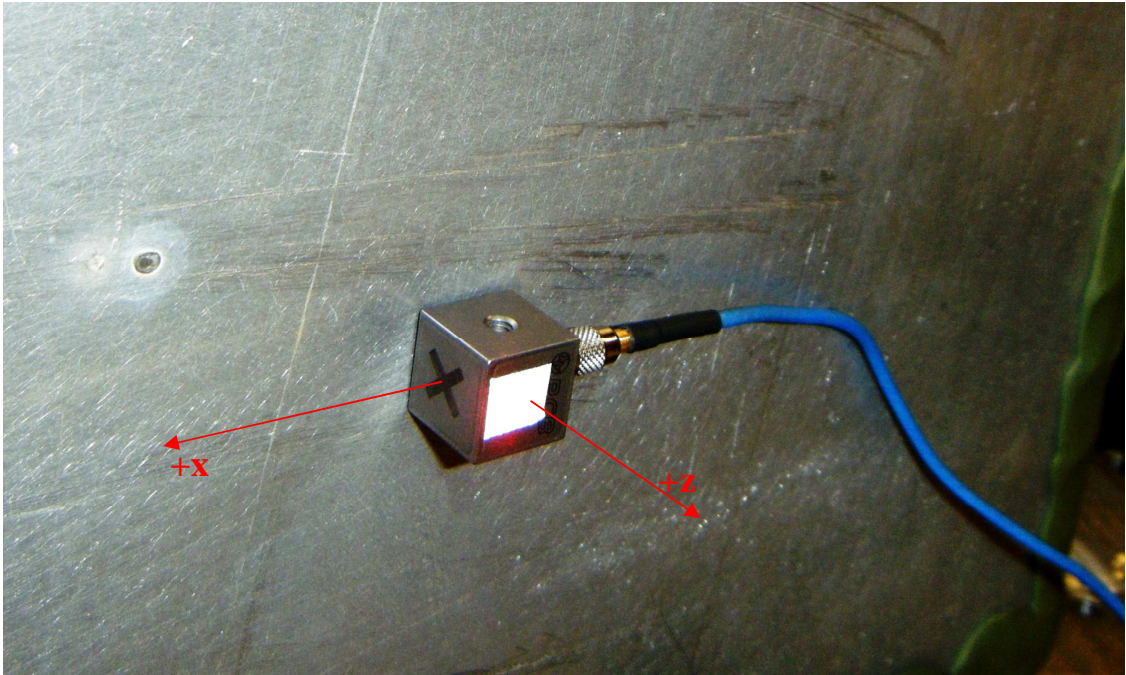
Figure 15: Zoomed view of the 3D accelerometer with the LDV measurement point directly on top. The orientation of the +x- and +z-axis were defined in this way for all calculations and explanations for this experiment and all others conducted during the work for this thesis.

3.4 Comparison with Accelerometer: Signal Processing and Results

3.4.1 Signal Processing

The data for both the LDVs and the accelerometer were acquired using the

Labview VI detailed in Chapter 2 with the LDVs set to collect with the low-pass filter set

on 22kHz and the high-pass filter (100Hz) turned on. The accelerometer does not have

any collection settings, but it only collects over a frequency range of 1Hz-4000Hz. Small

single channel amplifiers were used to collect the x- and z-direction accelerometer data in

order to enable proper functionality of the devices, but the gain was set to 1. Twenty-five signals of one second duration from each of the devices were collected and averaged with the VI.

For each oblique angle of incidence for the outer LDVs, three data sets were collected and saved in binary files to enable processing in MATLAB. The following is a general description of how each data set was analyzed. First, all collected signals were filtered from 100Hz-2.5kHz in order to accommodate for the different frequency ranges. The upper limit for the frequency range of the accelerometer is 4kHz, so 2.5kHz was selected as the upper limit for the filter in order to guarantee that all content over 4kHz was eliminated from the LDV signals. After the data was filtered using the 'filtfilt' function in MATLAB to preserve the phase of the signal, the three LDV signals were decomposed into the normal and in-plane components of the velocity of the surface of the plate. The value for the in-plane component was calculated using Equation 8, and the normal velocity was defined directly from the signal gathered by the middle LDV. The velocity data collected by the LDVs was then converted to acceleration using time differentiation. After the two components of motion had been defined in the time domain, each signal was cross-correlated with the corresponding component collected from the accelerometer using the 'xcorr' function in order to determine the time delay between the accelerometer and LDV signals. The PDV-100 has a response lag caused by the digital demodulation processing that is involved within each unit. Then, for each component of motion the corresponding time signals collected by each transducer were normalized by their maximum value and plotted together. The LDV signal was shifted to compensate for the different response times of the transducers in for the sake of comparison. Finally, both

signals for the accelerometer and LDVs were converted into the frequency domain using MATLAB's fast Fourier transform function, 'fft' and the absolute value of this result was normalized and plotted in order to compare each component's frequency spectrum to the spectrum of the signal collected by the other transducer.

3.4.2 Qualitative Comparison: Time Signals and Frequency Spectra

The following plots show a qualitative comparison between the time signals collected by the LDVs and those collected by the accelerometer. For these particular plots, the oblique angle of incidence of the outer LDVs was 73.50º from the plane of the plate. The signals compare very well in the time domain for both the normal and the in-plane components of the acceleration. (Fig. 16-21) There is slight disagreement in portions of both signals for various reasons probably related to the different sensitivities, calibration accuracies, and frequency responses of each of the transducers as well as the general differences in the physical principles of each measurement technique. Overall, however, the signals all show excellent correlation in the time domain. Notice how well the signals agree even into the coda or tail of the signals. (Fig. 19, 22) This shows that even as the signal becomes complex with reflections and diminishing amplitudes, the signals collected with the LDV and accelerometer still agree very well.
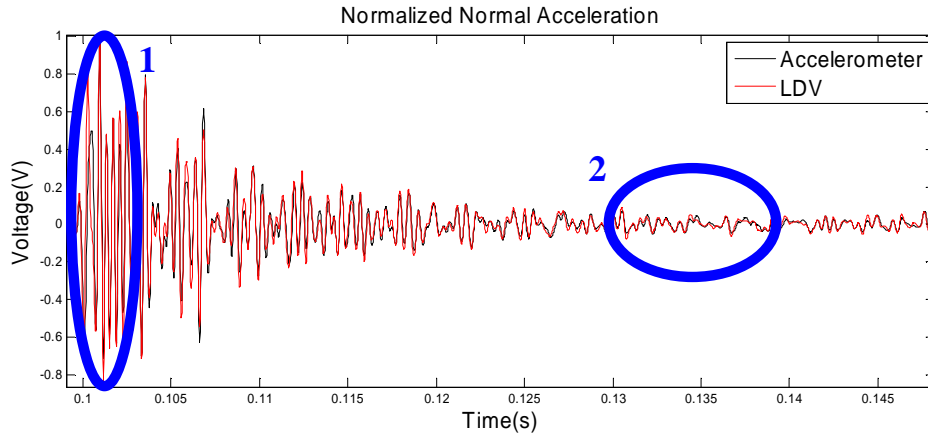
Figure 16: Comparison of the normalized normal acceleration time signals for the LDV (red) and accelerometer (black) signals. Areas of the signal designated 1 and 2 are zoomed in the following figures.
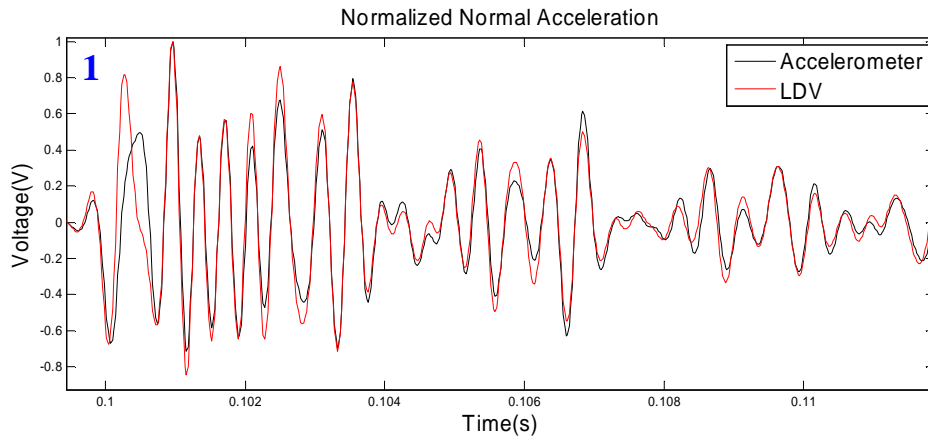
Figure 17: Zoomed comparison of the direct arrival and high amplitude portion of the time signals for the normalized normal acceleration collected with the LDV (red) and accelerometer (black).
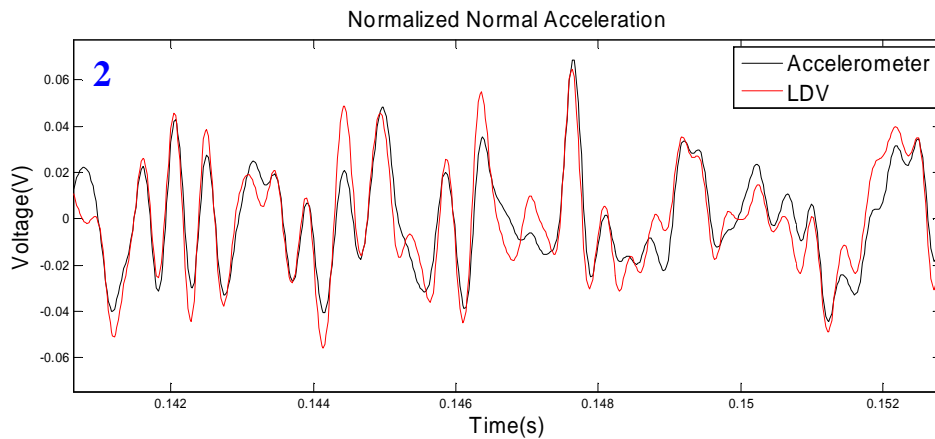
Figure 18: Zoomed comparison of the coda or low amplitude tail of the time signals for the normalized normal acceleration collected with the LDV (red) and accelerometer (black).

39
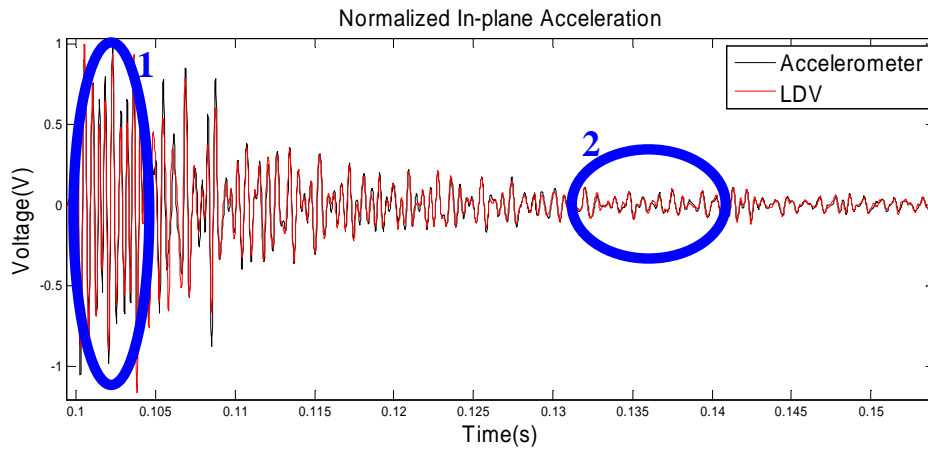
Figure 19: Comparison of the normalized in-plane acceleration time signals for the LDV (red) and accelerometer (black) signals. Areas of the signal designated 1 and 2 are zoomed in the following figures.
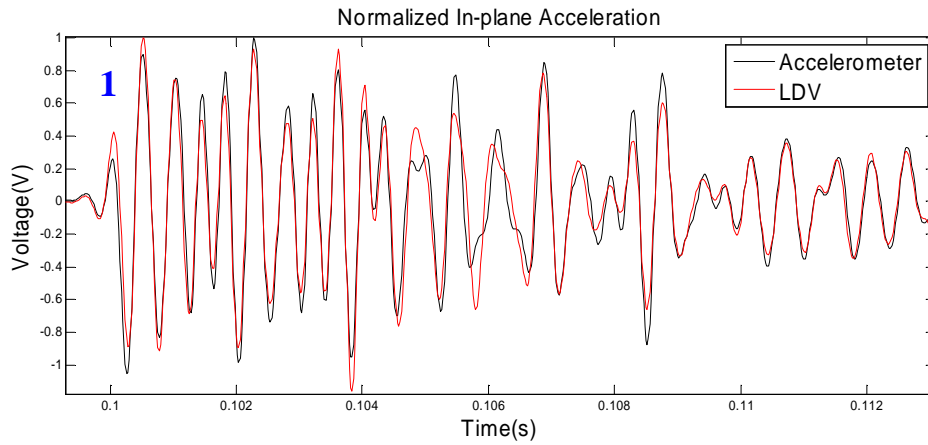
Figure 20: Zoomed comparison of the direct arrival and high amplitude portion of the time signals for the normalized in-plane acceleration collected with the LDV (red) and accelerometer (black).
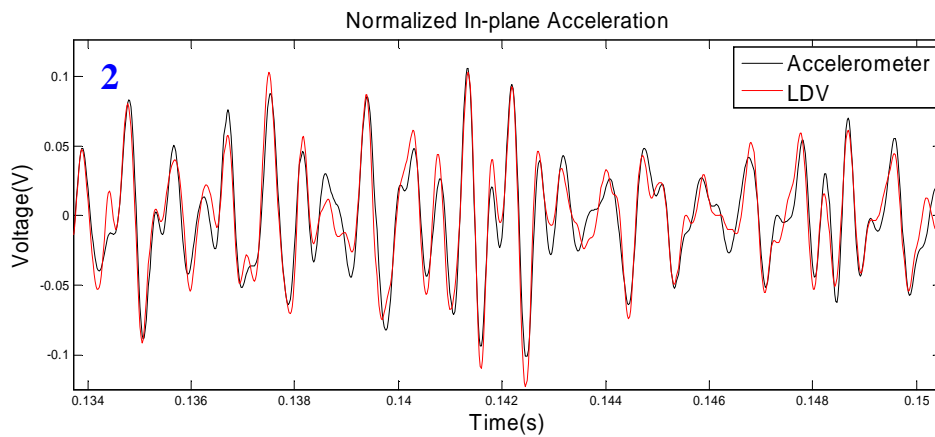
Figure 21: Zoomed comparison of the coda or low amplitude tail of the time signals for the normalized in-plane acceleration collected with the LDV (red) and accelerometer (black).

40

The frequency spectrums from both devices shown for each component in figures 22 and 23 also show very good agreement. The filter does not eliminate all of the contribution to the time signal above 2.5kHz so these plots show the entire content of the frequencies that make up the signals in the time domain.
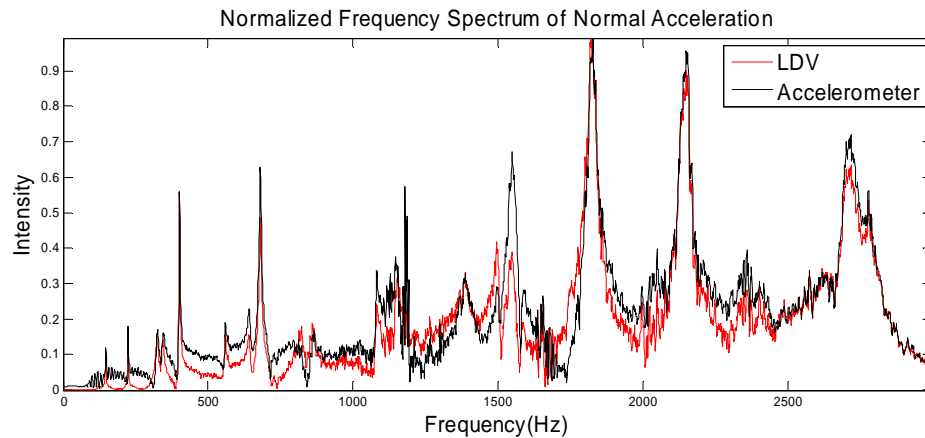
Figure 22: Comparison of normalized frequency spectra of normal acceleration collected with LDV (red) and accelerometer (black).
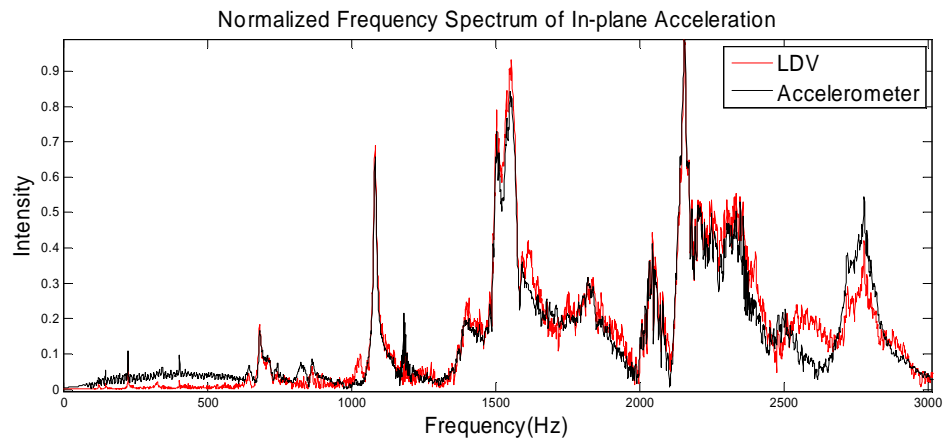
Figure 23: Comparison of normalized frequency spectra of in-plane acceleration collected with LDV (red) and accelerometer (black).

In both the time and frequency domain, the signals collected from both transducers show good agreement, and it even seems as if the in-plane components may show even better agreement for this particular angle and data set.

41

3.4.3 Quantitative Comparison: Oblique Angle Test

After performing the qualitative analysis by visually comparing the time signals and frequency spectrums, an additional step was taken to make this comparison more quantitative. All of the time signals for each of the oblique angles of incidence ($\theta = 45.25$ °, 60.87 °, 73.5 °, 80.82 °, 83.85 °) used for the outer LDVs seemed to show good correlation at the qualitative level, but it was still unclear which angle was the best or if that could be determined. The maximum values of the normalized cross-correlations between corresponding LDV and accelerometer signals were determined for each of the three data sets collected for each angle of oblique incidence of the LDVs, and these values are shown in figures 24 and 25 below.
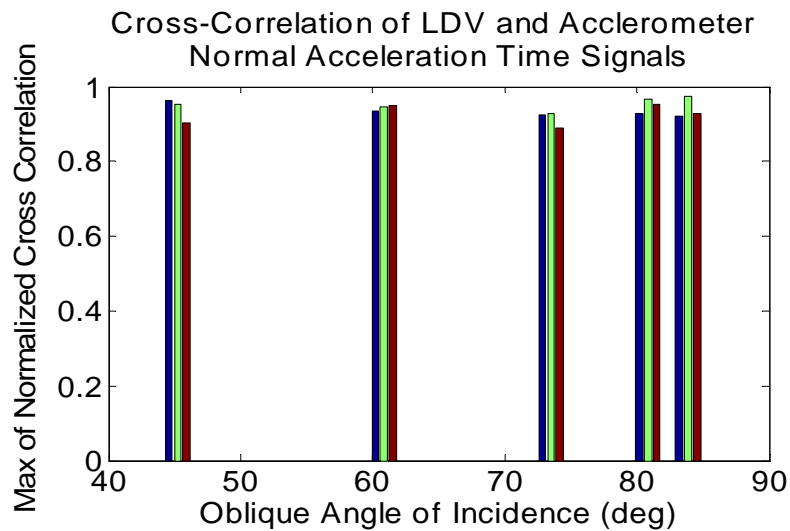
Figure 24: Maximum values of normalized cross-correlations of LDV and accelerometer normal acceleration time signals collected with varying angles of incidence; color distinctions represent the individual data sets collected at each angle
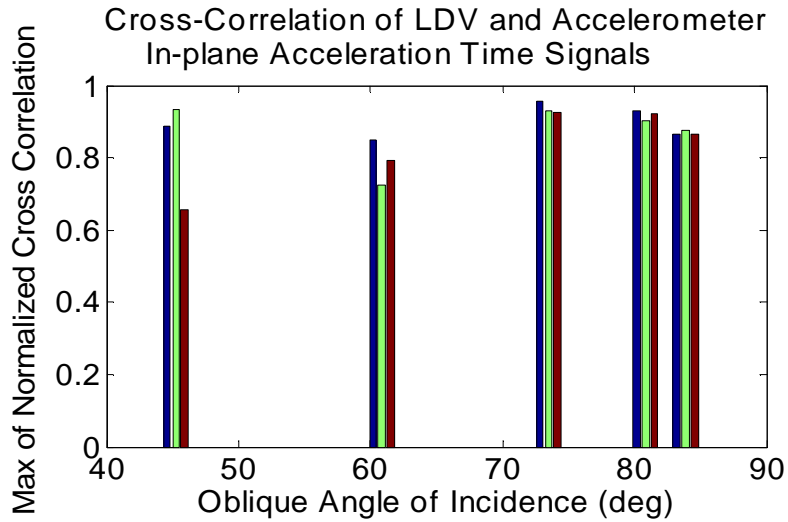
Figure 25: Maximum values of normalized cross-correlations of LDV and accelerometer in-plane acceleration time signals collected with varying oblique angles of incidence; color distinctions represent the individual data sets collected at each angle

It can be seen that the normal components showed very good correlation across the range of angles. This could be a bit deceiving because the normal LDV signal was not calculated but taken directly from the signal measured by the middle LDV, but figure 24 is included in order to show that there no major variation in the setup for each data set at each angle of incidence. This would imply that there should be similar, minimal variation in the in-plane component since it is assumed that nothing changed between data sets, but this is not necessarily the case.

The cross-correlation of the in-plane component is where the information regarding the best oblique angle of incidence would lie because the in-plane component is calculated using only the two signals collected using the outer LDVs and the measured angle θ. Two important pieces of information were gathered from figure 25. First, each of the LDV angles displays the ability to collect and decompose signals with good correlation to the accelerometer signals. It is interesting that LDV in-plane signals with high correlation to the accelerometer signals were able to be collected across a broad

range of incidence angles. There was some thought in the initial phases of the development of this system that there would be a significant tradeoff between the accuracy of the decomposed in-plane component of motion and the angle of incidence on the surface of interest due to the fact that a steeper incidence angle (smaller θ) results in more of the in-plane component being collected by each side LDV individually (Equ. 4 and 5). This tradeoff between incidence angle and accuracy makes some sense intuitively, but after the two signals from the side LDVs are combined and the full in-plane signal is decomposed, there is no tradeoff. This is shown in the geometry of section 3.2.1 and demonstrated here. It should be noted, however, that it is only true that there is no tradeoff in either direction if good SNR can be generated at all angles. If it cannot, there is the opposite tradeoff between incident angle and in-plane accuracy for steep angles. In this case, a steeper angle would actually result in lower SNR and an inaccurate decomposition of the in-plane component as a result. Based on the fact that good in-plane signals can be decomposed using large angles of incidence, improving SNR by bringing the side LDVs closer to normal (increasing θ) will improve the accuracy of the in-plane component without the tradeoff related to losing information due to the larger angle. Caution should be taken in increasing θ too much though because there is also a limit here as the alignment error blows up when θ gets close to 90 degrees.

The second thing of note from figure 25 is that the cross-correlations at the lower angles are not as consistent as the higher angles. One of the data sets collected at an angle of $\theta = 43.25$ ° has a very high correlation peak, but the correlation of one of the other data sets is significantly lower comparatively. The data collected with $\theta = 60.87$ ° shows a similar phenomenon but less pronounced. The source of this erratic behavior at the

smaller angles of incidence with respect to the plane of interest is difficult to say due to the small number of samples collected for this portion of the analysis. The LDVs displayed full intensity and seemingly good SNR during data collection due to the reflective tape that was used, so noise and measurement error can most likely be ruled out (assuming no anomalies in the data collection resulting in decreased accuracy due to malfunction of the LDVs). Based on the relationship between parameter error and $\tan\theta$, it would be difficult to presume that increased error around $\theta = 45°$ would be caused by inaccuracies in the measurement of θ. The most likely cause of this error seems to be adjustments made between data collections to attempt to adjust the focusing of the LDVs. Although adjustments to any part of the alignment between data collections with the same oblique incidence angle would normally be strictly prohibited in this type of study, this quantitative portion of the analysis was performed after the data had already been collected for the qualitative comparison. During data collection, the goal was to guarantee that the LDVs showed good intensity on their displays. At times, this resulted in adjustments to the focusing of the LDVs which could have led to accidental misalignment and necessary adjustments to realign the LDVs. Initially, the goal was simply to show that good signals could be collected at a wide range of angles and comparing data sets quantitatively was not the focus. Regardless, the oblique angle that produced the best results overall was $\theta = 73.5°$ with $\theta = 80.82°$ also performing very well. $\theta = 83.85°$ was consistent with all signals correlating well but not quite to the level of the two previously mentioned angles. This downward trend was possibly due to the parameter error being magnified as θ approached $90°$.

3.5 Conclusion

This chapter has detailed the experimental setup, procedure, and analysis used to validate that the developed system including the LDV configuration and hardware/software integration using the Labview VI explained in Chapter 2 does in fact measure both the normal and in-plane components of the motion of the surface of interest. In this experiment, a simple plate was used, and the analysis was performed at the lower end of the frequency range capabilities of the LDVs, but there was no indication that the multidimensional LDV system would breakdown within the range of the LDVs frequency capabilities (0-22kHz) or with more complex geometries provided the necessary measurements could be made accurately. The direct correlations between LDV and accelerometer signals were very good despite the complexities of the propagating Lamb modes within the plate and the basic differences between the two transducers. This shows that, as long as the experimental setup is precise with angles measured accurately, this LDV system is equally capable of collecting components of multiple dimensions as a PCB Triaxial Accelerometer with the added benefits of a less invasive, non-contact optical transducer.

This experiment also demonstrated that accurate measurements could be made across a broad range of incidence angles, θ, but that the most consistent and accurate measurements were made at an incidence angle of $\theta = 73.50°$. Angles between $70° < \theta < 75°$ were used for the remainder of the study, and applications using this system will attempt to operate in this range unless it is unfeasible to do so or it is shown that there is a truly optimal incidence angle for the outer LDVs. The surface of the target of interest is very important for the performance of the LDVs, so this incidence angle range may need

to be adjusted if optimal intensity levels cannot be reached within it. This is simply a suggested range based on a small sample of data, but the actual angle will always be contingent upon satisfactory levels of reflected light.

CHAPTER 4

MONITORING APPLIED STRESS VARIATIONS OF ALUMINUM SAMPLES USING 2D MEASUREMENTS OF MULTIPLY SCATTERED WAVES

4.1 Theory: The Acoustoelastic Effect

The acoustoelastic effect is the well-founded dependency of the wave speed on the level of stress and strain within a medium. The strain effect on wave velocity is an order of magnitude smaller than the stress effect and can be ignored. [Larose 2009] Typically, this phenomenon is studied by taking time-of-flight measurements using known source and receiver locations to measure wave speed directly in order to detect changes in stress. The wave velocity in a sample under uniaxial stress, $\Delta\sigma$, can be described to the first order as

$$V_{ij} = V_{ij}^0 + \frac{\partial V_{ij}}{\partial \sigma}\Delta\sigma + o(\varepsilon) \tag{14}$$

where i and j represent the directions of propagation and particle motion respectively. The dimensionless non-linear parameter β is defined as:

$$\beta_{ij} = -\frac{E}{V_{ij}^0}\frac{\partial V_{ij}}{\partial \sigma}. \tag{15}$$

where E is Young's modulus, and it depends on the second (Lamé) and third (Murnaghan) order elastic constants. Hence overall, the relative change of the wave velocity is expected to vary linearly with the stress increment $\Delta\sigma$

$$\frac{\Delta V_{ij}}{V_{ij}^0} = K\Delta\sigma \tag{16}$$

where K is the proportionality constant which depends on β. [Stobbe 2005] This formalism of the acoustoelastic effect will be used for the remainder of this chapter in order to properly describe the analysis of the collected components of motion in both the time and frequency domains.

Since the acoustoelastic effect is treated as a first order perturbation, its net effect on the measured waveform can be thought of as a simple stretch or compression of a signal in time. More precisely, if $h^k(t)$ is a time signal collected with load k, and $h^0(t)$ represents the waveform under no stress, then the acoustoelastic effect can be described using

$$h^k(t) = h^0(t(1-\nu_k)) \tag{17}$$

where the companding parameter $\nu_k \ll 1$ depends on the relative velocity change

$\dfrac{dV}{V} \ll 1$, and the negative sign is used to denote compressive stress. When the Fourier transform is used to convert this time signal to the frequency domain

$$h^k(\alpha_k t) \rightarrow H^k(f/\alpha_k), \tag{18}$$

since $\nu \ll 1$, $\frac{1}{\alpha} = \frac{1}{1-\nu} \cong 1 + \nu$, so that the frequency spectrum under load k can be expressed as

$$\hat{H}^k(f) = \hat{H}^0(f(1+\nu_k)). \tag{19}$$

Hence, in a broadband signal, the acoustoelastic effect can be seen not only in stretching or compression of the time signal but also in shifts in the frequency spectrum under varying loads.

4.2 Polarization Study

Furthermore, recent developments suggest that, for certain hard materials, polarization may actually be up to an order of magnitude more sensitive to stress loading than wave speed. [Junge et al. 2004; Junge et al. 2006] Polarization can be defined in several ways, but in general, it is a measure of the relationship between the normal and in-plane components of the surface motion caused by a propagating wave in an object. When plotting normal displacement on the y-axis and in-plane displacement on the x-axis, polarization can be used to visually describe the actual motion of a point on the surface of an object. In the special case of a Rayleigh surface wave, this particle motion on the surface is elliptical with the major axis in the vertical direction. Changes in stress cause this polarization ellipse to expand or compress along the major axis (and compress or expand, respectively, along the minor axis) depending on the compressive or tensile nature of the loads. [Junge et al. 2004; Junge et al. 2006]

The difficulty with this analysis is two fold. First, generating pure Rayleigh waves require a high frequency setup (or a very thick sample), and second, measuring both the in-plane and normal components of motion accurately is a challenge. This thesis focused on the latter, and with the developed system, a study was done to determine what information could be extracted from the 2D vibration measurements as they apply to the acoustoelastic effect in an Aluminum plate. Elastic waves were generated in the thin plate under various levels of stress, and the signals were analyzed in an effort to determine what effect the stress in the plate had on the propagating waves. Due to limitations of the experimental setup including the low frequency range of the system and the size of the plate that was used as a target, the waves created by the point source were Lamb body

waves instead of much simpler Rayleigh surface waves typically used in ultrasonics applications. Because the wavelengths of low frequency elastic waves are long with respect to the thickness of the aluminum plate (.131"), they can easily "see" and interact with both sides of the plate, causing the generation of both symmetric and antisymmetric Lamb modes. [Achenbach 1999; Graff 1991] Fortunately, the plate is thin enough and the frequency low enough so that only the zero-order modes (A_0 and S_0) were likely to be propagating. The measured waveforms, however, were complex due to multiple scattering effects at the plate edges.

4.3 Experimental Setup

This experiment used the system developed and validated in Chapters 2 and 3 with two notable changes in the setup. First, the object of interest was a 6" x 3.375" x 0.131" Aluminum plate, and second, a stress fixture was introduced in order to take measurements with the plate under stress. This plate was much smaller than the one used in Chapter 3 and was chosen for its thickness and width. In the frequency range of interest, this plate was thin enough to guarantee excitation of only the zero-order Lamb modes. The smaller size was also needed due to the diminutive size of the stress fixture. The fixture used was a Mark-10 Force Measurement Test Stand Model TSC. It was a manual fixture with both pressure and strain gauges and was used to apply uniaxial compressive loads to the plate. When oriented according to its design, stress is applied along the vertical axis with respect to the surface upon which it is placed, so in order to take measurements of the in-plane component of motion parallel to this stress axis, the fixture was laid on its side and leveled as shown in figure 26.
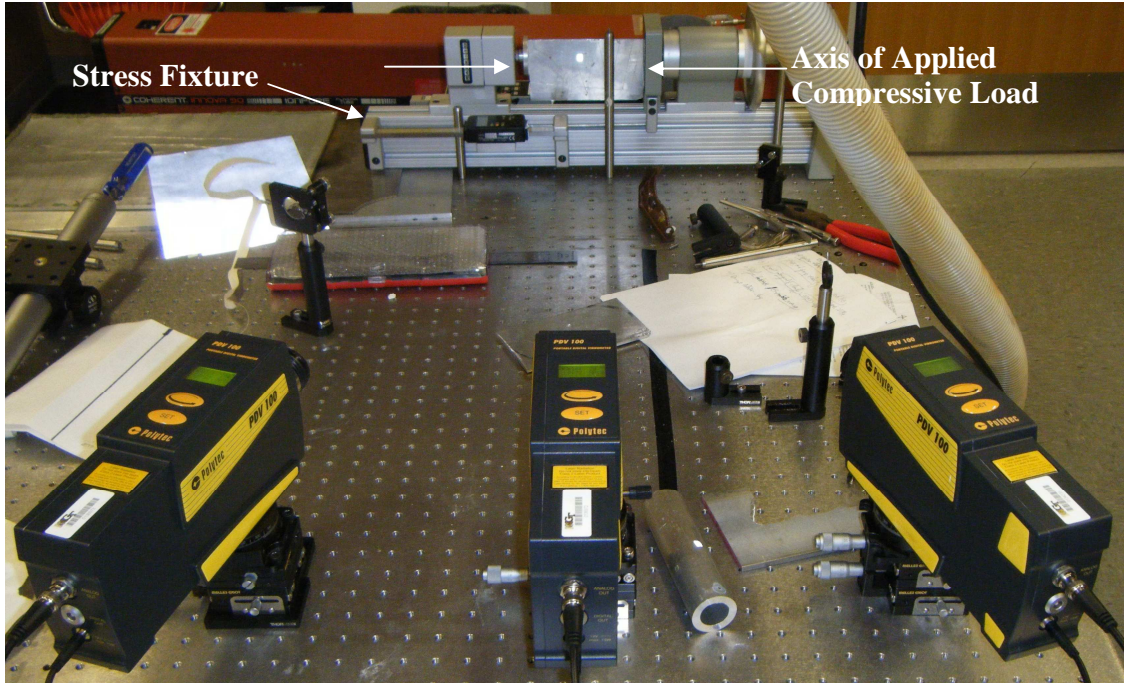
Figure 26: 2D measurement configuration using 3 Polytec PDV-100 LDVs mounted on the optical table and focused on an Aluminum plate under stress.

Two different ranges of loads (100lb-115lb, 200lb-235lb) were applied to the plate and data was collected at varying load step increments. For range 1 (100lb-115lb), all signals were collected at load increments of 3lbs, and for range 2 (200lb-235lb), signals were collected at increments of 5lbs up to 215lbs and 10lbs up to 235lbs. Fifty signals were averaged for each collection. Each collection took approximately two minutes, and small amount of creep was detected in the fixture, but it was negligible compared to the accuracy of the load measurement which was approximately ±1lb.

4.4 Data Processing

The signal processing techniques used to analyze the Lamb wave data can be divided into two categories—single component and component relationship techniques.

4.4.1 Single Component Analysis

Single component signal analysis for this experiment focused on the normal and

in-plane components of motion separately. Basically, in an attempt to simplify things, time signals and frequency spectra were compared across load range for an individual component at a time.

All data was preprocessed as described in Chapter 3 by filtering it from 6kHz-22kHz, and the normal and in-plane components were extracted from the raw data. Then, the time signals and frequency spectra were plotted across load ranges in order to provide some preliminary perspective on what was occurring with respect to the compression and shifting of the time signals and frequency spectra respectively.

The remainder of the single component analysis focused on the frequency spectra and how the applied loads caused noticeable shifting of the resonance peaks. These narrow frequency bands where the signals contained peaks of strong intensity were identified. Then, the exact frequency where the maximum occurs under each load condition was identified, and plots were generated of frequency shift relative to the resonance frequency of the smallest load

$$\Delta f = \frac{f^k - f^1}{f^1} \tag{20}$$

where, f^k is the frequency value at a resonance peak of the frequency spectrum for load k, and f^1 is the frequency at the same resonance peak under the lowest load. Δf is analogous to the shift parameter ν that was discussed in the theory of the acoustoelastic effect. This load dependent value was plotted on the y-axis with the independent load values represented on the x-axis in the form of the change in load relative to the lowest load or

$$\Delta S = \frac{S^k - S^1}{S^1} \tag{21}$$

where, S^k is the load in question, and S^1 is the lowest load in the range being analyzed. Identifying the peaks caused by the same Lamb modes within a single range was fairly straight forward because they were very close together and of similar amplitude, but the resonance peaks for a single mode across both load ranges was much more difficult due to the large gap in the frequency domain between the groups of resonances. The plots of $\Delta f(\nu)$ vs. ΔS revealed a linear relationship between the two parameters, so linear fits were performed on all of the plots in order to determine the sensitivity of relative frequency shift Δf to relative shift in load level ΔS.

4.4.2 Multi-Component Vibration: Joint Analysis

After the data for each of the components was analyzed individually, attempts were made to gather more information from studying how the two vibration components related to each other.

4.4.2.1 Time window selection

In order to do this, the time domain data was first windowed in an arbitrary time window of the whole broadband reverberant waveform. Early time-window corresponds to the direct arrival and first reflections. Late time-window corresponds to multiply scattered waves at the plate boundaries. The later portion of the time signal is called the coda, and traditionally, analysis is focused primarily on this portion because it is there that the broadband signal contains information about many reflections of the initial wave. These reflections serve to allow many interactions between the wave and the object and the objects condition(s) (i.e. cracks, stresses, material heterogeneities, etc.). The more times the wave encounters the condition of interest, the more the signal becomes altered as can be seen in this case with increasing application of stress.

The width of the time window was determined by the achievable temporal resolution which is inversely proportional to the selected frequency bandwidth. Since the selected broadband frequency bandwidth was 17kHz, the resolution of the filtered signal was limited to .059ms. With this as the lower bound of the possibilities for the width of the time window, an arbitrary width of 3.3ms was selected, and the remainder of the signal was set to zero. Then, the window was smoothed slightly by multiplying it by the Hanning function, and a fast Fourier transform was applied to convert it to the frequency domain. The resulting window of smoothed time data and its frequency content were the basis for the remainder of the signal processing and analysis.

4.4.2.2 Polarization angle measurement in the frequency domain

The primary focus of this portion of the signal processing was on how polarization was affected by changes in stress. Due to the complexities caused by the presence of Lamb waves, polarization in this situation refers to the phase angle between the signals representing the normal and in-plane components of motion. This was actually calculated using the ratio of the frequency spectra rather than the time signals. Therefore, polarization was defined as

$$\Pi = angle\left(\frac{\hat{u}_x}{\hat{u}_z}\right) \tag{22}$$

where, *angle* is the MATLAB command for determining the phase angle in radians of the complex matrix defined by $\frac{\hat{u}_x}{\hat{u}_z}$. Defining polarization in this way allowed analysis to be performed across the entire frequency band of interest. Plots were made of Π vs. frequency for all loads within a load range and were placed on top of all of the frequency

55

spectra for both components of motion across load range. The analysis was more qualitative in nature. Much like the shifts in frequency spectra, the polarization curves remained very similar when the applied load increased, but they were shifted. These shifts were not constant across frequency, but were much more pronounced in certain narrow frequency bands. In these bands, the polarization curves showed significant separation and were in order with respect to load level. Attempts were made to identify these areas in order understand this phenomenon further. It was also important to determine the resolution of our system as it pertains to this type of polarization measurement.

4.4.2.3 Particle motion measurement in the time domain

Finally, the two components of motion were analyzed in conjunction with one another through a direct comparison of the normal and in-plane components in the time domain of the windowed data in an attempt to apply a modified version of the elliptical analysis used in Rayleigh wave analysis to these Lamb wave excitations. Unlike the previous analysis that was done in the broadband frequency domain, this is a narrowband analysis. Dispersion of the Lamb waves prevents this analysis from being applied as directly as the simplified Rayleigh wave case. For this low frequency application, the windowed data first had to be filtered over smaller frequency bands contained in the broader bandwidth used for the previous analysis. The zeros were used to improve the resolution during the filtering but were dropped before proceeding. Then, in order to improve the resolution of the ellipse, the signals were interpolated using a cubic spline function. Finally, the windowed, filtered, interpolated time signals were plotted with the normal along the y-axis and the in-plane along the x-axis.

4.5 Experimental Results

4.5.1 Single Component Analysis

When the relative frequency shift, $\nu = \Delta f$, is plotted versus relative change in applied stress, ΔS , the data is fit most accurately by a linear fit as expected from the theoretical predictions from Section 4.1. Figures 27-29 below show the frequency shift in the normal component with increasing load across both load ranges individually and then together. At this resonance in the data, the peaks of the amplitude spectra (or resonance peaks) are very well separated and they have good intensity. This linearity across both ranges leads to the determination that all of the resonances identified between 9000Hz-9425Hz were caused by the same mode of vibration. Other attempts were made to analyze data across load ranges with little or no success. In many instances, there was linearity in each range independently but with noticeably different slopes implying that the resonance peaks that may have been close together in the frequency spectrum were actually caused by different modes of the Lamb wave.

Figure 27: Relative Frequency Shift vs. Relative Change in Applied Load for the normal component over load range 1 (100lb-115lb) for the resonance peaks near 9kHz; blue: data, red: linear fit defined by the equation upper left

Figure 28: Relative Frequency Shift vs. Relative Change in Applied Load for the normal component over load range 2 (200lb-235lb) for the resonance peaks near 9kHz; blue: data, red: linear fit defined by the equation upper left
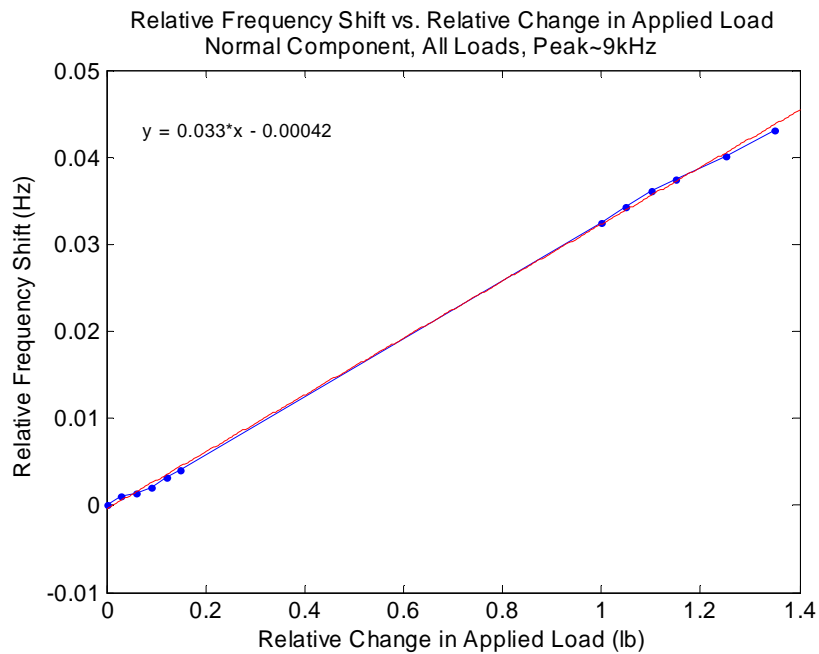
Figure 29: Relative Frequency Shift vs. Relative Change in Applied Load for the normal component over both load ranges for the resonance peaks near 9kHz; blue: data, red: linear fit defined by the equation upper left

The slope of these plots is a measure of the sensitivity of the frequency shift to increasing applied load. A steeper slope implies a greater sensitivity of the frequency shift to load change, and it is believed that the modes with the greatest sensitivity are those that travel along a path nearly parallel to the stress axis. Any mode that traverses the plate perpendicular or diagonal to the stress axis will be less affected by the presence of stress and will, therefore, not be as sensitive to changes in applied load. It was interesting to note how the slopes of the plots for the different frequency peaks varied and how they varied depending on the component that was being analyzed. The following plots (fig. 30-32) show three different resonance peaks of the in-plane frequency spectrum, and how they shifted with changes in applied load.
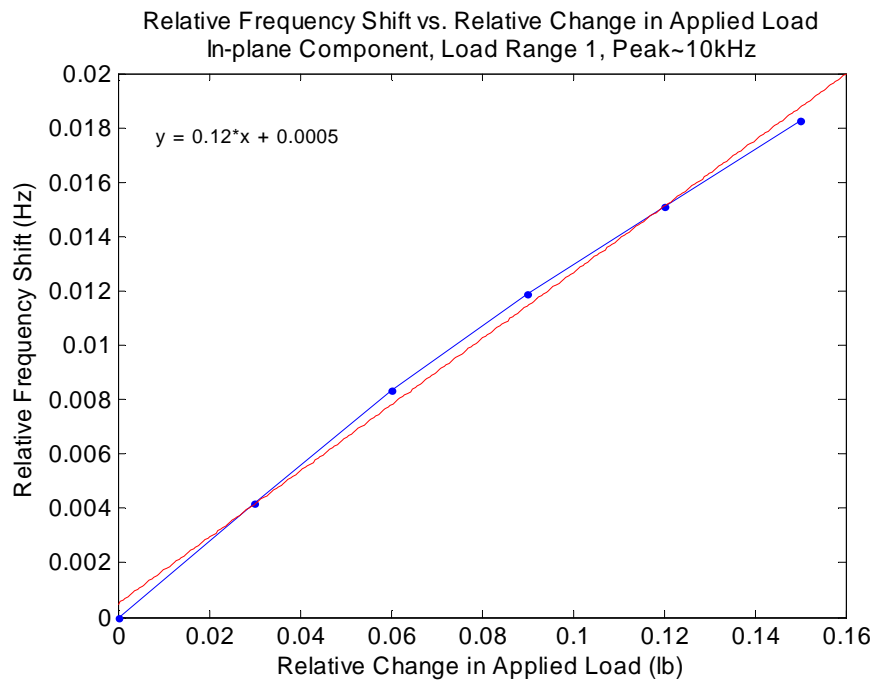
Figure 30: Relative Frequency Shift vs. Relative Change in Applied Load for the in-plane component over load range 1 (100lb-115lb) for the resonance peaks near 10kHz; blue: data, red: linear fit defined by the equation upper left

59
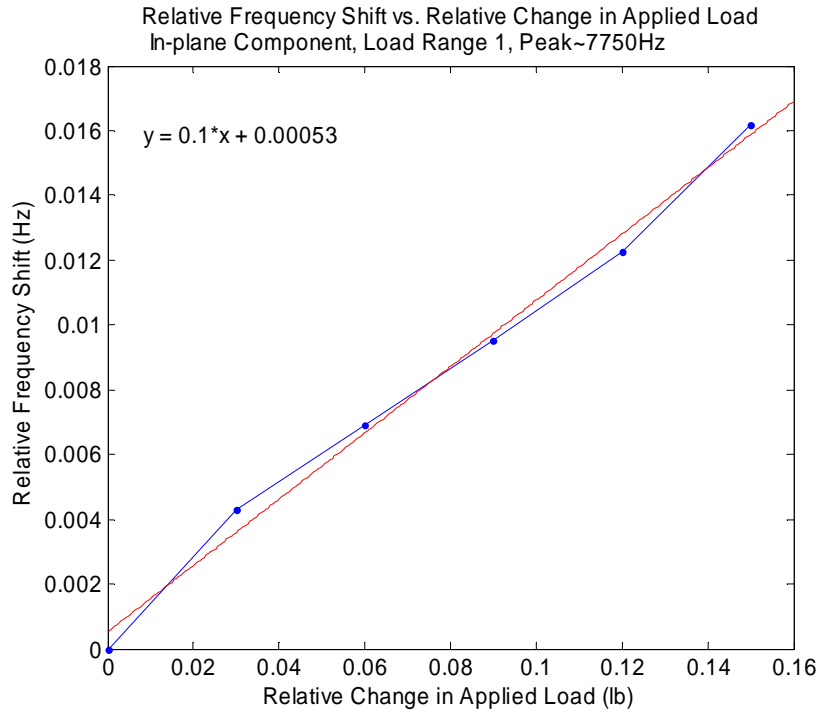
Figure 31: Relative Frequency Shift vs. Relative Change in Applied Load for the in-plane component over load range 1 (100lb-115lb) for the resonance peaks near 7750Hz; blue: data, red: linear fit defined by the equation upper left
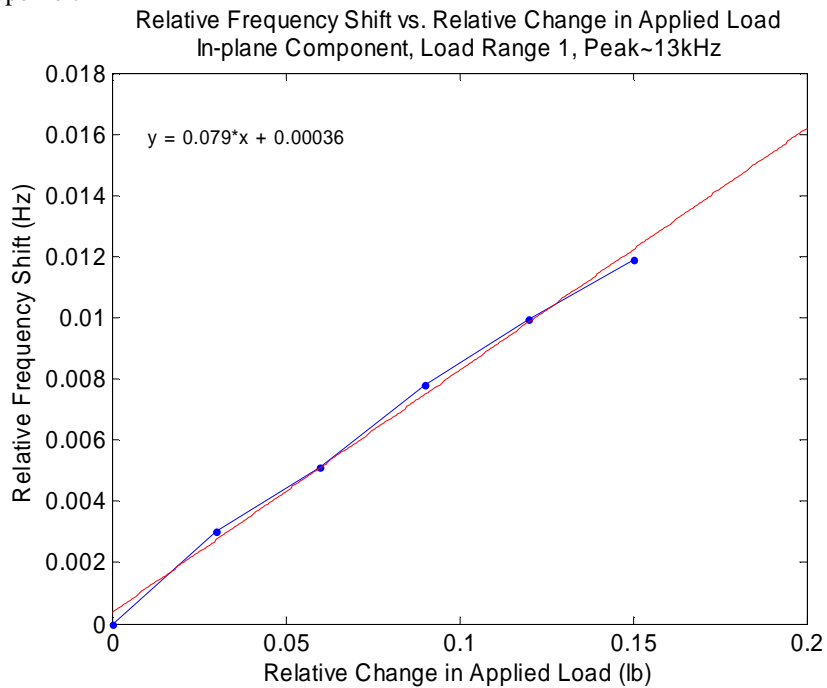
Figure 32: Relative Frequency Shift vs. Relative Change in Applied Load for the in-plane component over load range 1 (100lb-115lb) for the resonance peaks near 13kHz; blue: data, red: linear fit defined by the equation upper left

60

The linearity in each of these plots is as good as or better than any of the normal component plots, and their slopes are each significantly greater than the slopes of the previous plots or of any of the normal component plots as shown in Table 2.

Table 2: Comparison of the sensitivity (slope of linear fit) of the normal and in-plane components for different resonance peak ranges

Resonance frequency range (Hz)	Load Range	Normal	In-plane	Slope (Sensitivity)
9000-9060	1	x		.027
9300-9425	2	x		.029
9000-9425	both	x		.033
9800-10100	1		x	.12
7625-7800	1		x	.10
12900-13200	1		x	.079

While this application just a single situation with limited data, this seems to imply that the in-plane component could potentially be more sensitive to changes in stress levels than the normal component for certain situations. It also shows that even with complex Lamb wave signals, the in-plane component can be as precise as or more precise than the normal component in quantifying ν.

Another observation that was made when analyzing all the frequency spectra was that there seemed to be a peak near 16kHz in both the normal and in-plane spectra for all loads. It appears that the same mode analyzed in load range 1 has a resonance peak in both components of motion. While the effect of stress on ν is low for this mode, the slope is not only the same order of magnitude, but there is only 4.2% difference in the measured values of the slope for load range 1 which leads to the conclusion that one of the Lamb modes does in fact have a resonance in both components of vibration. The in-plane component for load range 2 is also fairly linear, but the slope is much steeper

61

leading to the realization that the peaks for this load range that were grouped together

with those from load range 1 are not artifacts of the same mode at all. Figures 33-35 show

this data and subsequent linear fits.
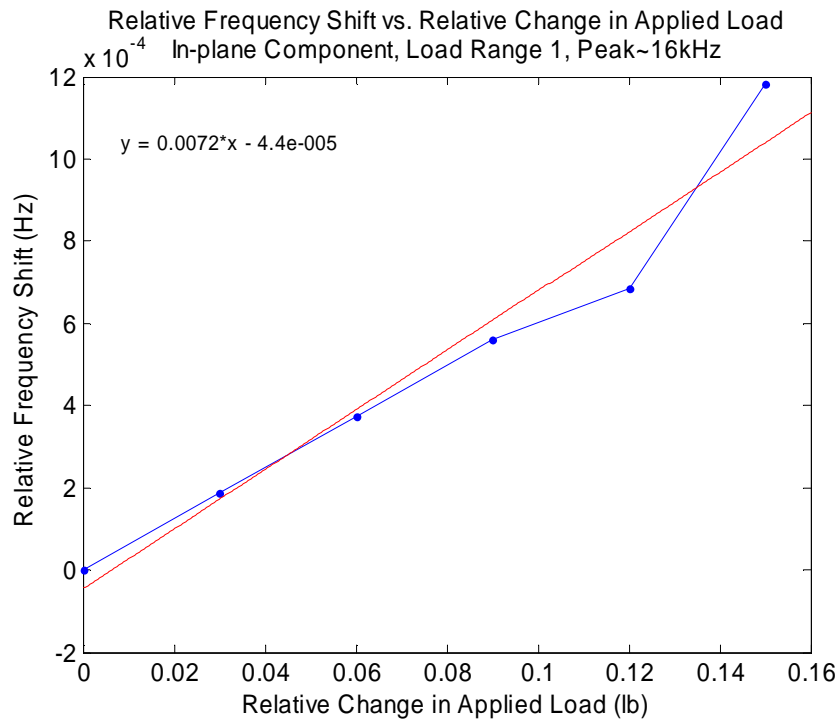
Figure 33: Relative Frequency Shift vs. Relative Change in Applied Load for the in-plane component over load range 1 (100lb-115lb) for the resonance peaks near 16kHz; blue: data, red: linear fit defined by the equation upper left
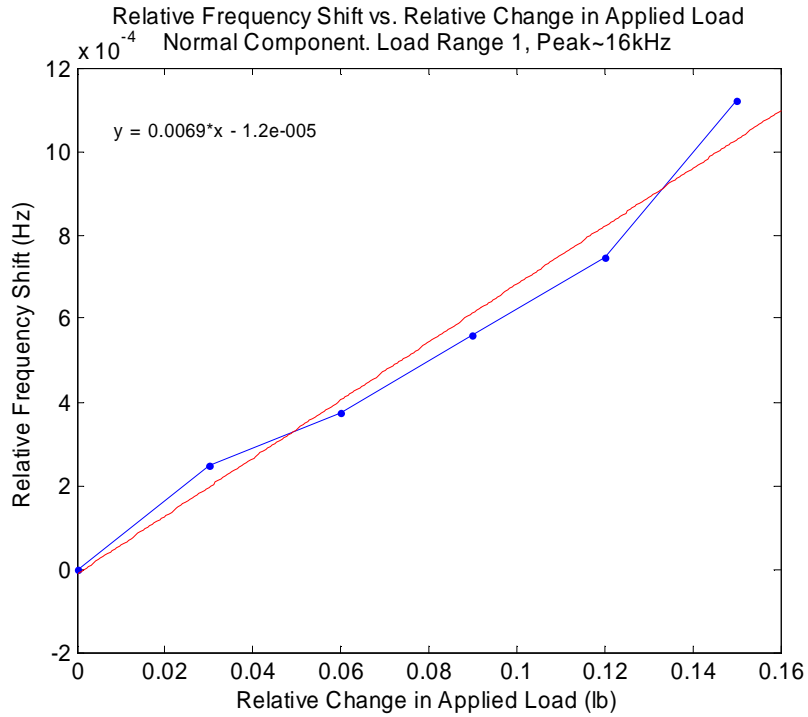
Figure 34: Relative Frequency Shift vs. Relative Change in Applied Load for the normal component over load range 1 (100lb-115lb) for the resonance peaks near 16kHz; blue: data, red: linear fit defined by the equation upper left
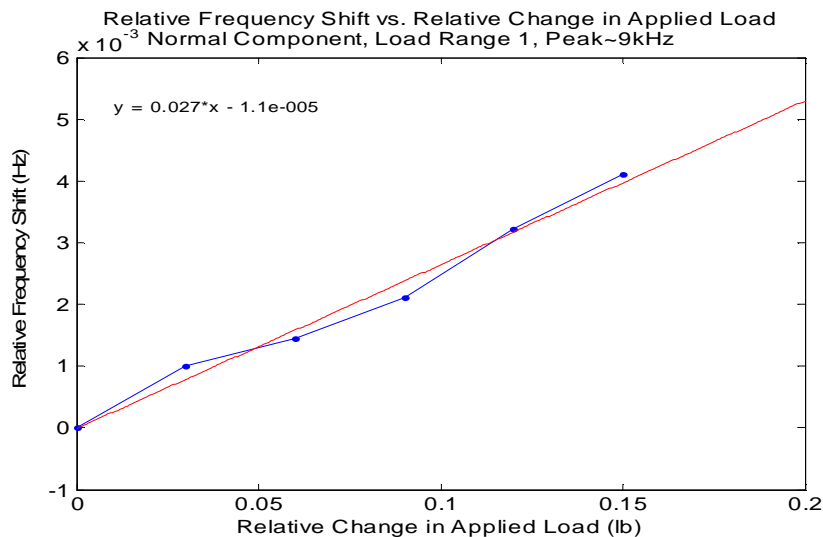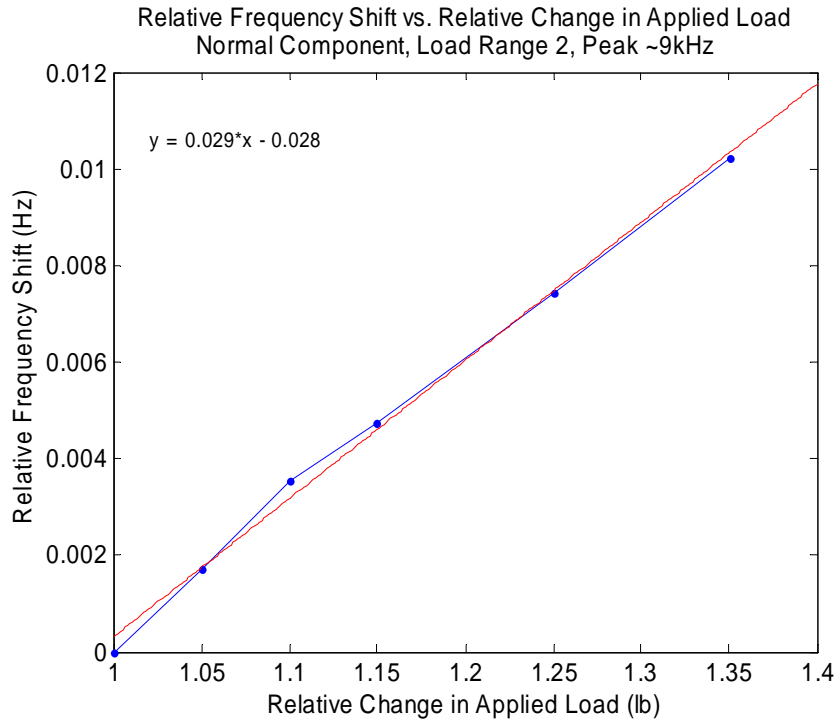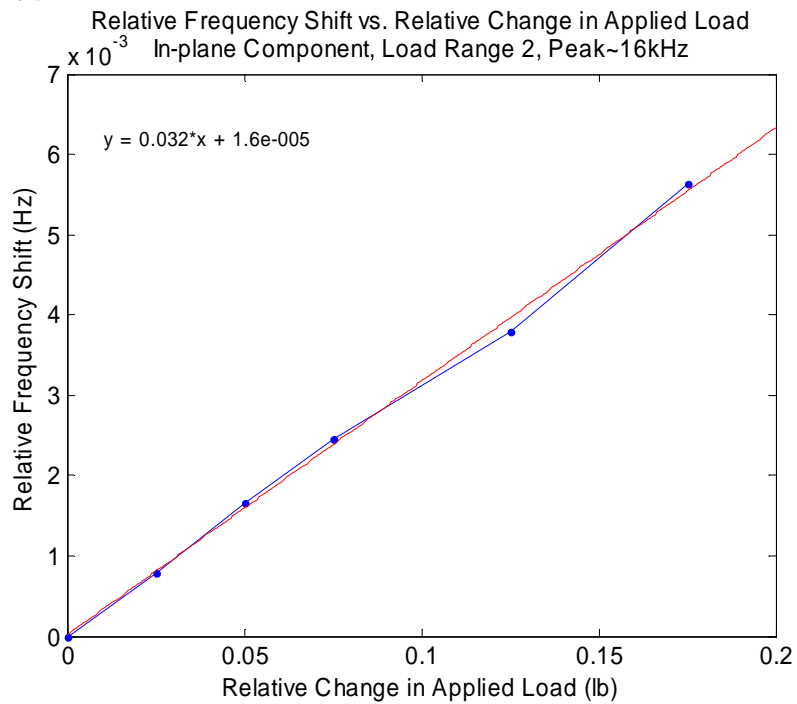

Figure 35: Relative Frequency Shift vs. Relative Change in Applied Load for the in-plane component over load range 2 (200lb-235lb) for the resonance peaks near 16kHz; blue: data, red: linear fit defined by the equation upper left

4.5.2 Multi-Component Joint Analysis Polarization angle and particle motion

When the polarization angle curves for each load level in load range 1 were plotted versus frequency on top of the frequency spectra for both components of vibration, it was clear that ideas from the resonance analysis conducted in the single component analysis could be applied to the polarization curves as well. As figures 36-39 below illustrate, the portions of the polarization curve that demonstrate both the correct shift direction for each load (resulting in proper ordering of curves) as well as the greatest resolution (separation in curves for varying loads) were those areas of the polarization curve that fell in the frequency bands where the resonance peaks of the amplitude spectra show the most linearity and sensitivity in ν. It seems that the ordering of the curves is related to linearity of ν, and the resolution between curves is related to the sensitivity of ν. This analysis was also done for another arbitrary time window later in the time signal, and the results were very similar.
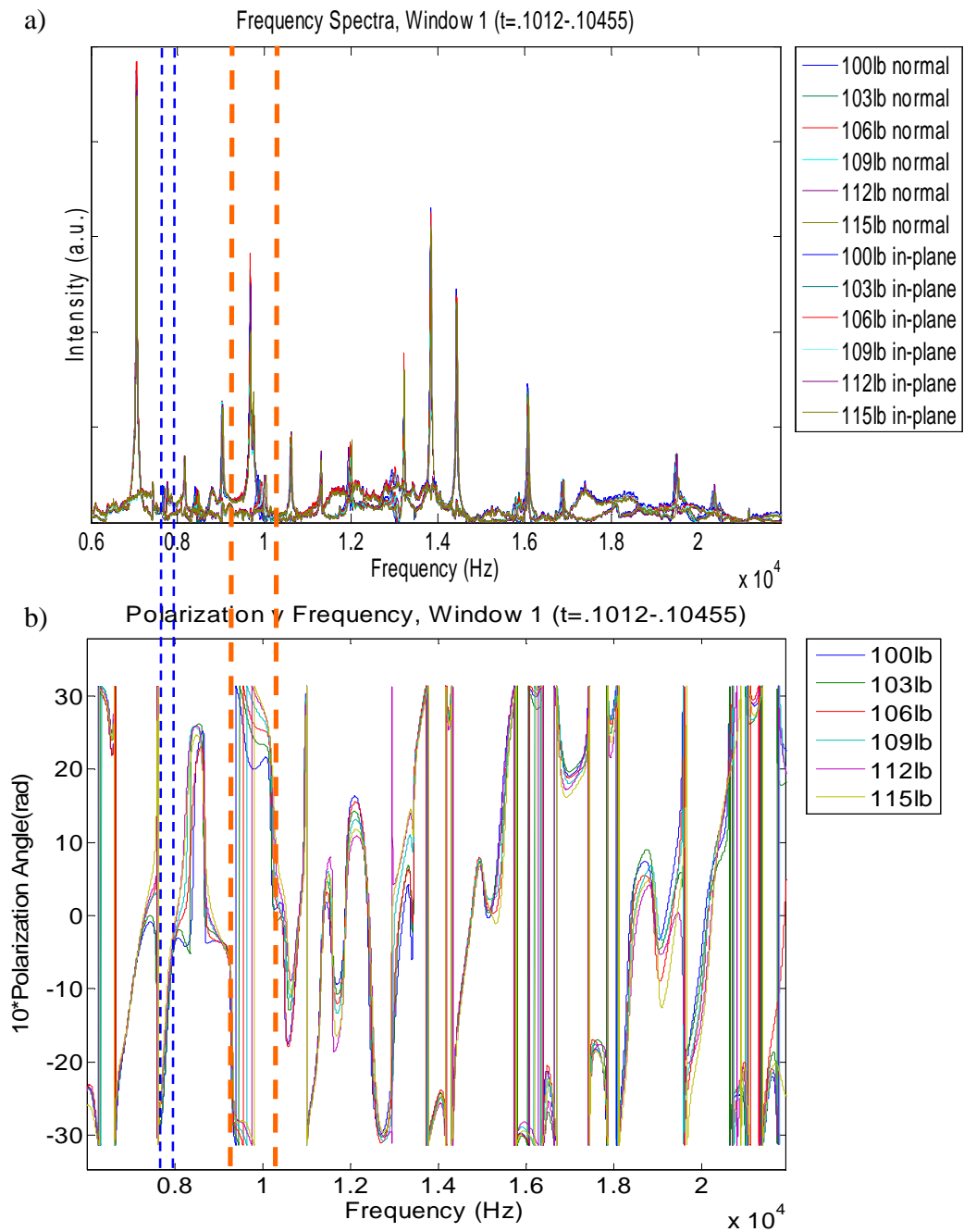
Figure 36: a) Frequency spectra for both components and range 1 load levels, **b)** Polarization angle plotted vs. frequency. Note that the orange and blue dashed lines denote areas that are zoomed for further analysis in the following figures.
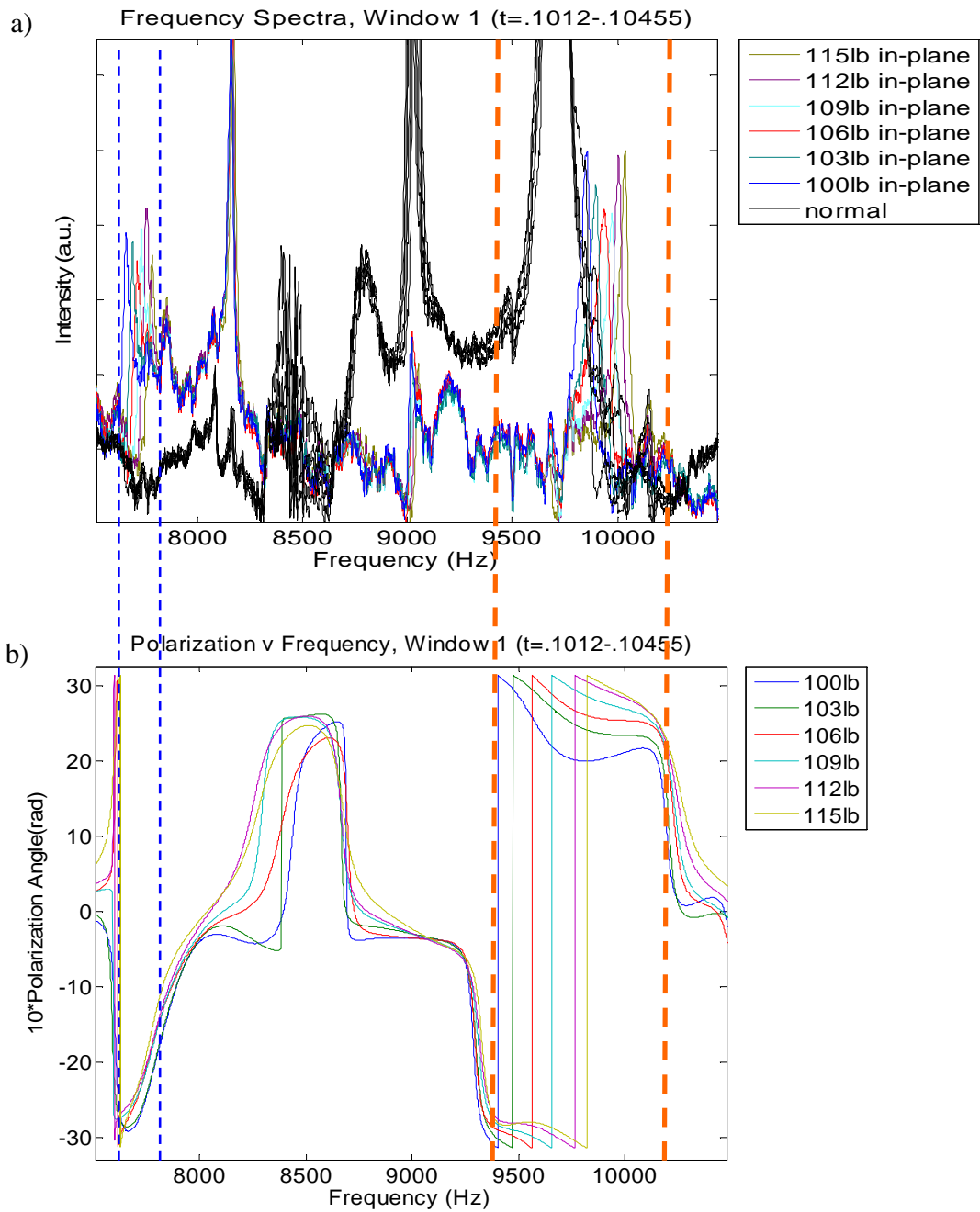
Figure 37: a) Frequency spectra for both components of range 1 loading; In-plane components are color coded according to load level, and all normal components are black. **b)** Polarization v. Frequency Plot. Zoomed area of interest to show how accuracy in the plots of polarization angle vs. frequency is related to good separation in the resonance peaks of the frequency spectra.
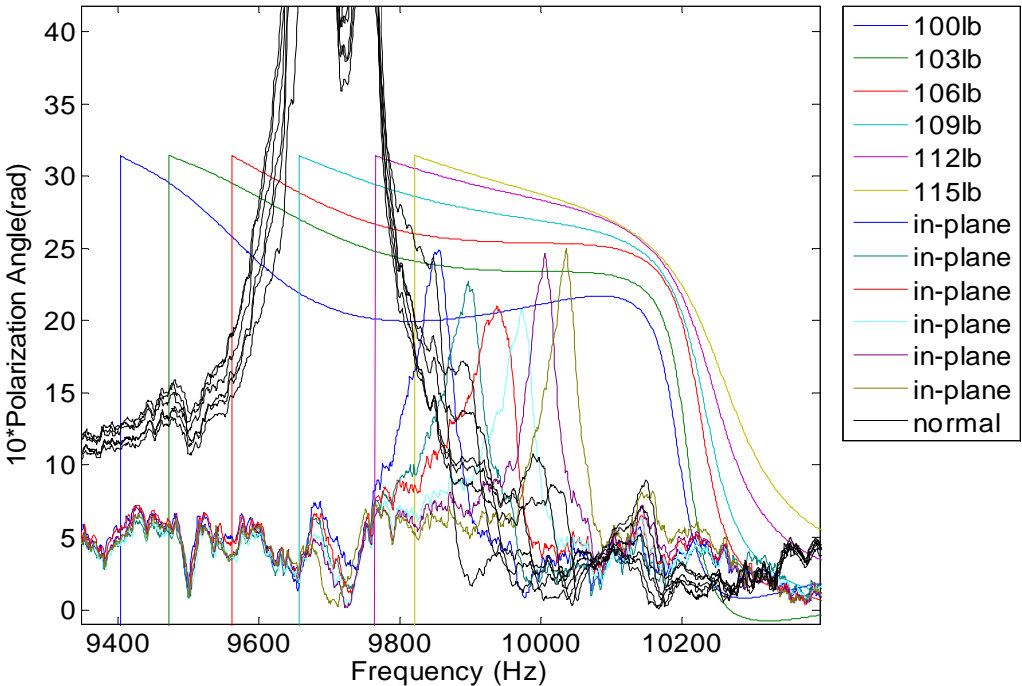
Figure 38: Zoomed area designated in previous figures by ORANGE dashed lines illustrating good accuracy (proper order) and resolution (good separation) in the plots of polarization angle vs. frequency for loads in range 1.
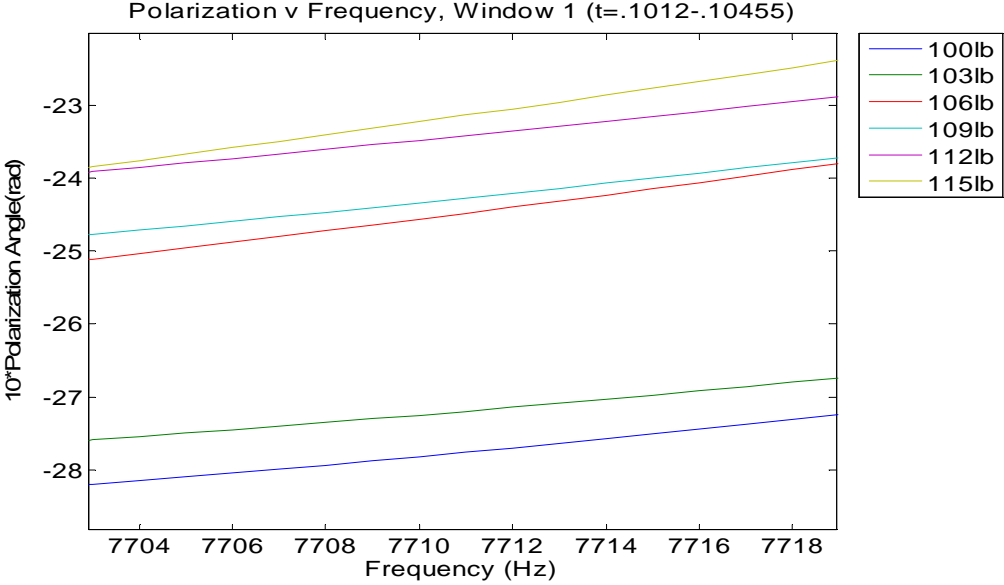
Figure 39: Zoomed area designated in previous figures by BLUE dashed lines illustrating good accuracy (proper order) and resolution (good separation) in the plots of polarization angle vs. frequency for loads in range 1.

After identifying these areas of good resolution and accuracy in the polarization

curves, the elliptical analysis was carried out as described in section 4.3.2 for the area

between 9.9kHz-10kHz. The following plots show how the polarization ellipses change

with increasing load for two different portions of the signal.
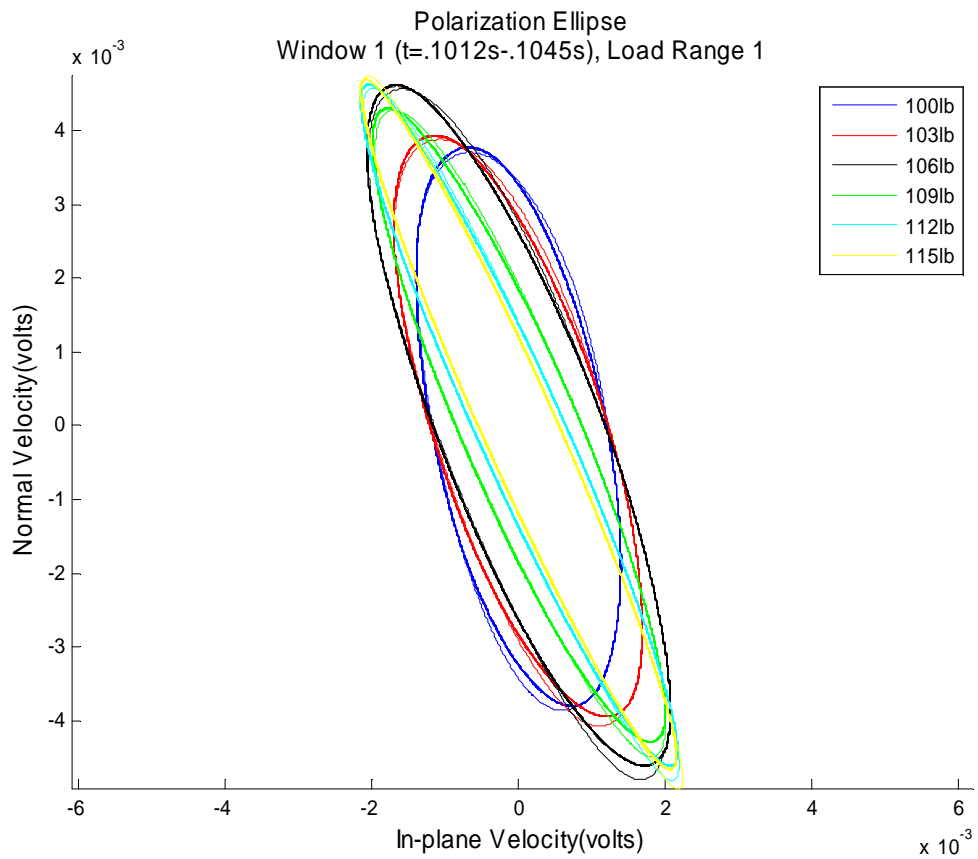
Figure 40: Polarization ellipse for time window 1 (t=.1012s-.1045s) which contains the direct arrival as well as the high amplitude portion of the time signal. This ellipse was created by filtering the data between 9980Hz-9990Hz.
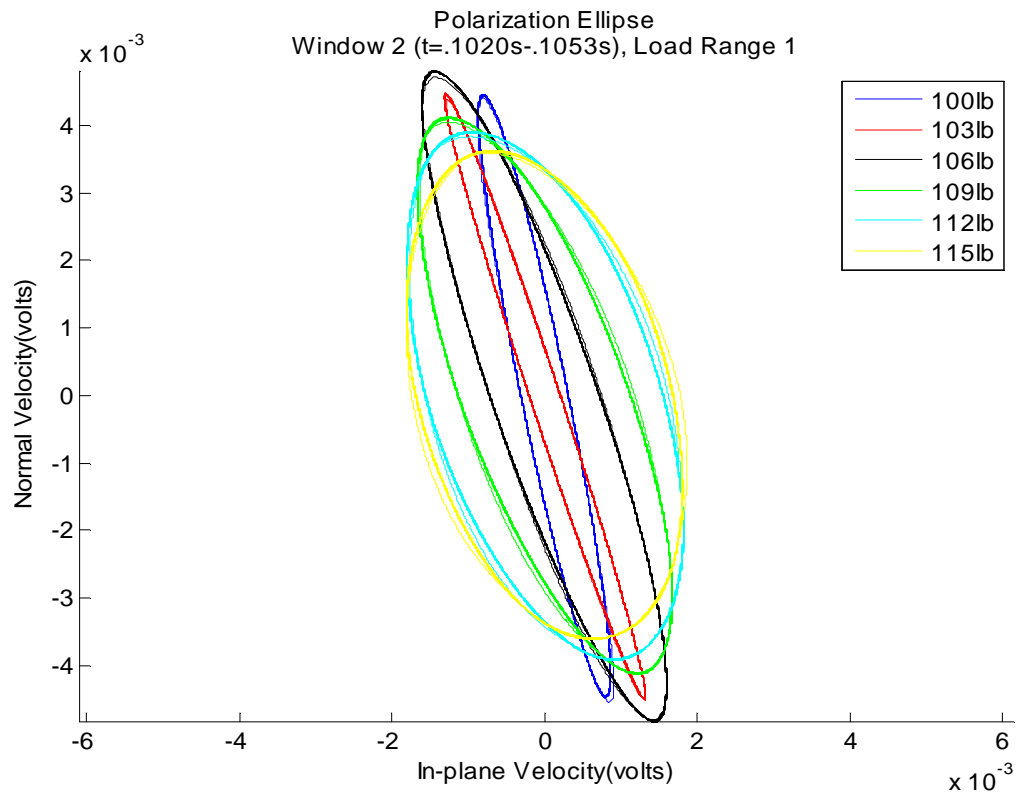
Figure 41: Polarization ellipse for time window 2 (t=.1020s-.1053s) which does not contain the direct arrival but instead many reflections of the Lamb waves within the plate. This ellipse was created by filtering the data between 9990Hz-10kHz.

As discussed previously in Section 4.2, ratio of the major axis to the minor axis of the particle motion ellipse changes under compressive stress, and that phenomenon can be seen in both of these plots as well. In general, as the applied compressive load increases, the ellipse expands in the normal direction and compresses in the in-plane direction. This is more pronounced in Figure 40 where "Window 1" was used. "Window 1" contains the direct arrival and fewer reflections from the boundaries of the plate. Because of this, this waveform in this portion of the signal is simpler allowing this type of analysis to produce promising results. In both plots, however, the stretch in the limits of the in-plane component can be clearly seen as the load increases. The complex Lamb

waves cause these ellipses to exhibit a tilt of the major axis, and it appears that this tilt increases with increasing load.

The ellipses for "Window 1" seem to align more directly with the theory developed for the acoustoelastic effect, and this is probably attributable to the simpler waveform for this portion of the reverberation signal. The coda contains more information in the broadband as mentioned previously, but complexity is introduced with added information; and for this narrowband analysis, the early portion of the signal may actually be more accurate as it appears here. Both windows of the time signal show increasing tilt (measured from the vertical) with increasing applied load, so this analysis shows promise to obtain useful information. However, due to the small amount of data and the qualitative nature of the analysis, further investigation is need to understand this phenomenon. Both of the techniques used to perform multi-component joint analysis are very qualitative in nature to this point, and steps must be taken in the future to determine quantitative relationships from these techniques. Measurement of the shifts in the polarization angle plots as well as quantification of the tilt and axis ratio of the ellipses under various loads may provide more information linking this multi-component analysis to the previous single component analysis. Also, it cannot yet be determined which portion of the signal shows the best results for these analysis techniques because this is only a single study, and there has not been enough data collected to make this type of determination. This determination could depend strongly on other factors such as the geometry of the object of interest and its material properties.

4.6 Conclusion

Both sets of analysis resulted in useful findings about using the components of motion independently and together. It was shown that the relative frequency shift, ν, of the resonance peaks can be determined for certain modes through fairly simple analysis of the frequency spectra for each component across load levels. It was also shown that, in some instances, the in-plane component of motion may be more sensitive to stress changes than the normal component but that both components can be accurately used in this way.

Thorough examination of the relationship of the polarization curves and the frequency spectra revealed that it is not necessarily the peak amplitude that influences the accuracy of the polarization plot, but instead, it is primarily the separation in the peaks. It seems that the best combination for accuracy of the polarization curve is both good peak amplitude intensity and large magnitude shift in the frequency spectra of one or both components, but a high value of the frequency shift, ν, seems to be much more important than the intensity of the resonance peaks. Figure 39 shows an area where there is little intensity in the resonance peaks of the in-plane frequency spectra and almost no intensity in the resonance peaks of the normal spectra. However, these in-plane peaks show very distinct shifts for each load level which results in good resolution and order in the polarization plots in this very narrow frequency band.

It was also shown that by choosing an arbitrary window containing the direct arrival of the reverberant time signal and then filtering it over narrow bands corresponding to the most accurate portions of the polarization plots, ellipses can be created that seem to align well with the developed theory of the acoustoelastic effect.

There is generally an expansion of the major axis and a compression of the minor axis in the measured ellipses which also results in changes in the tilt of the ellipse. More investigation needs to be done in this area, but the preliminary findings as they relate to Lamb waves are promising.

CHAPTER 5
CONCLUSION

This thesis described the development of a 2D non-contact measurement system based on point LDV technology. The system is composed of various hardware components and controlled by National Instruments Labview 8.5 software.

Upon completion of the hardware-software integration, the accuracy of the 2D LDV measurement configuration was studied through comparison to a PCB Triaxial (3D) Accelerometer. Data was analyzed in the range of the accelerometer (0-4kHz), and when compared to the accelerometer signals, the LDV signals showed very good agreement in all areas of the time signals and corresponding frequency spectra for both components of motion. A basic analysis was also done showing that large angles of incidence measured from the plane of the surface of interest could produce data containing information from which the normal and in-plane components can be accurately extracted. This work with the comparison to the accelerometer validated the 2D configuration and showed the accuracy of the system compared to the established industry standard for obtaining such measurements.

Finally, the developed system was used to analyze the acoustoelastic effect in a small Aluminum plate under uniaxial compressive loading. The relationship of wave velocity to stress was detailed briefly, and analysis was conducted to determine what information could be extracted from the signal characteristics of the components of motion. First, each component was treated individually in an effort to determine how the relative frequency shift, ν, depends on the uniaxial compressive load. As the theory

suggests, linear relationships were observed, and fits to the data were used to determine the compansion parameter in several resonance peaks of the complex waveform. After this, the signals for the normal and in-plane components of the waveform were analyzed through multi-component joint analysis. This approach sought to determine metrics as well as qualitative measures which utilized both components simultaneously in order to determine how the relationship of the components is affected by changing applied load. The complexity of the Lamb wavefield made quantitative metrics difficult to measure directly, but by focusing on the areas of resonance in the frequency spectra, some promising signs were shown in plots of polarization angle versus frequency. In certain frequency bands, the polarization angle curve shows very good resolution. Time signal joint analysis was also conducted by filtering a selected window of the reverberant waveform in the narrowband corresponding to the accuracy of the polarization angle plot. Then, ellipses analogous to particle motion at the surface of the plate were generated. The developed theory implies that particle motion under compressive stress will expand in the normal direction and compress in the in-plane direction, and this phenomenon was generally observed on the plots. The complexities of the Lamb waveform containing many reflections made direct measurement difficult, but the results are promising for future low-frequency multi-dimensional vibration analysis applications.

Future work with this system will include continued investigation of the acoustoelastic effect in an aluminum plate through further quantitative analysis of the techniques used in this thesis. Other studies will also be performed on objects with different geometries, such as cylinders, and different material properties, such as polymers or gel members upon which traditional accelerometers cannot be attached.

Further developments in the measurement system will also include adding pairs of LDVs in order to take multiple 2D measurements of a surface simultaneously. Finally, the components will be reconfigured to perform scanning measurements with the implementation of a fast steering piezoelectric mirror which will allow the system to image low-frequency vibrations across the surface of an object.

APPENDIX A

POLYTEC PDV-100 POINT LASER DOPPLER VIBROMETER

PDV-100 Technical Data

General Specifications			
Decoder type	DSP velocity decoder, 3 measurement ranges		
Frequency range	0 … 22 kHz (digital output); 0.5 Hz … 22 kHz (analog output)		
Measurement ranges	3		
Full scale peak[1] (mm s^{-1})	20	100	500
Scaling factor (mm s^{-1}/V)	5	25	125
Velocity resolution[2] (μm s^{-1}/$\sqrt{}$Hz)	< 0.02	< 0.02	< 0.1
Maximum acceleration (m s^{-2})	2,760	13,800	69,000
Working distance[3]	0.1 m … ca. 30 m		
Laser safety	Eye-safe class II visible HeNe laser		

[1] Adjustable via the display.
[2] The resolution is defined as the signal amplitude (rms) at which the signal-to-noise ratio is 0 dB in a 1 Hz spectral bandwidth (RBW), measured on 3M Scotchlite® tape.
[3] The maximum stand-off distance depends on the surface properties of the object.

Output Signals	
Analog velocity output	
Output voltage swing	± 4 V (24 bit DAC)
Frequency range	0.5 Hz … 22 kHz
Dynamic range[1]	> 90 dB
Calibration accuracy	± 1 % (20 Hz … 22 kHz)
Digital velocity output	
Electrical S/P-DIF interface[2]	24 bit, 48 kSa/s
Frequency range	0 … 22 kHz
Calibration accuracy	± 0.2 % (0.05 Hz … 22 kHz)
Output filter	
Digital low pass filter (FIR type)	1, 5, 22 kHz (- 0.1dB), roll-off >120 dB/dec
Analog high pass filter	100 Hz (-3dB), roll-off - 60 dB/dec

[1] Defined as spurious free dynamic range (SFDR).
[2] S/P-DIF: Sony/Philips Digital Audio InterFace.

Housing and Power	
Dimensions L x W x H	300 mm x 63 mm x 129 mm (11.8 in x 2.5 in x 5.1 in)
Weight	~ 2.6 kg (~ 5.7 lbs)
Protection rating	IP 64 (dust and spray water protected)
Power	12 V DC, max. 15 W
Operating temperature	+5 °C … +40 °C (41°F … 104 °F)
Storage temperature	-10 °C … +65 °C (14 °F … 149 ° F)
Relative humidity	max. 80 %, non-condensing
Display	LCD, 3-line, with background lighting
Battery Kit PDV-BS	Rechargeable Li-Ion battery for min. 4 hours operation time

Compliance with Standards	
Electrical safety	IEC/EN61010
EMC	IEC/EN61326
Laser safety	IEC/EN60825-1

APPENDIX B

NI-cDAQ-9172 CHASSIS SPECIFICATIONS

Specifications

These specifications are for the NI cDAQ-9172 chassis only. These specifications are typical at 25 °C unless otherwise noted. For the C Series I/O module specifications, refer to the documentation for the C Series I/O modules you are using.

Analog Input

Input FIFO size .... 2,047 samples

Sample rate[1]

    Maximum... 3.2 MS/s
    (multi-channel, aggregate)

    Minimum .... 0 S/s

Timing accuracy[2] .... 50 ppm of sample rate

Timing resolution[2] .... 50 ns

Number of channels supported .... Determined by the C Series I/O modules

Analog Output

Numbers of channels supported

    In hardware-timed task 16

    In non-hardware-timed task .... Determined by the C Series I/O modules

Maximum update rate .... 1.6 MS/s
(multi-channel, aggregate)

Timing accuracy..................................... 50 ppm of sample rate

Timing resolution .... 50 ns

Output FIFO size.................................... 8,191 samples shared among channels used

---

[1] Performance dependent on type of installed C Series I/O modules and number of channels in the task.

[2] Does not include group delay. Refer to C Series I/O module documentation for more information.

AO waveform modes.................................Non-periodic waveform, periodic waveform regeneration mode from onboard memory, periodic waveform regeneration from host buffer including dynamic update

Digital Waveform Characteristics (Slots 1 through 4 Only)[1]

Waveform acquisition (DI)
FIFO..2,047 samples

Waveform generation (DO)
FIFO..2,047 samples

Digital input sample clock frequency
    Streaming to application
    memory..0 to 8 MHz, system dependent
    Finite..0 to 10 MHz

Digital output sample clock frequency
    Streaming from application
    memory..0 to 8 MHz, system dependent
    Regenerate from FIFO.....................0 to 10 MHz
    Finite..0 to 10 MHz

Digital output or digital input
sample clock source..................................Any PFI, analog sample or convert clock, analog output sample clock, Ctr n Internal Output, and many other sources

PFI Characteristics (Slots 5 and 6 Only)[1]

Functionality ....Static digital input, static digital output, timing input, and timing output

Timing output sources ....Many analog input, analog output, counter, digital input, and digital output timing signals

---

[1] Requires correlated digital I/O modules installed on the appropriate slot(s).

78

Debounce filter settings .... Selectable per input:
125 ns, 6.425 µs, 2.56 ms, disable, high and low transitions

Timing input frequency........................... 0 to 20 MHz

Timing output frequency......................... 0 to 20 MHz

General-Purpose Counter/Timers (Slots 5 and 6 Only)[1]

Number of counter/timers 2

Resolution .... 32 bits

Counter measurements .... Edge counting, pulse,
semi-period, period,
two-edge separation

Position measurements............................ X1, X2, X4 quadrature encoding
with Channel Z reloading;
two-pulse encoding

Output applications .... Pulse, pulse train with dynamic
updates, frequency division,
equivalent time sampling

Internal base clocks .... 80 MHz, 20 MHz, 100 kHz

External base clock frequency .... 0 to 20 MHz

Base clock accuracy .... 50 ppm

Output frequency..................................... 0 to 20 MHz

Inputs.. Gate, Source, HW_Arm, Aux,
A, B, Z, Up_Down

Routing options for inputs....................... Any PFI, analog trigger,
many internal signals

FIFO .... 2 samples

Data transfers .... High-speed data stream,
programmed I/O

---

[1] Requires correlated digital I/O modules installed in the appropriate slot(s).

Frequency Generator (Slots 5 and 6 Only)

Number of channels................................1

Base clocks ....10 MHz, 100 kHz

Divisors...1 to 16 (integers)

Base clock accuracy................................50 ppm

Output is available on any PFI terminal.

External Digital Triggers (Slots 5 and 6 or with Some AI Modules)

Source ....Any PFI terminal

Polarity...Software-selectable for most signals

Analog input function ....Start Trigger, Reference Trigger, Pause Trigger, Sample Clock, Sample Clock Timebase

Analog output function ....Start Trigger, Pause Trigger, Sample Clock, Sample Clock Timebase

Counter/timer functions..........................Gate, Source, HW_Arm, Aux, A, B, Z, Up_Down

Module I/O States

At power-on...Module-dependent. Refer to the documentation included with the C Series I/O module(s).

With USB cable removed ....Reverts to power-on state

Power Requirements

You must use a National Electric Code (NEC) Class 2 power source with the NI cDAQ-9172 chassis.

Note Some I/O modules have additional power requirements. For more information about C Series I/O module(s) power requirements, refer to documentation included with the C Series I/O module(s).

Note Sleep mode for C Series I/O modules is not supported in the NI cDAQ-9172.

Input voltage range.................................. 11 V to 30 V

Maximum required input power .... 15 W

Power input connector .... DC input jack with locking, threaded ring 0.8 in. (2 mm) center pin

Power input mating connector .... Switchcraft S760K

Bus Interface

USB specification .... USB 2.0 Hi-Speed

Power from USB

4.10 to 5.25 V .... 500 µA maximum

High-performance data streams 4

Types available .... Analog input, analog output, digital input, digital output, counter/timer input

Physical Characteristics

Chassis weight (unloaded) .... Approx. 840 g (1 lb 13 oz)

Chassis dimensions (unloaded).............. 25.4 cm × 8.81 cm × 5.89 cm (10.0 in. × 3.5 in. × 2.3 in.)

Safety

If you need to clean the chassis, wipe it with a dry towel.

This product is designed to meet the requirements of the following standards of safety for electrical equipment for measurement, control, and laboratory use:

- IEC 61010-1, EN-61010-1
- UL 61010-1, CSA 61010-1

Note For UL and other safety certifications, refer to the product label or visit ni.com/certification, search by model number or product line, and click the appropriate link in the Certification column.

81

Environmental

The NI cDAQ-9172 chassis is intended for indoor use only. For outdoor use, mount the system in a suitably rated enclosure.

Operating temperature[1]
(IEC-60068-2-1 and IEC-60068-2-2).....−20 to 55 °C

Storage temperature
(IEC-60068-2-1 and IEC-60068-2-2).....−40 to 85 °C

Ingress protection ....IP 30

Operating humidity
(IEC-60068-2-56) ....10 to 90% RH, noncondensing

Storage humidity
(IEC-60068-2-56) ....5 to 95% RH, noncondensing

Maximum altitude...................................2,000 m

Pollution Degree (IEC 60664)................2

Shock and Vibration

To meet these specifications, you must panel mount the NI cDAQ-9172 system and affix ferrules to the ends of the terminal lines.

Operational shock ....30 g peak, half-sine, 11 ms pulse
(Tested in accordance with IEC-60068-2-27. Test profile developed in accordance with MIL-PRF-28800F.)

Random vibration

    Operating ....5 to 500 Hz, 0.3 g_{rms}

    Nonoperating ....5 to 500 Hz, 2.4 g_{rms}
(Tested in accordance with IEC-60068-2-64. Nonoperating test profile exceeds the requirements of MIL-PRF-28800F, Class 3.)

---

[1] When operated in temperatures below 0 °C, you must use the PS-5 power supply, or another power supply rated for below 0 °C.

Electromagnetic Compatibility

This product is designed to meet the requirements of the following standards of EMC for electrical equipment for measurement, control, and laboratory use:

- EN 61326 EMC requirements; Minimum Immunity
- EN 55011 Emissions; Group 1, Class A
- CE, C-Tick, ICES, and FCC Part 15 Emissions; Class A

Note For EMC compliance, operate this device according to product documentation.

CE Compliance

This product meets the essential requirements of applicable European Directives, as amended for CE marking, as follows:

- 2006/95/EC; Low-Voltage Directive (safety)
- 2004/108/EC; Electromagnetic Compatibility Directive (EMC)

Note Refer to the Declaration of Conformity (DoC) for this product for any additional regulatory compliance information. To obtain the DoC for this product, visit ni.com/certification, search by model number or product line, and click the appropriate link in the Certification column.

Environmental Management

National Instruments is committed to designing and manufacturing products in an environmentally responsible manner. NI recognizes that eliminating certain hazardous substances from our products is beneficial not only to the environment but also to NI customers.

For additional environmental information, refer to the *NI and the Environment* Web page at ni.com/environment. This page contains the environmental regulations and directives with which NI complies, as well as other environmental information not included in this document.

Waste Electrical and Electronic Equipment (WEEE)

EU Customers At the end of their life cycle, all products *must* be sent to a WEEE recycling center. For more information about WEEE recycling centers and National Instruments WEEE initiatives, visit ni.com/environment/weee.htm.

电子信息产品污染控制管理办法 （中国 RoHS）

中国客户 National Instruments 符合中国电子信息产品中限制使用某些有害物质指令 (RoHS)。关于 National Instruments 中国 RoHS 合规性信息，请登录 ni.com/environment/rohs_china。(For information about China RoHS compliance, go to ni.com/environment/rohs_china.)

APPENDIX C

MATLAB CODE

BASIC CODE USED TO LOAD DATA RECORDED USING THE FINAL VI

```
clear all
filename=uigetfile({'*.dat;*.bin;*.dbl','Binary Files
(*.dat,*.bin,*.dbl)';...
    '*.*','All Files (*.*)'},'Please Select Binary File');
    FPATH='C:\Documents and Settings\WES\Desktop\Vib Msmt Research\Work
in Progress Data\Verify 2D Msmt w Accel\';
fid=fopen([FPATH,filename],'r');
temp=fread(fid,inf,'double');
freq1=temp(1); %Hz
num_ch=temp(2); %Number of Channels Recorded
samples_ch = (length(temp)-2)/num_ch; %Number of samples per channel
for idx=1:num_ch
        data1(:,idx)=temp((3+(samples_ch*(idx-
1))):((idx*samples_ch)+2));
end
time1=1/freq1:1/freq1:(length(data1(:,1)))/freq1;
%save data.mat 'data1' 'time' 'freq';
% fclose all; clear fid temp idx idx2 ans %filename ans;

%Note on for loop: Binary file for laser trigger and save multifile is
written one channel at
%a time with each channel being written entirely before the next
channel
%begins. i.e. 3:'samples per channel+2' = channel 1 data, 'samples per
%channel+3':2*'samples per channel +2' = channel 2 data, etc.

N1=length(time1);
Ts1=1/freq1;
Faxis=[0:N1-1]/N1/Ts1;


[B,A] = butter(4,[6e3 22e3]/(freq1/2));%band -pass
% [B,A] = butter(7,[50]/(freq1/2),'low');
C=filter(B,A,data1(:,:));
c=abs(fft(C));%fft(C(:,1:2));
```

CODE USED FOR ACCELEROMETER VS LDV COMPARISON

```
clear all
filenameL=uigetfile({'*.dat;*.bin;*.dbl','Binary Files
(*.dat,*.bin,*.dbl)';...
    '*.*','All Files (*.*)'},'Please Select Binary File');
    FPATH='C:\Documents and Settings\Sarah Herbison\Desktop\Vib Msmt
Research\Work in Progress Data\Plate Stress Test\';
```

```matlab
fid=fopen([FPATH,filenameL],'r');
tempL=fread(fid,inf,'double');
freqL=tempL(1); %Hz
num_chL=tempL(2); %Number of Channels Recorded
samples_chL = (length(tempL)-2)/num_chL; %Number of samples per channel
for idx=1:num_chL
        dataL(:,idx)=tempL((3+(samples_chL*(idx-
1))):((idx*samples_chL)+2));
end
timeL=1/freqL:1/freqL:(length(dataL(:,1)))/freqL;
%save data.mat 'data1' 'time' 'freq';
fclose all; clear fid tempL idx idx2 ans %filename ans;


NL=length(timeL);
TsL=1/freqL;
FaxisL=[0:NL-1]/NL/TsL;


tcorr=[(-(NL-1):NL-1)].*TsL;


%Filter LDV data
[B,A] = butter(4,[3e3 21.9e3]/(freqL/2));%band -pass
% [B,A] = butter(7,[50]/(freqL/2),'low');


%LDV 1 Velocity data
dataLfilt=filtfilt(B,A,dataL(:,2:6));
dataLfilt_fft=(fft(dataLfilt));%fft(LDV(:,1:2));
% LDV_fft=abs(fft(dataL(:,2:4)));


%Acceleration from LDV
for i=1:5
    d_dataLfilt(:,i)=gradient(dataLfilt(:,i));
end
% dLDV=gradient(dataL(:,2:4));
d_dataLfilt_fft=(fft(d_dataLfilt));


%Extract u_x and u_z
theta = 71.57;
u_z=dataLfilt(:,3);
u_z1=(dataLfilt(:,4)+dataLfilt(:,5))/(2.*sind(theta));
u_x=(dataLfilt(:,4)-dataLfilt(:,5))/(2.*cosd(theta));


%Convert to acceleration
a_z=gradient(u_z);
a_x=gradient(u_x);


%Normalize, and plot acceleration along z-axis
m_Lz=max(u_z);

figure()
plot(timeL,u_z./m_Lz,'r')
title('Normalized Normal Velocity')
xlabel('Time(s)')
ylabel('Voltage(V)')


%Normalize, and plot acceleration along x-axis
```

85

```matlab
m_Lx=max(u_x);

figure()
plot(timeL,u_x./m_Lx,'r')
title('Normalized In-plane Velocity')
xlabel('Time(s)')
ylabel('Voltage(V)')

%Convert, normalize, and plot signals in frequency domain
u_x_fft=(fft(u_x));
u_z_fft=(fft(u_z));

% m_Lxfft=max(a_x_fft);
% m_Lzfft=max(a_z_fft);

figure(5)
plot(FaxisL,abs(u_z_fft),'r');hold on
title('Normalized Frequency Spectrum of Normal Velocity')
xlabel('Frequecy(Hz)')
ylabel('Intensity')

figure(6)
plot(FaxisL,abs(u_x_fft),'r');hold on
title('Normalized Frequency Spectrum of In-plane Velocity')
xlabel('Frequecy(Hz)')
ylabel('Intensity')

%Isolate the "good" portion of the signal for elliptical analysis
t1=.10124; %start time of initial excitation
t2=.1018; %t1 + (1/bandwidth) or end of signal agreement with
accelerometer
% t1=.1203;%Reflected wave??
% t2=.12086;
% t1=.10236;
% t2=.10292;
Int=find(timeL>t1&timeL<t2);

%LDV
u_x_win=zeros(size(u_x));
u_x_win(Int)=u_x(Int).*hanning(length(Int));
u_z_win=zeros(size(u_z));
u_z_win(Int)=u_z(Int).*hanning(length(Int));
u_x_winfft=fft(u_x_win);
u_z_winfft=fft(u_z_win);
angle_a=unwrap(angle(u_x_winfft./u_z_winfft));

figure()
plot(FaxisL,angle_a,'b')


%Filter LDV data
f1=12000;
f2=12010;
[C,D] = butter(4,[f1 f2]/(freqL/2));%band -pass
% [B,A] = butter(7,[50]/(freqL/2),'low');
```

```matlab
u_x_winfilt=filtfilt(C,D,u_x_win);
u_x_winfilt_fft=fft(u_x_winfilt);%fft(LDV(:,1:2));
u_z_winfilt=filtfilt(C,D,u_z_win);
u_z_winfilt_fft=fft(u_z_winfilt);

%Interpolate data to improve resolution
idx=1:length(Int);
idx_spline=[idx(1):.005:idx(end)];
u_x_spline=spline(idx,u_x_winfilt(Int),idx_spline);
u_z_spline=spline(idx,u_z_winfilt(Int),idx_spline);

figure();clf;hold on
plot(u_x_spline)
plot(u_z_spline,'r')

figure();clf;hold on
plot(u_x_spline,u_z_spline,'b.')

figure()
plot(abs(u_x_winfilt_fft))

figure()
plot(abs(u_z_winfilt_fft))
```

CODE USED FOR TO DETERMINE OPTIMAL ANGLE FOR OUTER LDVS

```matlab
clear all
filenameL=uigetfile({'*.dat;*.bin;*.dbl','Binary Files
(*.dat,*.bin,*.dbl)';...
    '*.*','All Files (*.*)'},'Please Select Binary File');
    FPATH='F:\Vib Msmt Research\Work in Progress Data\Verify 2D Msmt w
Accel\Simultaneous collection 2D\Angle~45\';
fid=fopen([FPATH,filenameL],'r');
tempL=fread(fid,inf,'double');
freqL=tempL(1); %Hz
num_chL=tempL(2); %Number of Channels Recorded
samples_chL = (length(tempL)-2)/num_chL; %Number of samples per channel
for idx=1:num_chL
        dataL(:,idx)=tempL((3+(samples_chL*(idx-
1))):((idx*samples_chL)+2));
end
timeL=1/freqL:1/freqL:(length(dataL(:,1)))/freqL;
%save data.mat 'data1' 'time' 'freq';
fclose all; clear fid tempL idx idx2 ans %filename ans;

%Note on for loop: Binary file for laser trigger and save multifile is
written one channel at
%a time with each channel being written entirely before the next
channel
%begins. i.e. 3:'samples per channel+2' = channel 1 data, 'samples per
%channel+3':2*'samples per channel +2' = channel 2 data, etc.
```

```matlab
filenameL2=uigetfile({'*.dat;*.bin;*.dbl','Binary Files
(*.dat,*.bin,*.dbl)';...
    '*.*','All Files (*.*)'},'Please Select Binary File');
    FPATH='F:\Vib Msmt Research\Work in Progress Data\Verify 2D Msmt w
Accel\Simultaneous collection 2D\Angle~60\';
fid=fopen([FPATH,filenameL2],'r');
tempL2=fread(fid,inf,'double');
freqL2=tempL2(1); %Hz
num_chL2=tempL2(2); %Number of Channels Recorded
samples_chL2 = (length(tempL2)-2)/num_chL2; %Number of samples per
channel
for idx=1:num_chL2
        dataL2(:,idx)=tempL2((3+(samples_chL2*(idx-
1))):((idx*samples_chL2)+2));
end
timeL2=1/freqL2:1/freqL2:(length(dataL2(:,1)))/freqL2;
%save data.mat 'data1' 'time' 'freq';
fclose all; clear fid tempL2 idx idx2 ans %filename ans;


filenameL3=uigetfile({'*.dat;*.bin;*.dbl','Binary Files
(*.dat,*.bin,*.dbl)';...
    '*.*','All Files (*.*)'},'Please Select Binary File');
    FPATH='F:\Vib Msmt Research\Work in Progress Data\Verify 2D Msmt w
Accel\Simultaneous collection 2D\Angle~73\';
fid=fopen([FPATH,filenameL3],'r');
tempL3=fread(fid,inf,'double');
freqL3=tempL3(1); %Hz
num_chL3=tempL3(2); %Number of Channels Recorded
samples_chL3 = (length(tempL3)-2)/num_chL3; %Number of samples per
channel
for idx=1:num_chL3
        dataL3(:,idx)=tempL3((3+(samples_chL3*(idx-
1))):((idx*samples_chL3)+2));
end
timeL3=1/freqL3:1/freqL3:(length(dataL3(:,1)))/freqL3;
%save data.mat 'data1' 'time' 'freq';
fclose all; clear fid tempL3 idx idx2 ans %filename ans;


filenameL4=uigetfile({'*.dat;*.bin;*.dbl','Binary Files
(*.dat,*.bin,*.dbl)';...
    '*.*','All Files (*.*)'},'Please Select Binary File');
    FPATH='F:\Vib Msmt Research\Work in Progress Data\Verify 2D Msmt w
Accel\Simultaneous collection 2D\Angle~80\';
fid=fopen([FPATH,filenameL4],'r');
tempL4=fread(fid,inf,'double');
freqL4=tempL4(1); %Hz
num_chL4=tempL4(2); %Number of Channels Recorded
samples_chL4 = (length(tempL4)-2)/num_chL4; %Number of samples per
channel
for idx=1:num_chL4
        dataL4(:,idx)=tempL4((3+(samples_chL4*(idx-
1))):((idx*samples_chL4)+2));
end
timeL4=1/freqL4:1/freqL4:(length(dataL4(:,1)))/freqL4;
%save data.mat 'data1' 'time' 'freq';
fclose all; clear fid tempL4 idx idx2 ans %filename ans;
```

```matlab
filenameL5=uigetfile({'*.dat;*.bin;*.dbl','Binary Files
(*.dat,*.bin,*.dbl)';...
    '*.*','All Files (*.*)'},'Please Select Binary File');
    FPATH='F:\Vib Msmt Research\Work in Progress Data\Verify 2D Msmt w
Accel\Simultaneous collection 2D\Angle~83\';
fid=fopen([FPATH,filenameL5],'r');
tempL5=fread(fid,inf,'double');
freqL5=tempL5(1); %Hz
num_chL5=tempL5(2); %Number of Channels Recorded
samples_chL5 = (length(tempL5)-2)/num_chL5; %Number of samples per
channel
for idx=1:num_chL5
        dataL5(:,idx)=tempL5((3+(samples_chL5*(idx-
1))):((idx*samples_chL5)+2));
end
timeL5=1/freqL5:1/freqL5:(length(dataL5(:,1)))/freqL5;
%save data.mat 'data1' 'time' 'freq';
fclose all; clear fid tempL5 idx idx2 ans %filename ans;

% filenameA=uigetfile({'*.dat;*.bin;*.dbl','Binary Files
(*.dat,*.bin,*.dbl)';...
%     '*.*','All Files (*.*)'},'Please Select Binary File');
%     FPATH='C:\Documents and Settings\Sarah Herbison\Desktop\Vib Msmt
Research\Work in Progress Data\Verify 2D Msmt w Accel\';
% fid=fopen([FPATH,filenameA],'r');
% tempA=fread(fid,inf,'double');
% freqA=tempA(1); %Hz
% num_chA=tempA(2); %Number of Channels Recorded
% samples_chA = (length(tempA)-2)/num_chA; %Number of samples per
channel
% for idx=1:num_chA
%         dataA(:,idx)=tempA((3+(samples_chA*(idx-
1))):((idx*samples_chA)+2));
% end
% timeA=1/freqA:1/freqA:(length(dataA(:,1)))/freqA;
% fclose all; clear fid tempA idx idx2 ans %filename ans;

NL=length(timeL);
TsL=1/freqL;
FaxisL=[0:NL-1]/NL/TsL;

tcorr=[(-(NL-1):NL-1)].*TsL;

NL2=length(timeL2);
TsL2=1/freqL2;
FaxisL2=[0:NL2-1]/NL2/TsL2;

tcorr2=[(-(NL2-1):NL2-1)].*TsL2;

NL3=length(timeL3);
TsL3=1/freqL3;
FaxisL3=[0:NL3-1]/NL3/TsL3;

tcorr3=[(-(NL3-1):NL3-1)].*TsL3;
```

```matlab
NL4=length(timeL4);
TsL4=1/freqL4;
FaxisL4=[0:NL4-1]/NL4/TsL4;


tcorr4=[(-(NL4-1):NL4-1)].*TsL4;


NL5=length(timeL5);
TsL5=1/freqL5;
FaxisL5=[0:NL5-1]/NL5/TsL5;


tcorr5=[(-(NL5-1):NL5-1)].*TsL5;


% NA=length(timeA);
% TsA=1/freqA;
% FaxisA=[0:NA-1]/NA/TsA;


%Filter LDV data
[B,A] = butter(4,[100 2.5e3]/(freqL/2));%band -pass
% [B,A] = butter(7,[50]/(freqL/2),'low');


%LDV 1 Velocity data
dataLfilt=filtfilt(B,A,dataL(:,2:6));
dataLfilt_fft=abs(fft(dataLfilt));%fft(LDV(:,1:2));
% LDV_fft=abs(fft(dataL(:,2:4)));


%Acceleration from LDV
for i=1:5
    d_dataLfilt(:,i)=gradient(dataLfilt(:,i));
end
% dLDV=gradient(dataL(:,2:4));
d_dataLfilt_fft=abs(fft(d_dataLfilt));


%LDV 2 Velocity data
dataLfilt2=filtfilt(B,A,dataL2(:,2:6));
dataLfilt2_fft=abs(fft(dataLfilt2));%fft(LDV(:,1:2));
% LDV_fft=abs(fft(dataL2(:,2:4)));


%Acceleration from LDV
for i=1:5
    d_dataLfilt2(:,i)=gradient(dataLfilt2(:,i));
end
% dLDV=gradient(dataL(:,2:4));
d_dataLfilt2_fft=abs(fft(d_dataLfilt2));


%LDV 3 Velocity data
dataLfilt3=filtfilt(B,A,dataL3(:,2:6));
dataLfilt3_fft=abs(fft(dataLfilt3));%fft(LDV(:,1:2));
% LDV_fft=abs(fft(dataL(:,2:4)));


%Acceleration from LDV
for i=1:5
    d_dataLfilt3(:,i)=gradient(dataLfilt3(:,i));
end
```

```matlab
% dLDV=gradient(dataL(:,2:4));
d_dataLfilt3_fft=abs(fft(d_dataLfilt3));


%LDV 4 Velocity data
dataLfilt4=filtfilt(B,A,dataL4(:,2:6));
dataLfilt4_fft=abs(fft(dataLfilt4));%fft(LDV(:,1:2));
% LDV_fft=abs(fft(dataL(:,2:4)));


%Acceleration from LDV
for i=1:5
    d_dataLfilt4(:,i)=gradient(dataLfilt4(:,i));
end
% dLDV=gradient(dataL(:,2:4));
d_dataLfilt4_fft=abs(fft(d_dataLfilt4));


%LDV 5 Velocity data
dataLfilt5=filtfilt(B,A,dataL5(:,2:6));
dataLfilt5_fft=abs(fft(dataLfilt5));%fft(LDV(:,1:2));
% LDV_fft=abs(fft(dataL(:,2:4)));


%Acceleration from LDV
for i=1:5
    d_dataLfilt5(:,i)=gradient(dataLfilt5(:,i));
end
% dLDV=gradient(dataL(:,2:4));
d_dataLfilt5_fft=abs(fft(d_dataLfilt5));


% %Filter Accelerometer data
% [D,C] = butter(4,[100 3.9e3]/(freqA/2));%band -pass
% % [B,A] = butter(7,[50]/(freqA/2),'low');
%
% %Acceleration from Accelerometer
% Acc=filtfilt(D,C,dataA(:,2:3));
% Acc_fft=(fft(Acc));%fft(Acc(:,1:2));


% figure(1)
% plot(timeL,dataLfilt(:,3))
% title('Time Series LDV Data')
%
% figure(2)
% plot(timeL,dataLfilt(:,5:6))
% title('Time Series Left LDV Data')
%
% figure(3)
% plot(FaxisL,dataLfilt_fft(:,2:3))
% title('Frequency Spectrum Right LDV Data')
%
% figure(4)
% plot(FaxisL,dataLfilt_fft(:,3))
% title('Frequency Spectrum Left LDV Data')
%
% % figure(3)
% % plot(timeA,Acc(:,1));hold on
% % plot(timeA,Acc(:,2)+.07,'g')
% % title('Time Series Accelerometer Data')
%
```

```matlab
% figure(5)
% plot(timeL,d_dataLfilt(:,3)+.2);hold on
% plot(timeL,dataLfilt(:,1),'k')
% legend('Derivative of LDV signal','Accelerometer Signal')
% title('Time Signal Comparison; both signals filtered from 100-3900Hz,
LDV signal offset by +.07V')
% xlabel('Time(s)')
% ylabel('Voltage(V)')
%
% figure(6)
% plot(FaxisL,abs(d_dataLfilt_fft(:,3))); hold on
% plot(FaxisL,abs(dataLfilt_fft(:,1)),'k')
% title('Frequency Spectrum Accelerometer')
% legend('Derivative of LDV signal','Accelerometer Signal')
%
% % %Whiten signal to eliminate difference in magnitude due to
different
% % %sensor. Phase will be preserved and this is what we are concerned
about in
% % %the rebuilt signal.
% % %Whiten dLDV_fft and rebuild dLDV
% % Fmin=3e3;
% % Fmax=4e3;
% %
% % If=find((FaxisL>=Fmin) & (FaxisL<=Fmax));
% % [M,I]=max(abs(dLDV_fft(If,:)));
% % E=(1/50).*M;
% %
% % for ee=1:3;
% % dLDV_fft2(:,ee)=dLDV_fft(:,ee)./(abs(dLDV_fft(:,ee))+E(ee));
% % end
% %
% % figure(5)
% % plot(abs(dLDV_fft2(:,1)))
% %
% % dLDV_fft3=zeros(size(dLDV_fft2));
% % for ee=1:3;
% % dLDV_fft3(If,ee)=dLDV_fft2(If,ee).*((hanning(length(If)))).^0.5;
% % end
% %
% % f=['b' 'k' 'r'];
% % figure(6)
% % for ee=1:3;
% % plot(FaxisL,abs(dLDV_fft3(:,ee)),f(ee)); hold on
% % end
% %
% % %Inverse FFT back to time domain
% % dLDV_t2=2*real(ifft(dLDV_fft3));
% %
% % figure(7)
% % plot(timeL,dLDV_t2(:,1)+.04,'r');hold on
% %
% % %Whiten Acc_fft using same frequency range as LDV signal and
rebuild Acc
% % If=find((FaxisL>=Fmin) & (FaxisL<=Fmax));
% % [MA,IA]=max(abs(Acc_fft(If,:)));
```

```matlab
% % EA=(1/50).*MA;
% %
% % for ee=1:2;
% % Acc_fft2(:,ee)=Acc_fft(:,ee)./(abs(Acc_fft(:,ee))+EA(ee));
% % end
% %
% % figure(8)
% % plot(abs(Acc_fft2(:,1)))
% %
% % If=find((FaxisA>=Fmin) & (FaxisA<=Fmax));
% % Acc_fft3=zeros(size(Acc_fft2));
% % for ee=1:2;
% % Acc_fft3(If,ee)=Acc_fft2(If,ee).*((hanning(length(If)))).^0.5;
% % end
% %
% % f=['k' 'b'];
% % figure(9)
% % for ee=1:2;
% % plot(FaxisA,abs(Acc_fft3(:,ee)),f(ee)); hold on
% % end
% %
% % %Inverse FFT back to time domain
% % Acc_t2=2*real(ifft(Acc_fft3));
% %
% % figure(10)
% % plot(timeA,Acc_t2)
%
% %Compare time signal of z-axis acceleration from LDV and
% Accelerometer data
% XCORR=xcorr(dataLfilt(:,1),d_dataLfilt(:,3),'coeff');
% figure(11)
% plot(tcorr,XCORR)
%
% [Y I]=max(XCORR);
% delay_I=length(FaxisL)-I;
% delay_T=tcorr(I);
% figure(12)
% plot(timeL,dataLfilt(:,1),'k');hold on
% plot(timeL+delay_T,d_dataLfilt(:,3))
% title('Z-axis Acceleration Data in Time Domain')
% legend('Accelerometer signal','LDV 1 signal','LDV 2 signal')
% xlabel('time(s)')
% ylabel('Relative Acceleration')

%Extract u_x and u_z
theta = 45.25;
u_z=dataLfilt(:,3);
u_x=(dataLfilt(:,4)-dataLfilt(:,5))/(2.*cosd(theta));

%Convert to acceleration
a_z=gradient(u_z);
a_x=gradient(u_x);

%Extract u_x and u_z
theta2 = 60.87;
u_z2=dataLfilt2(:,3);
```

93

```matlab
u_x2=(dataLfilt2(:,4)-dataLfilt2(:,5))/(2.*cosd(theta2));

%Convert to acceleration
a_z2=gradient(u_z2);
a_x2=gradient(u_x2);

%Extract u_x and u_z
theta3 = 73.50;
u_z3=dataLfilt3(:,3);
u_x3=(dataLfilt3(:,4)-dataLfilt3(:,5))/(2.*cosd(theta3));

%Convert to acceleration
a_z3=gradient(u_z3);
a_x3=gradient(u_x3);

%Extract u_x and u_z
theta4 = 80.82;
u_z4=dataLfilt4(:,3);
u_x4=(dataLfilt4(:,4)-dataLfilt4(:,5))/(2.*cosd(theta4));

%Convert to acceleration
a_z4=gradient(u_z4);
a_x4=gradient(u_x4);

%Extract u_x and u_z
theta5 = 83.85;
u_z5=dataLfilt5(:,3);
u_x5=(dataLfilt5(:,4)-dataLfilt5(:,5))/(2.*cosd(theta5));

%Convert to acceleration
a_z5=gradient(u_z5);
a_x5=gradient(u_x5);

%Shift and plot acceleration along z-axis
XCORR_z=xcorr(dataLfilt(:,1),a_z,'coeff');
figure(13)
plot(tcorr,XCORR_z)
title('Cross-Correlation of Normal Acceleration of Accelerometer and
LDV 1')

[Y_z I_z]=max(XCORR_z);
delay_I_z=length(FaxisL)-I_z;
delay_T_z=tcorr(I_z);

%LDV 2
XCORR_z2=xcorr(dataLfilt2(:,1),a_z2,'coeff');
figure(14)
plot(tcorr2,XCORR_z2)
title('Cross-Correlation of Normal Acceleration of Accelerometer and
LDV 2')

[Y_z2 I_z2]=max(XCORR_z2);
delay_I_z2=length(FaxisL2)-I_z2;
delay_T_z2=tcorr(I_z2);
```

```matlab
%LDV 3
XCORR_z3=xcorr(dataLfilt3(:,1),a_z3,'coeff');
figure(15)
plot(tcorr3,XCORR_z3)
title('Cross-Correlation of Normal Acceleration of Accelerometer and
LDV 3')

[Y_z3 I_z3]=max(XCORR_z3);
delay_I_z3=length(FaxisL3)-I_z3;
delay_T_z3=tcorr(I_z3);

%LDV 4
XCORR_z4=xcorr(dataLfilt4(:,1),a_z4,'coeff');
figure(16)
plot(tcorr4,XCORR_z4)
title('Cross-Correlation of Normal Acceleration of Accelerometer and
LDV 3')

[Y_z4 I_z4]=max(XCORR_z4);
delay_I_z4=length(FaxisL4)-I_z4;
delay_T_z4=tcorr(I_z4);

%LDV 5
XCORR_z5=xcorr(dataLfilt5(:,1),a_z5,'coeff');
figure(17)
plot(tcorr5,XCORR_z5)
title('Cross-Correlation of Normal Acceleration of Accelerometer and
LDV 3')

[Y_z5 I_z5]=max(XCORR_z5);
delay_I_z5=length(FaxisL5)-I_z5;
delay_T_z5=tcorr(I_z5);

% figure(16)
% plot(timeL,dataLfilt(:,1),'k');hold on
% plot(timeL+delay_T_z,a_z,'r')
% title('Normal Acceleration')
% legend('Accelerometer signal','LDV signal')
% xlabel('Time(s)')
% ylabel('Voltage(V)')

%Normalize Signals and Plot
%LDV 1
m_az=max(dataLfilt(:,1));
m_Lz=max(a_z);

figure(18)
plot(timeL,dataLfilt(:,1)./m_az,'k');hold on
plot(timeL+delay_T_z,a_z./m_Lz,'r')
title('Normalized Normal Acceleration')
legend('Accelerometer signal','LDV 1 signal')
xlabel('Time(s)')
ylabel('Voltage(V)')
```

```matlab
%LDV 2
m_az2=max(dataLfilt2(:,1));
m_Lz2=max(a_z2);

figure(19)
plot(timeL2,dataLfilt2(:,1)./m_az2,'k');hold on
plot(timeL2+delay_T_z2,a_z2./m_Lz2,'r')
title('Normalized Normal Acceleration')
legend('Accelerometer signal','LDV 2 signal')
xlabel('Time(s)')
ylabel('Voltage(V)')

%LDV 3
m_az3=max(dataLfilt3(:,1));
m_Lz3=max(a_z3);

figure(20)
plot(timeL3,dataLfilt3(:,1)./m_az3,'k');hold on
plot(timeL3+delay_T_z3,a_z3./m_Lz3,'r')
title('Normalized Normal Acceleration')
legend('Accelerometer signal','LDV 3 signal')
xlabel('Time(s)')
ylabel('Voltage(V)')

%LDV4
m_az4=max(dataLfilt4(:,1));
m_Lz4=max(a_z4);

figure(21)
plot(timeL4,dataLfilt4(:,1)./m_az4,'k');hold on
plot(timeL4+delay_T_z4,a_z4./m_Lz4,'r')
title('Normalized Normal Acceleration')
legend('Accelerometer signal','LDV 4 signal')
xlabel('Time(s)')
ylabel('Voltage(V)')

%LDV 5
m_az5=max(dataLfilt5(:,1));
m_Lz5=max(a_z5);

figure(22)
plot(timeL5,dataLfilt5(:,1)./m_az5,'k');hold on
plot(timeL5+delay_T_z5,a_z5./m_Lz5,'r')
title('Normalized Normal Acceleration')
legend('Accelerometer signal','LDV 5 signal')
xlabel('Time(s)')
ylabel('Voltage(V)')

%Shift and plot acceleration along x-axis
XCORR_x=xcorr(dataLfilt(:,2),a_x,'coeff');
figure(23)
plot(tcorr,XCORR_x)
title('Cross-Correlation of In-plane Acceleration of Accelerometer and
LDV 1')
```

```matlab
[Y_x I_x]=max(XCORR_x);
delay_I_x=length(FaxisL)-I_x;
delay_T_x=tcorr(I_x);

%LDV 2
XCORR_x2=xcorr(dataLfilt2(:,2),a_x2,'coeff');
figure(24)
plot(tcorr2,XCORR_x2)
title('Cross-Correlation of In-plane Acceleration of Accelerometer and
LDV 2')

[Y_x2 I_x2]=max(XCORR_x2);
delay_I_x2=length(FaxisL2)-I_x2;
delay_T_x2=tcorr(I_x2);

%LDV 3
XCORR_x3=xcorr(dataLfilt3(:,2),a_x3,'coeff');
figure(25)
plot(tcorr3,XCORR_x3)
title('Cross-Correlation of In-plane Acceleration of Accelerometer and
LDV 3')

[Y_x3 I_x3]=max(XCORR_x3);
delay_I_x3=length(FaxisL3)-I_x3;
delay_T_x3=tcorr(I_x3);

%LDV 4
XCORR_x4=xcorr(dataLfilt4(:,2),a_x4,'coeff');
figure(26)
plot(tcorr4,XCORR_x4)
title('Cross-Correlation of In-plane Acceleration of Accelerometer and
LDV 4')

[Y_x4 I_x4]=max(XCORR_x4);
delay_I_x4=length(FaxisL4)-I_x4;
delay_T_x4=tcorr(I_x4);

%LDV 5
XCORR_x5=xcorr(dataLfilt5(:,2),a_x5,'coeff');
figure(27)
plot(tcorr5,XCORR_x5)
title('Cross-Correlation of In-plane Acceleration of Accelerometer and
LDV 5')

[Y_x5 I_x5]=max(XCORR_x5);
delay_I_x5=length(FaxisL5)-I_x5;
delay_T_x5=tcorr(I_x5);

% figure(23)
% plot(timeL,dataLfilt(:,2),'k');hold on
% plot(timeL+delay_T_x,a_x,'r')
% title('In-plane Acceleration')
% legend('Accelerometer signal','LDV signal')
% xlabel('Time(s)')
% ylabel('Voltage(V)')
```

```matlab
%Normalize and Plot
%LDV1
m_ax=max(dataLfilt(:,2));
m_Lx=max(a_x);

figure(28)
plot(timeL,dataLfilt(:,2)./m_ax,'k');hold on
plot(timeL+delay_T_x,a_x./m_Lx,'r')
title('Normalized In-plane Acceleration, Data 1')
legend('Accelerometer signal','LDV signal')
xlabel('Time(s)')
ylabel('Voltage(V)')

%LDV 2
m_ax2=max(dataLfilt2(:,2));
m_Lx2=max(a_x2);

figure(29)
plot(timeL2,dataLfilt2(:,2)./m_ax2,'k');hold on
plot(timeL2+delay_T_x2,a_x2./m_Lx2,'r')
title('Normalized In-plane Acceleration, Data 2')
legend('Accelerometer signal','LDV signal')
xlabel('Time(s)')
ylabel('Voltage(V)')

%LDV 3
m_ax3=max(dataLfilt3(:,2));
m_Lx3=max(a_x3);

figure(30)
plot(timeL3,dataLfilt3(:,2)./m_ax3,'k');hold on
plot(timeL3+delay_T_x3,a_x3./m_Lx3,'r')
title('Normalized In-plane Acceleration, Data 3')
legend('Accelerometer signal','LDV signal')
xlabel('Time(s)')
ylabel('Voltage(V)')

%LDV 4
m_ax4=max(dataLfilt4(:,2));
m_Lx4=max(a_x4);

figure(31)
plot(timeL4,dataLfilt4(:,2)./m_ax4,'k');hold on
plot(timeL4+delay_T_x4,a_x4./m_Lx4,'r')
title('Normalized In-plane Acceleration, Data 4')
legend('Accelerometer signal','LDV signal')
xlabel('Time(s)')
ylabel('Voltage(V)')

%LDV 5
m_ax5=max(dataLfilt5(:,2));
m_Lx5=max(a_x5);

figure(32)
```

```matlab
plot(timeL5,dataLfilt5(:,2)./m_ax5,'k');hold on
plot(timeL5+delay_T_x5,a_x5./m_Lx5,'r')
title('Normalized In-plane Acceleration, Data 5')
legend('Accelerometer signal','LDV signal')
xlabel('Time(s)')
ylabel('Voltage(V)')

figure(33)
plot(timeL+delay_T_x,a_x,'b'); hold on
plot(timeL2+delay_T_x2,a_x2,'r'); hold on
plot(timeL3+delay_T_x3,a_x3,'k'); hold on
plot(timeL4+delay_T_x4,a_x4,'g'); hold on
plot(timeL5+delay_T_x5,a_x5,'c')
title('In-Plane Acceleration')
legend('Data 1','Data 2','Data 3','Data 4','Data 5')
xlabel('Time(s)')
ylabel('Voltage(V)')

%Convert and plot signals in frequency domain
a_x_fft=abs(fft(a_x));
a_z_fft=abs(fft(a_z));

a_x2_fft=abs(fft(a_x2));
a_z2_fft=abs(fft(a_z2));

a_x3_fft=abs(fft(a_x3));
a_z3_fft=abs(fft(a_z3));

a_x4_fft=abs(fft(a_x4));
a_z4_fft=abs(fft(a_z4));

a_x5_fft=abs(fft(a_x5));
a_z5_fft=abs(fft(a_z5));

% figure(34)
% plot(FaxisL,a_x_fft,'r');hold on
% plot(FaxisL,dataLfilt_fft(:,2),'k')
% title('Frequency Spectrum of In-plane Acceleration, Data 1')
% xlabel('Frequecy(Hz)')
% ylabel('Intensity')
%
% figure(35)
% plot(FaxisL,a_z_fft,'r');hold on
% plot(FaxisL,dataLfilt_fft(:,1),'k')
% title('Frequency Spectrum of Normal Acceleration, Data 1')
% xlabel('Frequecy(Hz)')
% ylabel('Intensity')

%Normalize and Plot Frequency Spectrum
m_axfft=max(dataLfilt_fft(:,2));
m_Lxfft=max(a_x_fft);
m_azfft=max(dataLfilt_fft(:,1));
m_Lzfft=max(a_z_fft);

m_ax2fft=max(dataLfilt2_fft(:,2));
```

```
m_Lx2fft=max(a_x2_fft);
m_az2fft=max(dataLfilt2_fft(:,1));
m_Lz2fft=max(a_z2_fft);


m_ax3fft=max(dataLfilt3_fft(:,2));
m_Lx3fft=max(a_x3_fft);
m_az3fft=max(dataLfilt3_fft(:,1));
m_Lz3fft=max(a_z3_fft);


m_ax4fft=max(dataLfilt4_fft(:,2));
m_Lx4fft=max(a_x4_fft);
m_az4fft=max(dataLfilt4_fft(:,1));
m_Lz4fft=max(a_z4_fft);


m_ax5fft=max(dataLfilt5_fft(:,2));
m_Lx5fft=max(a_x5_fft);
m_az5fft=max(dataLfilt5_fft(:,1));
m_Lz5fft=max(a_z5_fft);


%In-plane Frequency Spectrums
figure(36)
plot(FaxisL,a_x_fft./m_Lxfft,'r');hold on
plot(FaxisL,dataLfilt_fft(:,2)./m_axfft,'k')
title('Normalized Frequency Spectrum of In-plane Acceleration, Data 1')
xlabel('Frequecy(Hz)')
ylabel('Intensity')


figure(37)
plot(FaxisL2,a_x2_fft./m_Lx2fft,'r');hold on
plot(FaxisL2,dataLfilt2_fft(:,2)./m_ax2fft,'k')
title('Normalized Frequency Spectrum of In-plane Acceleration, Data 2')
xlabel('Frequecy(Hz)')
ylabel('Intensity')


figure(38)
plot(FaxisL3,a_x3_fft./m_Lx3fft,'r');hold on
plot(FaxisL3,dataLfilt3_fft(:,2)./m_ax3fft,'k')
title('Normalized Frequency Spectrum of In-plane Acceleration, Data 3')
xlabel('Frequecy(Hz)')
ylabel('Intensity')


figure(39)
plot(FaxisL4,a_x4_fft./m_Lx4fft,'r');hold on
plot(FaxisL4,dataLfilt4_fft(:,2)./m_ax4fft,'k')
title('Normalized Frequency Spectrum of In-plane Acceleration, Data 4')
xlabel('Frequecy(Hz)')
ylabel('Intensity')


figure(40)
plot(FaxisL5,a_x5_fft./m_Lx5fft,'r');hold on
plot(FaxisL5,dataLfilt5_fft(:,2)./m_ax5fft,'k')
title('Normalized Frequency Spectrum of In-plane Acceleration, Data 5')
xlabel('Frequecy(Hz)')
ylabel('Intensity')
```

```
figure(41)
plot(FaxisL,a_x_fft./m_Lxfft,'b');hold on
plot(FaxisL2,a_x2_fft./m_Lx2fft,'g');hold on
plot(FaxisL3,a_x3_fft./m_Lx3fft,'k');hold on
plot(FaxisL4,a_x4_fft./m_Lx4fft,'r');hold on
plot(FaxisL5,a_x5_fft./m_Lx5fft,'c')
title('Frequency Spectrum Comparison, In-Plane Acceleration')
legend('Data 1','Data 2','Data 3','Data 4','Data 5')
xlabel('Frequency (Hz)')
ylabel('Intensity')


figure(42)
plot(FaxisL,dataLfilt_fft(:,2)./m_axfft,'b'); hold on
plot(FaxisL2,dataLfilt2_fft(:,2)./m_ax2fft,'r'); hold on
plot(FaxisL3,dataLfilt3_fft(:,2)./m_ax3fft,'g'); hold on
plot(FaxisL4,dataLfilt4_fft(:,2)./m_ax4fft,'k'); hold on
plot(FaxisL5,dataLfilt5_fft(:,2)./m_ax5fft,'c'); hold on
title('Accelerometer Frequency Spectrum Comparison')
xlabel('Frequency(Hz)')
ylabel('Intensity')
legend('Data 1','Data 2','Data 3','Data 4','Data 5')

%Normal Frequency Spectrum
figure(43)
plot(FaxisL,a_z_fft./m_Lzfft,'r');hold on
plot(FaxisL,dataLfilt_fft(:,1)./m_azfft,'k')
title('Normalized Frequency Spectrum of Normal Acceleration, Data 1')
xlabel('Frequecy(Hz)')
ylabel('Intensity')


figure(44)
plot(FaxisL2,a_z2_fft./m_Lz2fft,'r');hold on
plot(FaxisL2,dataLfilt2_fft(:,1)./m_az2fft,'k')
title('Normalized Frequency Spectrum of Normal Acceleration, Data 2')
xlabel('Frequecy(Hz)')
ylabel('Intensity')


figure(45)
plot(FaxisL3,a_z3_fft./m_Lz3fft,'r');hold on
plot(FaxisL3,dataLfilt3_fft(:,1)./m_az3fft,'k')
title('Normalized Frequency Spectrum of Normal Acceleration, Data 3')
xlabel('Frequecy(Hz)')
ylabel('Intensity')


figure(46)
plot(FaxisL4,a_z4_fft./m_Lz4fft,'r');hold on
plot(FaxisL4,dataLfilt4_fft(:,1)./m_az4fft,'k')
title('Normalized Frequency Spectrum of Normal Acceleration, Data 4')
xlabel('Frequecy(Hz)')
ylabel('Intensity')


figure(47)
plot(FaxisL5,a_z5_fft./m_Lz5fft,'r');hold on
plot(FaxisL5,dataLfilt5_fft(:,1)./m_az5fft,'k')
title('Normalized Frequency Spectrum of Normal Acceleration, Data 5')
xlabel('Frequecy(Hz)')
```

```matlab
ylabel('Intensity')

figure(48)
plot(FaxisL,a_z_fft./m_Lzfft,'b');hold on
plot(FaxisL2,a_z2_fft./m_Lz2fft,'r');hold on
plot(FaxisL3,a_z3_fft./m_Lz3fft,'k');hold on
plot(FaxisL4,a_z4_fft./m_Lz4fft,'g');hold on
plot(FaxisL5,a_z5_fft./m_Lz5fft,'c');hold on
title('Frequency Spectrum Comparison, Normal Acceleration')
legend('Data 1','Data 2','Data 3','Data 4','Data 5')
xlabel('Frequency (Hz)')
ylabel('Intensity')

figure(49)
plot(FaxisL,dataLfilt_fft(:,1)./m_azfft,'b'); hold on
plot(FaxisL2,dataLfilt2_fft(:,1)./m_az2fft,'r'); hold on
plot(FaxisL3,dataLfilt3_fft(:,1)./m_az3fft,'g'); hold on
plot(FaxisL4,dataLfilt4_fft(:,1)./m_az4fft,'k'); hold on
plot(FaxisL5,dataLfilt5_fft(:,1)./m_az5fft,'c'); hold on
title('Accelerometer Frequency Spectrum Comparison, Normal
Acceleration')
xlabel('Frequency(Hz)')
ylabel('Intensity')
legend('Data 1','Data 2','Data 3','Data 4','Data 5')

%Isolate the "good" portion of the signal
tx1=.0992; %start time of initial excitation
tx2=.13; %t1 + (1/bandwidth) or end of signal agreement with
accelerometer
tz1=.0992;
tz2=.13;
Intx=find(timeL>tx1&timeL<tx2);
Intz=find(timeL>tz1&timeL<tz2);

%LDV Data
a_x_good=zeros(size(a_x));
a_x_good(Intx)=a_x(Intx);
a_z_good=zeros(size(a_z));
a_z_good(Intz)=a_z(Intz);

a_x2_good=zeros(size(a_x2));
a_x2_good(Intx)=a_x2(Intx);
a_z2_good=zeros(size(a_z2));
a_z2_good(Intz)=a_z2(Intz);

a_x3_good=zeros(size(a_x3));
a_x3_good(Intx)=a_x3(Intx);
a_z3_good=zeros(size(a_z3));
a_z3_good(Intz)=a_z3(Intz);

a_x4_good=zeros(size(a_x4));
a_x4_good(Intx)=a_x4(Intx);
a_z4_good=zeros(size(a_z4));
a_z4_good(Intz)=a_z4(Intz);
```

```matlab
a_x5_good=zeros(size(a_x5));
a_x5_good(Intx)=a_x5(Intx);
a_z5_good=zeros(size(a_z5));
a_z5_good(Intz)=a_z5(Intz);

%Accelerometer Data
acc_x_good=zeros(size(dataLfilt(:,2)));
acc_x_good(Intx)=dataLfilt(Intx,2);
acc_z_good=zeros(size(dataLfilt(:,1)));
acc_z_good(Intz)=dataLfilt(Intz,1);

acc_x2_good=zeros(size(dataLfilt2(:,2)));
acc_x2_good(Intx)=dataLfilt2(Intx,2);
acc_z2_good=zeros(size(dataLfilt2(:,1)));
acc_z2_good(Intz)=dataLfilt2(Intz,1);

acc_x3_good=zeros(size(dataLfilt3(:,2)));
acc_x3_good(Intx)=dataLfilt3(Intx,2);
acc_z3_good=zeros(size(dataLfilt3(:,1)));
acc_z3_good(Intz)=dataLfilt3(Intz,1);

acc_x4_good=zeros(size(dataLfilt4(:,2)));
acc_x4_good(Intx)=dataLfilt4(Intx,2);
acc_z4_good=zeros(size(dataLfilt4(:,1)));
acc_z4_good(Intz)=dataLfilt4(Intz,1);

acc_x5_good=zeros(size(dataLfilt5(:,2)));
acc_x5_good(Intx)=dataLfilt5(Intx,2);
acc_z5_good=zeros(size(dataLfilt5(:,1)));
acc_z5_good(Intz)=dataLfilt5(Intz,1);

%Compare Cross-correlations with Accelerometer Data
xcorr_x=xcorr(acc_x_good,a_x_good,'coeff');
xcorr_xmax1=max(xcorr_x)
xcorr_z=xcorr(acc_z_good,a_z_good,'coeff');
xcorr_zmax1=max(xcorr_z)

xcorr_x2=xcorr(acc_x2_good,a_x2_good,'coeff');
xcorr_xmax2=max(xcorr_x2)
xcorr_z2=xcorr(acc_z2_good,a_z2_good,'coeff');
xcorr_zmax2=max(xcorr_z2)

xcorr_x3=xcorr(acc_x3_good,a_x3_good,'coeff');
xcorr_xmax3=max(xcorr_x3)
xcorr_z3=xcorr(acc_z3_good,a_z3_good,'coeff');
xcorr_zmax3=max(xcorr_z3)

xcorr_x4=xcorr(acc_x4_good,a_x4_good,'coeff');
xcorr_xmax4=max(xcorr_x4)
xcorr_z4=xcorr(acc_z4_good,a_z4_good,'coeff');
xcorr_zmax4=max(xcorr_z4)

xcorr_x5=xcorr(acc_x5_good,a_x5_good,'coeff');
xcorr_xmax5=max(xcorr_x5)
xcorr_z5=xcorr(acc_z5_good,a_z5_good,'coeff');
```

```matlab
xcorr_zmax5=max(xcorr_z5)


% a_x_win=zeros(size(a_x));
% Winx=hanning(length(Int));
% a_x_win(Int)=a_x(Int).*Winx;
%
% a_z_win=zeros(size(a_z));
% Winz=hanning(length(Int));
% a_z_win(Int)=a_z(Int).*Winz;
%
% figure(21)
% plot(timeL,a_x_clean)
% title('Hanning Window of In-plane LDV Acceleration')
%
% figure(22)
% plot(timeL,a_z_clean)
% title('Hanning Window of Normal LDV Acceleration')
%
% figure(23)
% plot(a_x_win,a_z_win)
% title('Polarization of LDV Acceleration')
% xlabel('In-plane Acceleration')
% ylabel('Normal Acceleration')


%Find Theta (assuming theta1 = theta2 measured from the plate to the
beam)
% initialwave_0 = 4974;
% initialwave_1 = 5020;
% yt = dataLfilt(initialwave_0:initialwave_1,3);
% xt =
((dataLfilt(initialwave_0:initialwave_1,4))+dataLfilt(initialwave_0:ini
tialwave_1,5))./2;
% figure
% plot(xt,yt)
% slope = polyfit(xt,yt,1)
% theta = asind(slope(1))
%
% %More robust way to find theta; y = ax, a = 1/sin(theta)
% Uzt_12iw = ((dataLfilt(initialwave_0:initialwave_1,4)) +
dataLfilt(initialwave_0:initialwave_1,5))./2; %(u1 + u2)/2; ;
% Uzt_iw = dataLfilt(initialwave_0:initialwave_1,3); %Normal LDV data
for the initial wave
% y = xcorr(Uzt_iw,Uzt_12iw);
% x = xcorr(Uzt_12iw,Uzt_12iw);
% a = max(y)./max(x);
% theta = asind(1/a)


% %Compare LDV acceleration data to accelerometer data through
% %cross-correlation in the time domain


% xcorrAzt =
xcorr(Azt(initialwave_0:initialwave_1),C(initialwavea_0:initialwavea_1,
5)); %%%initialwavea_0:initialwavea_1... cuts accelerometer data to
initial wave only
% figure(5)
% plot(xcorrAzt)
```

104

```
% title('Cross-correlation of the LDV out-of-plane acceleration data
and the out-of-plane accelerometer data')
% xcorrAxt =
xcorr(Axt(initialwave_0:initialwave_1),C(initialwavea_0:initialwavea_1,
4));
% figure(6)
% plot(xcorrAxt)
% title('Cross-correlation of the LDV in-plane accerelation data and
the
% in-plane accelerometer data')
```

CODE USED TO ANALYZE STRESS ON PLATE

```
clear all
% theta= 71.57;
% counter=0;
% for i=1:12;
% counter=counter+1;
% FPATH='F:\Vib Msmt Research\Work in Progress Data\Plate Stress
Test\';
% filename=[num2str(i),'.dat'];
% fid=fopen([FPATH,filename],'r');
% temp=fread(fid,inf,'double');
% freqL=temp(1); %Hz
% num_chL=temp(2); %Number of Channels Recorded
% samples_ch = (length(temp)-2)/num_chL; %Number of samples per channel
% for idx=1:num_chL
%         data(:,idx)=temp((3+(samples_ch*(idx-
1))):((idx*samples_ch)+2));
% end
% timeL=1/freqL:1/freqL:(length(data(:,1)))/freqL;
% %save data.mat 'data1' 'time' 'freq';
% fclose all; clear fid temp idx idx2 ans %filename ans;
% u_zm(:,counter)=data(:,4);
% u_zc(:,counter)=(data(:,5)+data(:,6))/(2.*sind(theta));
% u_x(:,counter)=(data(:,5)-data(:,6))/(2.*cosd(theta));
% clear data
% end
% save EXPPLATE u_zc u_zm u_x timeL freqL

load EXPPLATE

NL=length(timeL);
TsL=1/freqL;
FaxisL=[0:NL-1]/NL/TsL;

u_z=u_zm;
%Plot Frequency Spectrums
jj=6
figure(jj);clf;hold on
plot(FaxisL,abs(fft(u_x(:,jj))));hold on
plot(FaxisL,abs(fft(u_z(:,jj))),'k');hold on
% plot(FaxisL,abs(u_zfilt_fft(:,7:12)),'r');hold on
% plot(FaxisL,abs(u_zfilt_fft(:,13:18)),'g');hold on
```

```matlab
% plot(FaxisL,abs(u_zfilt_fft(:,19:24)),'k');hold on
title('UNDFILTERED  Frequency Spectrum of Normal Velocity')
xlabel('Frequecy(Hz)')
ylabel('Intensity')




%Filter LDV data
f1=6e3;
f2=22e3;
[B,A] = butter(4,[f1 f2]/(freqL/2));%band -pass
% [B,A] = butter(7,[50]/(freqL/2),'low');

%Filter data
u_xfilt=filtfilt(B,A,u_x);
u_zfilt=filtfilt(B,A,u_z);

%Compute fft
u_xfilt_fft=(fft(u_xfilt));
u_zfilt_fft=(fft(u_zfilt));

%Plot time signals
jj=1;
figure();clf;hold on
plot(timeL,u_zfilt(:,jj))
plot(timeL,u_xfilt(:,jj))
title('Normal Velocity black')
xlabel('Time(s)')
ylabel('Voltage(V)')

figure()
plot(timeL,u_xfilt(:,1))
title('In-plane Velocity')
xlabel('Time(s)')
ylabel('Voltage(V)')

figure()
plot(timeL,u_zfilt(:,1));hold on
plot(timeL,u_xfilt(:,1)+3.5,'r')
title('top In-plane, bottom Normal')

%Plot Frequency Spectrums
% mz=max(abs(u_zfilt_fft));
figure()
plot(FaxisL,abs(u_zfilt_fft(:,1:6)),'b');hold on
plot(FaxisL,abs(u_zfilt_fft(:,7:12)),'k');hold on
% plot(FaxisL,abs(u_zfilt_fft(:,2))./mz(:,2),'r');hold on
% plot(FaxisL,abs(u_zfilt_fft(:,3))./mz(:,3),'g');hold on
% plot(FaxisL,abs(u_zfilt_fft(:,4))./mz(:,4),'k');hold on
% plot(FaxisL,abs(u_zfilt_fft(:,5))./mz(:,5),'c');hold on
% plot(FaxisL,abs(u_zfilt_fft(:,6))./mz(:,6),'.');hold on
title('Frequency Spectrum of Normal Velocity, loads 7-12 in black')
xlabel('Frequecy(Hz)')
ylabel('Intensity')

figure()
```

```matlab
plot(FaxisL,abs(u_xfilt_fft(:,1:6)),'b');hold on
plot(FaxisL,abs(u_xfilt_fft(:,7:12)),'k');hold on
% plot(FaxisL,abs(u_xfilt_fft(:,7:12)),'r');hold on
% plot(FaxisL,abs(u_xfilt_fft(:,13:18)),'g');hold on
% plot(FaxisL,abs(u_xfilt_fft(:,19:24)),'k');hold on
title('Frequency Spectrum of In-plane Velocity, loads 7-12 in black')
xlabel('Frequecy(Hz)')
ylabel('Intensity')

%Find Frequency Value at Peaks of Normal Velocity
fiz=16060;
ffz=16110;
fbandz=find(FaxisL>fiz&FaxisL<ffz);
for kk=1:12;
    [Yz(:,kk),fz(:,kk)]=max(abs(u_zfilt_fft(fbandz,kk)));
    f_pz(:,kk)=fz(:,kk)+min(fbandz)-2;
end

figure()
plot(FaxisL,abs(u_zfilt_fft(:,1:12)));hold on
plot(f_pz(:,1:12),Yz(:,1:12),'.');

f0z=f_pz(1);
f_pzrel(:,1:12)=(f_pz(:,:)-f0z)./f0z;
lb=[100 103 106 109 112 115 200 205 210 215 225 235];
lb0=lb(1);
lb_rel=(lb-lb0)./lb0;

figure()
plot(lb_rel(1:6),f_pzrel(1:6));hold on
plot(lb_rel(1:6),f_pzrel(1:6),'.')
title('Relative Frequency Shift vs. Relative Change in Applied Load,
Normal Component')
ylabel('Relative Frequency Shift (Hz)')
xlabel('Relative Change in Applied Load (lb)')

% figure()
% plot(lb,f_pzrel);hold on
% plot(lb,f_pzrel,'.')
% title('Relative Frequency vs. Load, Normal Component')
% ylabel('Relative Frequency (Hz)')
% xlabel('Applied Load (lb)')

%Find Frequency Value at Peaks of In-plane Velocity
fix=12900;
ffx=13200;
fbandx=find(FaxisL>fix&FaxisL<ffx);
for kk=1:12;
    [Yx(:,kk),fx(:,kk)]=max(abs(u_xfilt_fft(fbandx,kk)));
    f_px(:,kk)=fx(:,kk)+min(fbandx)-2;
end

figure()
plot(FaxisL,abs(u_xfilt_fft(:,1:12)));hold on
plot(f_px(:,1:12),Yx(:,1:12),'.');
```

107

```matlab
f0x=f_px(1);
f_pxrel(:,1:12)=(f_px(:,:)-f0x)./f0x;

figure()
plot(lb_rel(1:6),f_pxrel(1:6));hold on
plot(lb_rel(1:6),f_pxrel(1:6),'.')
title('Relative Frequency Shift vs. Relative Change in Applied Load,
In-plane Component')
ylabel('Relative Frequency Shift (Hz)')
xlabel('Relative Change in Applied Load (lb)')


%%%%%%%%%%%%%%%%%%%%%%%%%%%%%%%%%%%%%%%%%%%%%%%%%%%%%%%%%%%%%%%%%%%%%%%
%%%%%%%%%%%%%%%%%%%%%%%%%%%%%%%%%%%%%%%%%%%%%
%Window Signal and Polarization vs. Frequency Analysis
% %Isolate the "good" portion of the signal
t1=.1012; %start time of initial excitation
t2=.1045; %t1 + (1/bandwidth) or end of signal agreement with
accelerometer
% % t1=.1019; %start time of arbitrary "middle" window
% % t2=t1+.0004; %end of "middle" window of same width as intial window
% % t1=.1050; %start time of arbitrary "late" window
% % t2=t1+.0004; %end of "late" window of same length as initial window

Int=find(timeL>t1&timeL<t2);

u_x_win(:,:)=zeros(size(u_xfilt(:,:)));
u_z_win(:,:)=zeros(size(u_zfilt(:,:)));
for iii=1:12;
u_x_win(Int,iii)=u_xfilt(Int,iii).*hanning(length(Int));
u_z_win(Int,iii)=u_zfilt(Int,iii).*hanning(length(Int));
% u_x_win(Int,iii)=u_xfilt(Int,iii);
% u_z_win(Int,iii)=u_zfilt(Int,iii);
u_x_winfft(:,iii)=fft(u_x_win(:,iii));
u_z_winfft(:,iii)=fft(u_z_win(:,iii));
angle_a(:,iii)=angle(u_x_winfft(:,iii)./u_z_winfft(:,iii));
end

figure()
plot(timeL,u_x_win(:,1)+3.5,'r');hold on
plot(timeL,u_z_win(:,1))
title('top In-plane, bottom Normal')

%Plot Polarization v Frequency
figure()
% plot(FaxisL,unwrap(angle_a(:,1:6)));hold on
plot(FaxisL,10*angle_a(:,1:6));hold on
plot(FaxisL,abs(u_zfilt_fft(:,1:6)),'k');hold on
plot(FaxisL,abs(u_xfilt_fft(:,1:6)),'b');hold on
xlim([6e3 21.9e3])
title('Polarization v Frequency')
xlabel('Frequency (Hz)')
ylabel('Polarization Angle')
%
```

```matlab
%%%%%%%%%%%%%%%%%%%%%%%%%%%%%%%%%%%%%%%%%%%%%%%%%%%%%%%%%%%%%%%%%%%%%%%%%%%%%%%%
%%%%%%%%%%%%%%%%%%%%%%%%%%%%%%%%%%%%%%%%%%%
%Time Domain Polarization Analysis using Ellipses
%Filter LDV data
nband=.1e2; %Define width of narrowband frequency to filter window of
interest
freq0=9.9e3;
freq1=10e3;
u_x_winfilt(:,:,:)=zeros(length(Int),size(u_z,2),((freq1-
freq0)/nband));
u_z_winfilt(:,:,:)=zeros(length(Int),size(u_z,2),((freq1-
freq0)/nband));
for f=1:((freq1-freq0)/nband);
[C,D] = butter(4,[(freq0-nband)+f*nband freq0+f*nband]/(freqL/2));%band
-pass
% [C,D] = butter(4,[12e3 13e3]/(freqL/2));%band -pass
u_xtemp(:,:,f)=filtfilt(C,D,u_x_win(:,:));
u_x_winfilt(:,:,f)=u_xtemp(Int,:,f);
clear u_xtemp

u_ztemp(:,:,f)=filtfilt(C,D,u_z_win(:,:));
u_z_winfilt(:,:,f)=u_ztemp(Int,:,f);
clear u_ztemp
% u_x_winfilt_fft(:,:,f)=fft(u_x_winfilt(:,:,f));%fft(LDV(:,1:2));
% u_z_winfilt(:,:,f)=filtfilt(C,D,u_z_win(:,:));
% u_z_winfilt_fft(:,:,f)=fft(u_z_winfilt(:,:,f));
end

% %Interpolate data to improve resolution
idx=1:length(Int);
idx_spline=[idx(1):.005:idx(end)];
for ff=1:((freq1-freq0)/nband);
for v=1:12;
u_x_spline(:,v,ff)=spline(idx,u_x_winfilt(:,v,ff),idx_spline);
u_z_spline(:,v,ff)=spline(idx,u_z_winfilt(:,v,ff),idx_spline);
end
end

gg=8;
figure(ff);clf;hold on
for vv=19:24
plot(u_x_spline(:,vv,8),u_z_spline(:,vv,gg),'r')
pause
plot(u_x_spline(:,vv,gg),u_z_spline(:,vv,gg),'k')
end
figure(100+gg);clf;hold on
vv=[22:24]
plot(squeeze(u_x_spline(:,vv,ff)),squeeze(u_z_spline(:,vv,ff)))


for fff=1:((freq1-freq0)/nband);
figure();hold on
plot(u_x_spline(:,1,fff),u_z_spline(:,1,fff));hold on
plot(u_x_spline(:,2,fff),u_z_spline(:,2,fff),'r');hold on
plot(u_x_spline(:,3,fff),u_z_spline(:,3,fff),'k');hold on
plot(u_x_spline(:,4,fff),u_z_spline(:,4,fff),'g');hold on
```

```matlab
plot(u_x_spline(:,5,fff),u_z_spline(:,5,fff),'c');hold on
plot(u_x_spline(:,6,fff),u_z_spline(:,6,fff),'y');hold on
title('Polarization Ellipse, Window 2 (t=.1020s-.1053s), Load Range 1')
xlabel('In-plane Velocity(volts)')
ylabel('Out-of-plane Velocity(volts)')
axis equal
% axis tight
end

figure()
plot(abs(u_x_winfilt_fft))

figure()
plot(abs(u_z_winfilt_fft))
%%%%%%%%%%%%%%%%%%%%%%%%%%%%%%%%%%%%%%%%%%%%%%%%%%%%%%%%%%%%%%%%%%%%%%%%%%%%
%%%%%%%%%%%%%%%%%%%%%%%%%%%%%%%%%%%%%%%%%%%%%%

%%estimate noise level
NLx=mean(median(std(u_xfilt(1:4e3,:),0,1)));
NLz=mean(median(std(u_zfilt(1:4e3,:),0,1)));


tcorr=[(-(NL-1):NL-1)].*TsL;


%%%%%%%%%%%%%%%%%%%%%%%%%%%%%%%%%%%%%%%%%%%%%%%%%%%%%%%%%%%%%%%
%%%%%%%%%%%%%%%%%%%%%%%%%%%%%%%%%%%%%%%%%%%%%%%%%%%%%%%%%%%%%%%%%%
%%%%%Detect THRESHOLD
DECAY=200; %%number of points for the decay
WINDOW=hanning(DECAY*2);
INDEX=1;


for jj=1:size(u_zfilt,2)

    for Rec=[1, 2];
        if Rec==1
            D1=u_xfilt(:,jj);
        THR=5*NOISElevel
         elseif Rec==2
            D1=u_zfilt(:,jj);
        end

        IIok=find(abs(D1)>=THR);
        ImaxALL(INDEX,jj)=max(find(diff(IIok)<=1));%%Prevent fomr
getting influenced by isolated spikes
        IIok=[IIok(1):IIok(ImaxALL(INDEX,jj))];

        Imax(jj,Rec)=IIok(end);
        Imin(jj,Rec)=IIok(1);
    end
end

IIok=[max(max(Imin)):min(min(Imax))];

%%%%Cut all files with the same threshold
```

110

```matlab
    for jj=1:size(DATA,2)

     for Rec=[1, 2];
         if Rec==1
             D1=DATA1(:,jj);
         elseif Rec==2
             D1=DATA(:,jj);
         end
      %%Selectionne la partie du signal au dessus du Seuil
         %%"THR"
         TEMP=zeros(N,1);
         TEMP(IIok)=D1(IIok);


         %%Arrondis les bords.
         TEMP(Imax-DECAY+1:Imax)=TEMP(Imax-
DECAY+1:Imax).*WINDOW(DECAY+1:end);
         TEMP(Imin:Imin+DECAY-1)=TEMP(Imin:Imin+DECAY-
1).*WINDOW(1:DECAY);


         IIhigh=find(abs(TEMP)>=THR);

         %%Clip l'amplitude;
         TEMP(IIhigh)=THR.*sign(TEMP(IIhigh));
         D1=TEMP;

         %Remplace chaque ligne par les valeurs clipe
         if Rec==1
             DATA1(:,jj)=D1;
         elseif Rec==2
             DATA(:,jj)=D1;
         end

     end

end;



%%%Look at correlations
for ii=1:6
Cxz(:,ii)=xcorr(u_xfilt(:,ii),u_zfilt(:,ii));
end
figure(1);
plot(tcorr,Cxz)

%Analysis of Polarization Angle in Time Domain Using Hilbert Function
[Q R]=size(u_xfilt);
for ii=1:R;
Au_x(:,ii)=u_xfilt(:,ii)+hilbert(u_xfilt(:,ii));
Au_z(:,ii)=u_zfilt(:,ii)+hilbert(u_zfilt(:,ii));
Phx(:,ii)=angle(Au_x(:,ii));
Phz(:,ii)=angle(Au_z(:,ii));
```

111

```matlab
end

% Phx0=Phx(:,1);
% Phz0=Phz(:,1);
% for id=1:24;
% Phx_rel(:,id)=(Phx(:,id)-Phx0)./Phx0;
% Phz_rel(:,id)=(Phz(:,id)-Phz0)./Phz0;
% end
%
% %Relative Phase
% figure()
% plot(timeL(5.1e3:end),unwrap(Phx_rel(5.1e3:end,12:18)));hold on
% plot(timeL(5.1e3:end),unwrap(Phz_rel(5.1e3:end,12:18)))
%
% PhD_rel=abs(unwrap(Phz_rel)-unwrap(Phx_rel));
%
% figure()
% plot(timeL,PhD_rel(:,13:18))

figure()
I1=19, I2=24;
plot(timeL(5.1e3:end),(Phx(5.1e3:end,I1:I2)));hold on
%plot(timeL(5.1e3:end),(Phz(5.1e3:end,I1:I2)),'--');hold on
xlim([0.101 0.15])%
plot(timeL(5.1e3:end),unwrap(Phx(5.1e3:end,7:12)),'b');hold on
title('Polarization Angle vs. Time, 100-115lb and 300-315lb')
xlabel('Time(s)')
ylabel('Polarization Angle(radians)')

%Absolute Phase
figure()
I1=19, I2=24;
plot(timeL(5.1e3:end),unwrap(Phx(5.1e3:end,I1:I2)));hold on
plot(timeL(5.1e3:end),unwrap(Phz(5.1e3:end,I1:I2)),'--');hold on
xlim([0.101 0.15])%
plot(timeL(5.1e3:end),unwrap(Phx(5.1e3:end,7:12)),'b');hold on
title('Polarization Angle vs. Time, 100-115lb and 300-315lb')
xlabel('Time(s)')
ylabel('Polarization Angle(radians)')

PhD=unwrap(Phz)-unwrap(Phx);
figure()
plot(timeL(5.1e3:end),PhD(5.1e3:end,1:6),'r');hold on
plot(timeL(5.1e3:end),PhD(5.1e3:end,7:12),'b');hold on
plot(timeL(5.1e3:end),PhD(5.1e3:end,13:18),'g');hold on
plot(timeL(5.1e3:end),PhD(5.1e3:end,19:24),'k');hold on
title('Difference between in-plane and normal polarization vs time,
300-315lb')
```
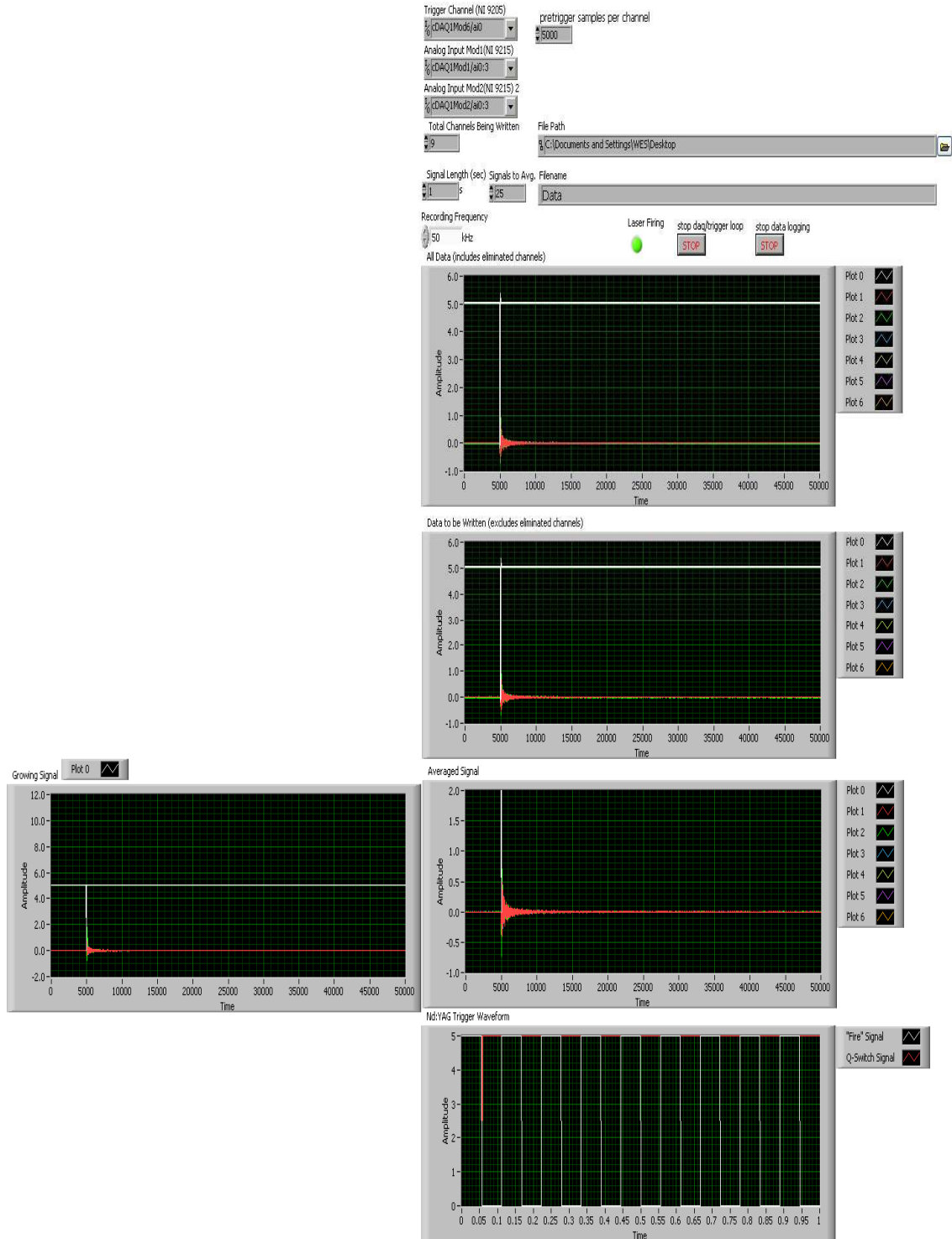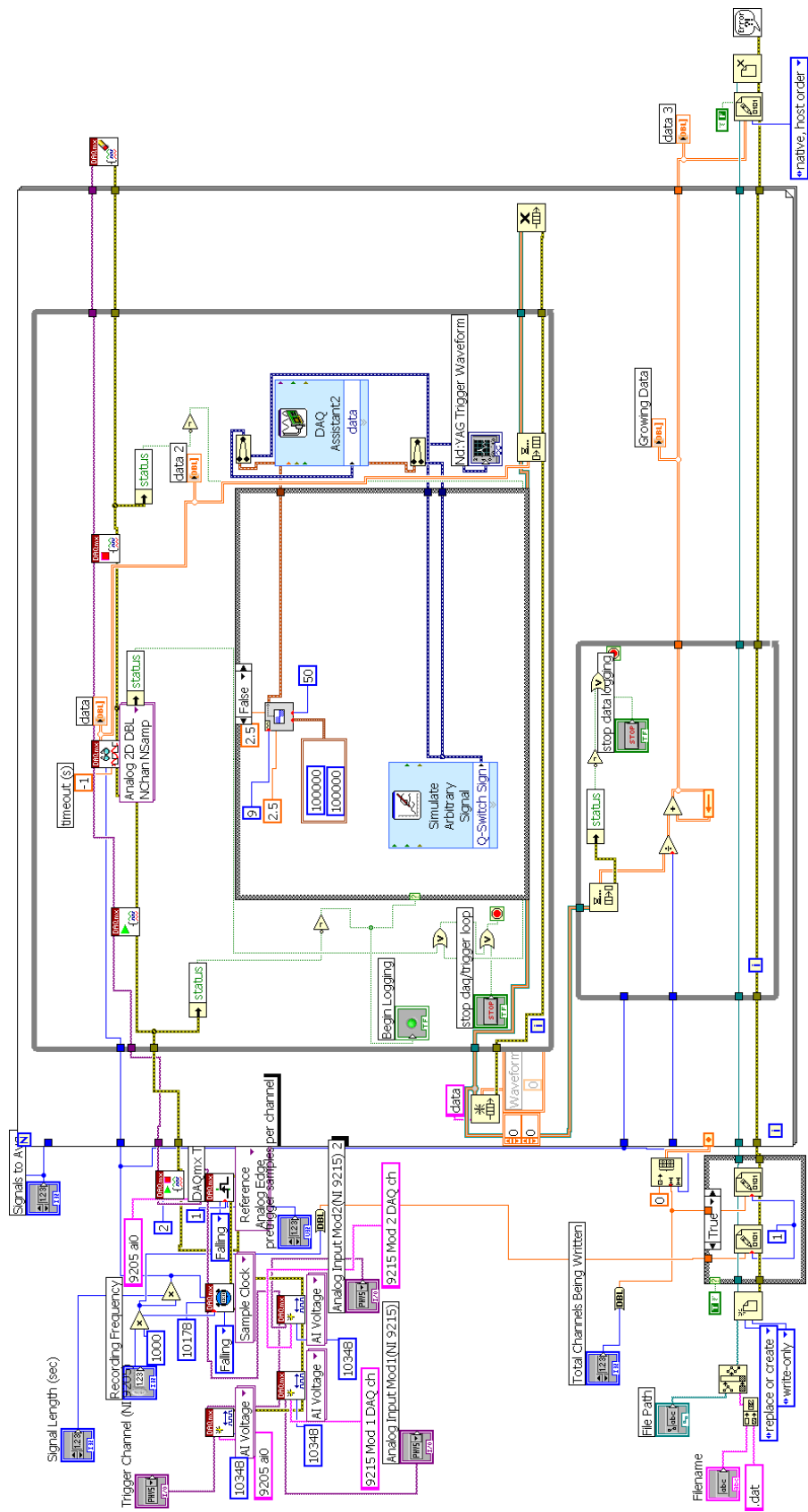
APPENDIX D

LABVIEW VI FRONT PANEL AND BLOCK DIAGRAM

APPENDIX E

NEWPORT OPTICAL TABLE

I-2000 Stabilizers are based on the same platform as the PL-2000 isolators, but they use a pneumatic configuration of three self-leveling valves and a constant air supply to damp outside vibrations caused by the building and its systems. In addition to improving its damping efficiency, this system automatically levels the table any time a load is changed or repositioned. This was crucial as the Nd:YAG laser and the LDVs were constantly repositioned on the table throughout the work on this system. Several basic tests were done showing the improvement in the damping, but this work could not have been done if the table had to be leveled each time a component of significant weight was repositioned.

The following specifications were taken from the "Newport Vibration Control System Instruction Manual":

Specifications

Table Tops:

|	
Flatness:	±0.005in. (0.13mm)*
Compliance:	Consult your Newport Catalog or Newport directly for the specific compliance and other pertinent table top specifications of your particular table top model.

Isolators: Stabilizer™ I-2000

Vertical Resonant Frequency:	<1.1 Hz at 80 psi
Horizontal Resonant Frequency:	<1.5 Hz
Recommended Load Range: (per 4 isolators)	660 to 8,000 lb (300 to 3,600 kg)
Automatic Leveling Accuracy:	±0.010 inch (0.25 mm) standard, higher accuracy available on special order
Vertical Adjustment Range:	1.3 inches (33 mm)
Settling Time: (after 5-lb. weight removal)	<1.5 sec.
Typical Air Pressure Range:	10 to 85 psi (0.7 to 6.0 kg/cm^2)

Isolation System Transmissibility
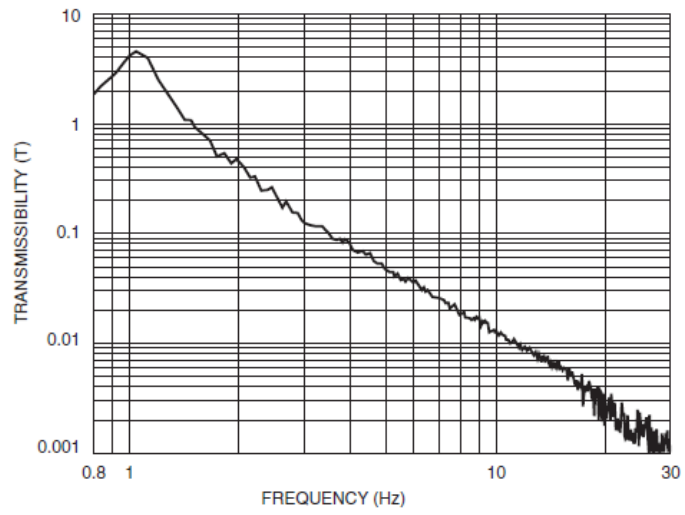
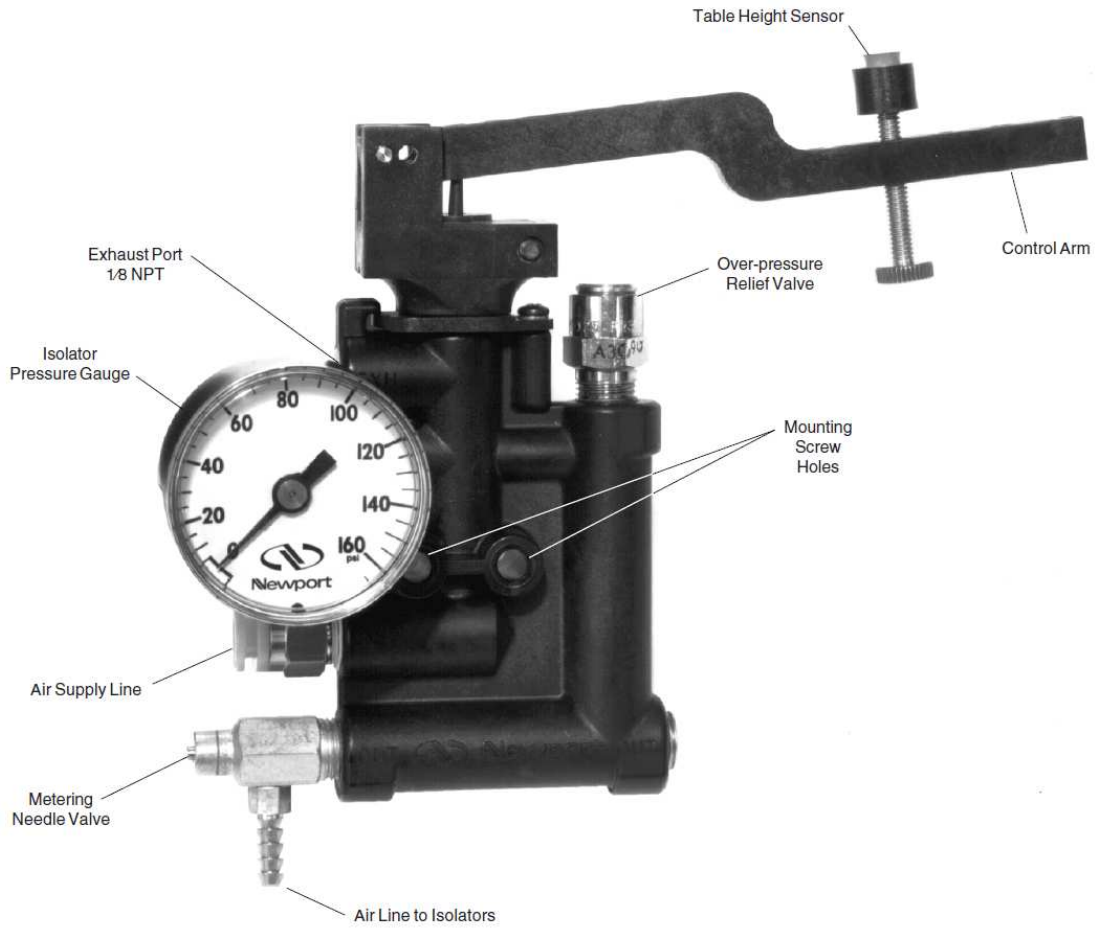

Vertical Transmissibility (at maximum recommended load)
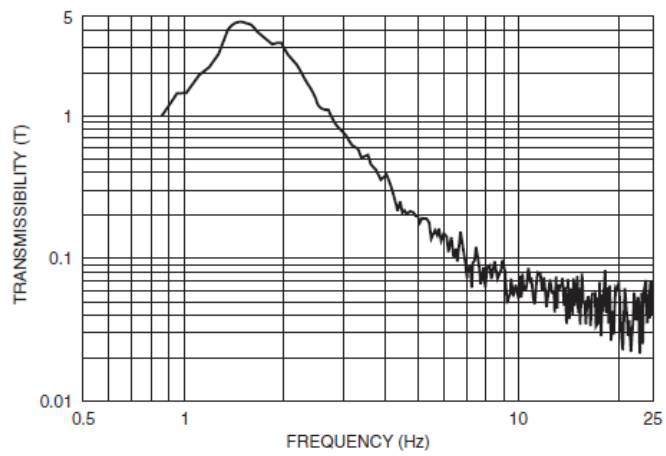
Horizontal Transmissibility

117

Valve: Model IPV

Leveling Accuracy: ±0.010 in (.25 mm) standard**

Materials: Glass fiber reinforced polycarbonate
                                brass

                                Available in non-magnetic version

                                Exhaust may be captured by clean room
                                vacuum system

** Higher accuracies are available by special order.

Model IPV Leveling Valve

REFERENCES

- Achenbach, J.D., (1999), *Wave Propagation in Elastic Solids*, North Holland, Amsterdam.

- Castellini, P, Martarelli, M., Tomasini, E.P., (2006), "Laser Doppler Vibrometry: Development of advanced solutions answering to technology's needs." Mechanical Systems and Signal Processing 20, 1265-1285.

- Continuum, (1996), "Operation and Maintenance Manual for Surelight Lasers", Continuum, USA.

- Ewins, D. and Martarelli, M., (2006), "Continuous scanning laser Doppler vibrometry and speckle noise occurrence." Mechanical Systems and Signal Processing 20, 2277-2288.

- Giurgiutiu, V., (2007), *Structural Health Monitoring: with Piezoelectric Wafer Active Sensors*, Academic Press, NY.

- Graff, K., (1991), *Wave Motion in Elastic Solids*, Dover, NY.

- Junge, M., Jacobs, L., Qu, J., Jarzynski, J., and La Saponara, V., (2004), "The Measurement of Applied Stresses Using the Polarization of Rayleigh Surface Waves", Review of Quantitative Nondestructive Evaluation Vol. 23.

- Junge, M., Qu, J., and Jacobs, L., (2006), "Relationship between Rayleigh wave polarization and state of stress", Ultrasonics 44, 233-237.

- Langston, P.W., (2005) "TV Holography: Speckle Pattern Averaging." Stetson University, DeLand, FL.

- Larose, E., Hall, S., (2009), "Monitoring stress related velocity variation in concrete with a 2.10^{-5} relative resolution using diffuse ultrasound.", The Journal of the Acoustic Society of America (2009) accepted.

- Martarelli, M., (2001) "Exploiting the Laser Scanning Facility for Vibration Measurements." Imperial College of Science, Technology, and Medicine University of London, England.

- Polytec, (2005), "3D Laser Vibrometer, 3D-LV", Polytec International, Waldbronn, Germany.

- Rose, J., (1999), *Ultrasonic Waves in Solid Media*, Cambridge University Press, NY.

- Siegman, Anthony E., (1986), *Lasers*. University Science Books, Herndon, VA.

- Stobbe, D. (2005), "Acoustoelasticity in 7075-T651 Aluminum and Dependence of Third Order Elastic Constants on Fatigue Damage", Georgia Institute of Technology, Atlanta.